THESIS

For the award of the Degree of

DOCTOR OF PHILOSOPHY

UNIVERSITY OF POITIERS
and
UNIVERSITY OF IOANNINA

Submitted by:

LOUKAS E. KOUTSOKERAS

****

GROWTH, STRUCTURE AND ELECTRONIC PROPERTIES OF TERNARY TRANSITION METAL NITRIDES THIN FILMS

****

Ioannina
July 2010

Preface

The unique combination of electrical conductivity, chemical and metallurgical stability, refractory character and lattice constants close to those of III-nitrides, make the transition metal nitrides (TMNs) of groups IVb-VIb promising candidates for electronics and device applications. In this thesis, we extensively studied the structure, stability and microstructure of binary and ternary transition metal nitrides in thin films. This study includes many binary systems and the widest range of ternary nitrides reported ever. Additionally, we examined also the electronic structure, the optical properties and the mechanical behavior of these materials in order to accomplish a complete study about these materials.

This joined PhD thesis, is the result of a close collaboration between two institutes, the University of Poitiers and the University of Ioannina in the field of growth, structure and functional properties of complex transition metal nitrides. The growth of samples and the analysis has been performed at both institutes, and the combination of knowledge and the transfer of know-how, strengthen the results and raises the quality of this work. Three different deposition techniques, pulsed laser deposition (PLD), magnetron sputtering (MS) and ion beam sputtering were used to deposit the samples. X-ray diffraction (XRD), optical reflectance spectroscopy (ORS), *in situ* and *real time* stress measurements, hardness and computational data are some techniques, among others, used to cover this wide study of transition metal nitrides. Special emphasis has been given to the acquisition of accurate experimental data of various structural and functional properties of a wide variety of binary and ternary TMNs, in an effort to establish a database for these materials.

Acknowledgements

I would like to personally thank my advisor Panos Patsalas. Panos was always there to listen and to give advice. He is responsible for my introduction to the research field of thin films and he has confidence in me, when I was doubted myself. He showed me different ways to approach a research problem and the need to be persistent to accomplish any goal. Also, I would like to be grateful for his assistance and guidance in the writing of this thesis.

Also, special thanks go to my co-advisor Gregory Abadias, who is the one that taught me to be organized, precise in my work and really effective, and he widened my scientific and research horizon by introducing me in the field of stress of thin films and their correlation with the microstructural features. In 2009, when I moved to France, at the PHYMAT laboratory for the second year of my studies, his valuable help was everything I needed for settling there and having a good start with my studies. It was a great experience which I will not forget.

Other special thanks go to Dimitris Anagnostopoulos, a friend and mentor, who promoted me from an undergraduate student to a PhD candidate. I really appreciated a lot the discussions with him, his advices in all these years and his continuous support. Also, I would like personally to show my gratitude to George Evangelakis, our host and best friend in the Department of Physics of the University of Ioannina. His critical discussions and questions help me to think through my problems (whether philosophical, scientific or practical) and also opened a way of understanding the real beauty of science in real life. I would like also to extend my heartfelt thanks to Christina Lekka, who supported my work with her valuable contribution and computational data. Additionally, I would like to express gratitude to the other members of the jury committee Prof. P.C. Kelires, Prof. C. Templier, Prof. C. Rebholtz and Prof. I. Panagiotopoulos, for their efforts and time they have devoted in reading and commenting this thesis.

Let me also say "thanks a lot" to Grigoris Matenoglou, a friend who was the first person I met in the laboratory and taught me everything about the lab work. His guidance at the beginning and the close collaboration afterwards, are more than enough to express my gratitude to him. Additionally, I want also to be grateful to Nikos Panagiotopoulos for his assistance in the lab and the fruitful discussions we had.

Furthermore, I would like to gratefully acknowledge all the people who helped me during my work at both institutes; C. Kosmidis, G. Karras and the Central Laser facility of the University of Ioannina for their support in laser depositions, Philippe Guerin for his guidance

List of Papers

In the framework of the present thesis we have published (or prepared) the following peer-reviewed papers:

1   A. Lotsari, G. P. Dimitrakopulos, T. Kehagias, P. Kavouras, H. Zoubos, L. E. Koutsokeras, P. Patsalas, and P. Komninou, *Surface and Coatings Technology* **204**, 1937-1941 (2010).

2   L. E. Koutsokeras, N. Hastas, S. Kassavetis, O. Valassiades, C. Charitidis, S. Logothetidis, and P. Patsalas, *Surface and Coatings Technology* **204**, 2038-2041 (2010).

3   G. Abadias, L. E. Koutsokeras, S. N. Dub, G. N. Tolmachova, A. Debelle, T. Sauvage, and P. Villechaise, *Journal of Vacuum Science and Technology A: Vacuum, Surfaces and Films* **28**, 541-551 (2010).

4   G. M. Matenoglou, C. E. Lekka, L. E. Koutsokeras, G. Karras, C. Kosmidis, G. A. Evangelakis, and P. Patsalas, *Journal of Applied Physics* **105**, 103714, (2009).

5   G. M. Matenoglou, L. E. Koutsokeras, and P. Patsalas, *Applied Physics Letters* **94**, 152108, (2009).

6   G. M. Matenoglou, L. E. Koutsokeras, C. E. Lekka, G. Abadias, C. Kosmidis, G. A. Evangelakis, and P. Patsalas, *Surface and Coatings Technology* **204**, 911-914 (2009).

7   G. Abadias, L. E. Koutsokeras, P. Guerin, and P. Patsalas, *Thin Solid Films* **518**, 1532-1537 (2009).

8   G. M. Matenoglou, L. E. Koutsokeras, C. E. Lekka, G. Abadias, S. Camelio, G. A. Evangelakis, C. Kosmidis, and P. Patsalas, *Journal of Applied Physics* **104**, 124907, (2008).

9   L. E. Koutsokeras, G. Abadias, C. E. Lekka, G. M. Matenoglou, D. F. Anagnostopoulos, G. A. Evangelakis, and P. Patsalas, *Applied Physics Letters* **93**, 011904, (2008).

10 P. Patsalas, G. Abadias, G.M Matenoglou, L.E Koutsokeras, Ch.E Lekka. Transition metal nitride-based complex coatings: kinetic and thermodynamic effects resulting to ternary films or nanocomposites. *Thin Solid Films*, (2010); Submitted

11 L.E Koutsokeras, G. Abadias, P. Patsalas. Texture and microstructure control of ternary nitrides of rocksalt structure. *Journal of Applied Physics*, (2010); In preparation

TABLE OF CONTENTS

CHAPTER 1

INTRODUCTION

1.0 Aim of the PhD thesis

The object of the present PhD thesis is the detailed study of the Transition Metal Nitrides (TMNs) in thin films forms. More specifically, the aim was the study of the ternary TMN, since the binary nitrides have been studied in the last decades, especially TiN. Thus, the study on the binary has been extended to ZrN and TaN using three different deposition techniques to determine the universal mechanisms that affect the stability, growth, microstructure and optical properties. Furthermore, we focused on ternary nitrides in the formation of $M1_xM2_{1-x}N$, where M1 and M2 are transition metals. The alloying of different transition metals in nitrides can lead to improved functionality as a consequence of fine tuning of the microstructure and properties of the final material.

In general, TMNs and especially the nitrides of group IVb-VIb exhibit a unique combination of electron conductivity, refractory character, high hardness, chemical inertness, and a cubic rocksalt structure with a lattice constant close to those of III-nitrides. These properties make them suitable for applications in electronics, such as diffusion barriers, metallizations, and growth templates for wide bandgap semiconductors and as components in microelectromechanical systems (MEMS).

Functional layers in modern devices require very good control of the structure and the microstructure of the used material. Thus we aim in tailoring the microstructure of the coating with composition. By using ternary compounds, the composition of the third element can be used to tailor the properties of the system accordingly to each situation.

1.1 Materials involved

In general, transition metals are the elements of the groups IIIb to IIb (3-12 IUPAC). The common characteristic of these elements is the partially filled d orbitals, thus, the alternative name of the elements is the d-block elements. The group of the TMN is divided into three smaller groups: a) the main elements of the d-block, b) the lanthanides and c) the actinides. The elements used in the framework of the present thesis are only the elements which belong to the groups IVb-VIb, except Vanadium and Chromium (fig 1.1 red). These elements are Titanium (Ti), Zirconium (Zr), Niobium (Nb), Molybdenum (Mo), Hafnium (Hf), Tantalum (Ta) and Tungsten (W).

Figure 1.1: Periodic Table of the elements

All these elements react with nitrogen and form nitrogen compounds, which are called nitrides. TiN and ZrN are the most studied compounds of the TMN. The technological advance in recent decades allowed the use of coatings at the nanometer scale for the improvement of functionality and endurance. These materials in the form of thin films have been already used as protection coatings, due the high hardness or for decorative reasons, because they exhibit a gold-like color (figure 1.2).

Figure 1.2: Titanium nitride coatings on mechanical tools and drills.

Thin film deposition techniques allow the use of coatings almost on every possible surface available.

1.2 General Properties of TMN

In general, TMN have an extraordinary combination of features. These compounds are refractory materials with a very high melting point (T_m) and are very stable in hostile environments because they are chemically inert. In figure 1.3 the melting points of transition metals and TMN of periods 4, 5 and 6 of the periodic table are shown. For the period 4 elements, all the nitrides exhibit much higher melting points than the corresponding metals. The difference in the T_m between metals and nitrides is getting smaller for higher atomic numbers and for the case of chromium, the metal exhibit higher T_m than the nitride. Similar behavior is observed in higher atomic number elements. This behavior can be addressed to the partial occupation of bonding and anti-bonding states.

In pure metals, the increase of valence electrons increases the population of electrons in bonding states, making the bonding of atoms more stable and stronger. This implies a higher T_m because of the greater amount of energy required to break these bonds down. In nitrides compounds the extra free electrons are occupying bonding and anti-bonding states (even though these states are bands in case of a solid) loosening the bond strength.
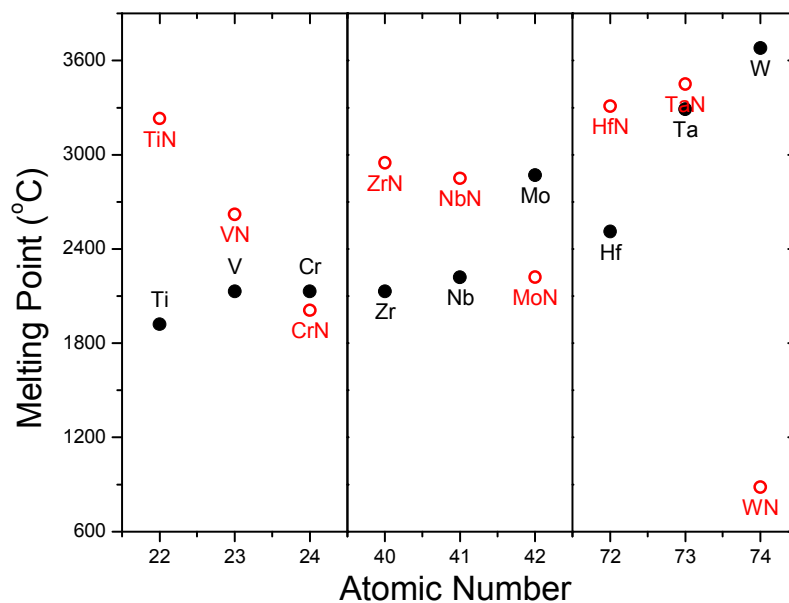
Figure 1.3: Melting point of transition metals and TMNs as a function of the atomic number.

The electrical properties of TMNs can be also explained from the valence electron configuration of the constituent metal. Further on, transition metals with increased valence electrons (such as Nb or Ta) have higher "free" electron density, thus a higher conductivity. Electrical resistivity values of pure metals and nitrides are given in table 1 for comparison [1-4].

Table I: Electrical resistivity values of transition metals

Element	Electrical Resistivity $\mu\Omega$cm 25°C	
	Metal	Nitride
Ti	39	25
Zr	42.1	21
Hf	30	56.5
V	20.1	85
Nb	15.2	58
Ta	12.4-14.7	135-250
Cr	20.8	79
Mo	5.5	19.8
W	5.4	9

The mechanical properties of TMNs are similar to ceramic materials, exhibiting high hardness, high bulk modulus and low plasticity. All the above features are due to the covalent bond between metals and nitrogen. The intrinsic property of the material is the bulk modulus, which relies on the bond strength itself. Covalent bonds with high directionality mean a large bulk modulus, while the hardness is the extrinsic property of the material and depends on the microstructure. The initial value of the bulk modulus can serve as a starting point to produce harder materials by tailoring the microstructure. Hardness values of nitrides as a function of the constituent metal's atomic number (MAN) is shown [1,5,6] in figure 1.4. It is clear that the hardest material among TMNs is TiN which has the lowest MAN number.
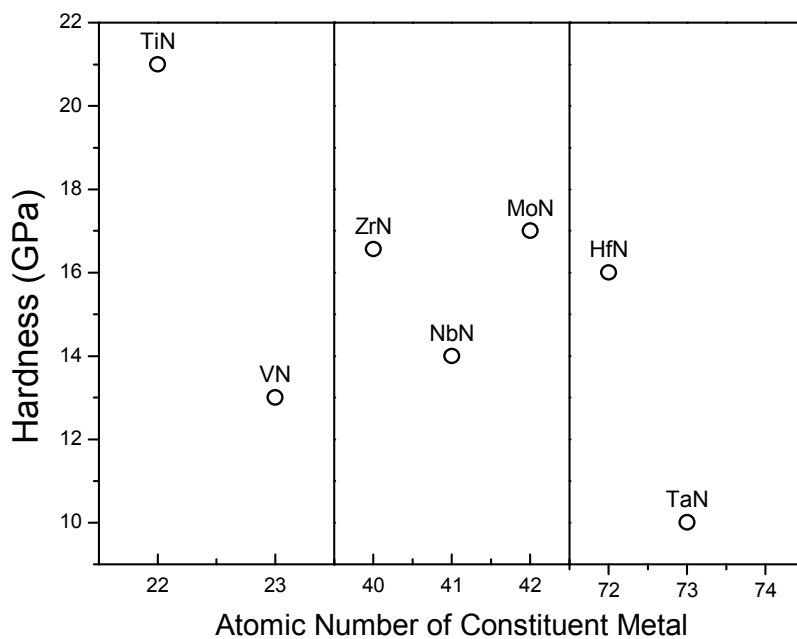
Figure 1.4: Hardness of TMNs as a function of Metal Atomic Number.

The TMNs exhibit also a high young modulus, much higher than the corresponding metal. In figure 1.5 the young modulus of transition metals and the corresponding TMNs are shown. It is obvious that the TMNs are much stiffer than the metals. This is explained from the disturbance of the uniform distribution of the electrons of the metallic bond. A crystalline solid (with a metallic bond) consisted of two distinct atoms, shows less symmetry in the charge density, thus produces electrostatic forces. These forces do not increase significantly the bond strength, but imply restrictions to the movement of electrons, thus increasing stiffness.
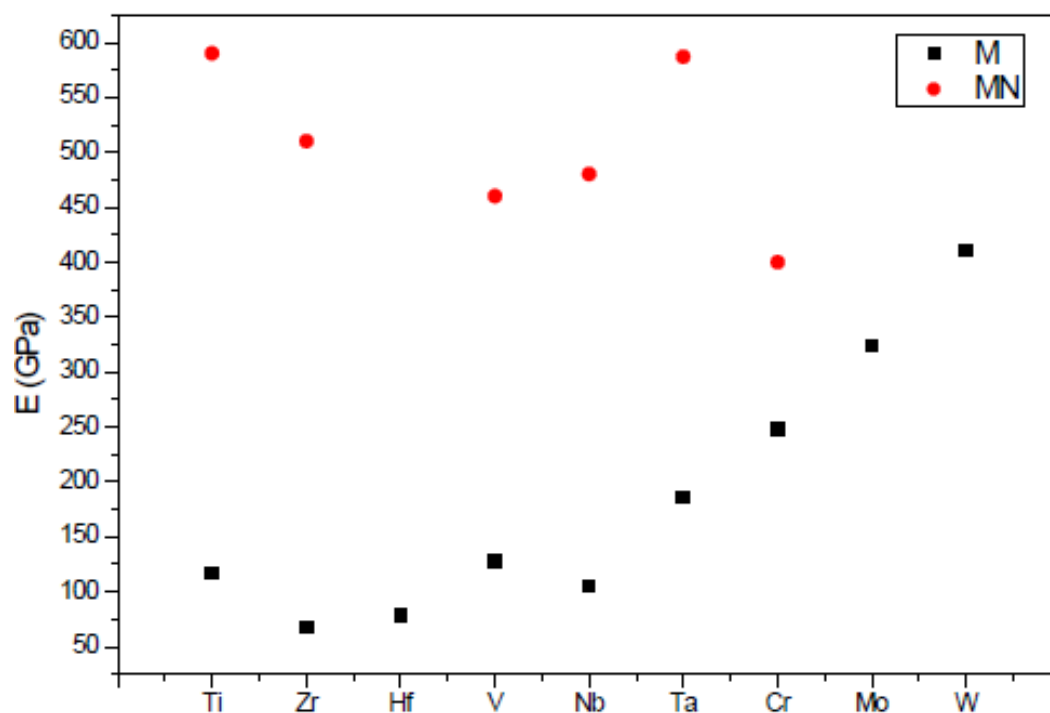
Figure 1.5: Young modulus of transition metals[1,7] (M, square black box) and the corresponding TMNs (MN, round red dots).

1.3 Applications of TMNs

Because of the unique properties they exhibit, the TMNs have been established in technological applications for decades. Particularly TiN, the most studied TMN, has been used as a protective coating for wear resistance on drills and cutting tools. Additionally the golden color of the TiN allows a visual inspection of the condition of the coating, which is really very appreciable in industry. More recently, TiN and ZrN are the most used materials as

coatings for mechanical applications. One of the major problems of TiN is the oxidation at high temperatures (above 600°). ZrN on the other hand, exhibits high hardness.

In general, TMNs exhibit also a very good feature for their use in the microelectronics field, due to the low activation energy for the diffusion of Cu and Si. The diffusion of Cu and Si is a very common problem in microelectronics, which can cause device degradation over time and failure. TMNs are very good candidates as conductive diffusion barriers in integrated microelectronic devices. The activation energy for Cu diffusion in TiN is about 4.4eV, while for the metals is roughly 2eV; TaN is the most used nitride as a diffusion barrier in electronics.

Another great feature of TMNs is the ability to form solid solutions to each other. Solid solutions can be used to match the lattice constants of the epilayers allowing epitaxial growth, which is essential in some areas of the microelectronic industry. Also the formation of solid solutions can be used to tailor all the functional properties of the layer matching it exactly to the desired need.

1.4 General description of the PhD thesis

In the present chapter we give a general description as well as the basic aims of the PhD thesis. The second chapter explains the thin film growth mechanisms and presents the basic theory behind vapor deposition. We describe all the stages from vapor to film formation as well as the nucleation theory which describes film formation. The chapter includes every possible microstructure of a thin film such as the epitaxial films or the polycrystalline ones. Furthermore, we describe the basic features of the deposition techniques and especially the three deposition techniques used for the samples in the framework of the present thesis.

The third chapter is about the characterization techniques and the models used to analyze the experimental data. This chapter is divided in sections for the structural, compositional, morphological and electronic characterization of the thin films and each section consists of the corresponding techniques. For every single technique the basic setup is presented in addition to the basic principle in which the technique relies on. This chapter is accompanied by two appendixes which record all the required mathematical equations for the analysis of the optical and stress measurements; appendix I and II, respectively.

In the forth and fifth chapters are presenting the results of this study. The chapter four is about the structural and microstructural results. Many samples have been measured and evaluated in terms of crystal structure and microstructure, using the techniques described in chapter 3. The fifth chapter is about the electronic structure and the optical properties of the

nitrides. All the transition metal nitrides exhibit electrical and thermal conductivity and the majority of them appear in a gold-like color. From optical measurements as well as ab initio calculations we present the electronic structure of the binary and ternary TMNs. The sixth and final chapter summarizes all the above results and gives the perspectives of the performed work.

References

[1] H. Holleck, Journal of Vacuum Science & Technology A: Vacuum, Surfaces, and Films **4,** 2661-2669 (1986).

[2] T.-E. Kim, S. Han, W.-j. Son, E. Cho, H.-S. Ahn, and S. Shin, Computational Materials Science **44,** 577-580 (2008).

[3] S. T. Oyama, *The Chemistry of Transition Metals Nitrides and Carbides* (Blackie Academic and Professional, New York).

[4] D. Steele, *The Chemistry of the Metallic Elements,* (Pergamon Press, Gr.Britain, 1966).

[5] F. LeM vy, P. Hones, P. E. Schmid, R. SanjineM s, M. Diserens, and C. Wiemer, Surface and Coatings Technology **120-121,** 284-290 (1999).

[6] Z. I. Tolmacheva and V. N. Eremenko, Soviet Powder Metallurgy and Metal Ceramics **2,** 445-449 (1963).

[7] K. I. Portnoi, A. A. Mukaseev, V. N. Gribkov, Y. V. Levinskii, and S. A. Prokof'ev, Powder Metallurgy and Metal Ceramics **7,** 185-186 (1968).

CHAPTER 2

THIN FILM GROWTH

Section I: Film growth mechanisms

2.1 Introduction

In the last decades the materials science has been the central point for the development of almost all the fields of engineering and applied sciences. The field of low dimensional materials, such as the thin films, has played a significant role towards that direction. Materials in thin film form represent the major component of the advanced electronics, protective coatings technology and functional nano-devices. As commonly understood, a thin film is a two dimensional material having thickness from a fraction of nanometer up to few microns[1-3]. A thin film can be attached to a relatively thick substrate or be totally unconfined (free-standing), like the example shown in figure 2.1.
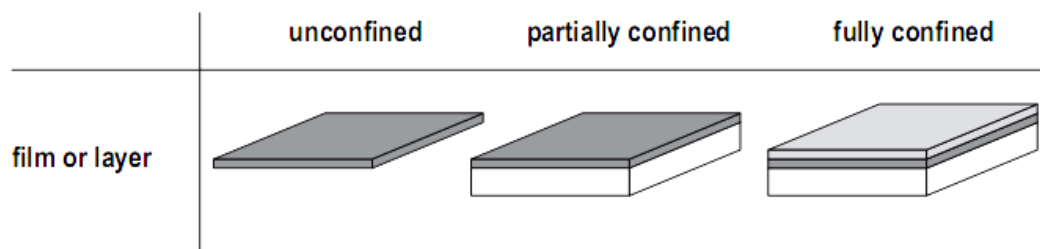
Figure 2.1: A categorization of small volume two dimensional structures in terms of their general shapes and levels of constraints (figure taken from [4]).

The most important and wide-spread methods for transferring material atom by atom from one or more sources to the growth surface are the Physical Vapor Deposition (PVD) and the Chemical Vapor Deposition(CVD) techniques. Both techniques rely on the vapor deposition, which takes place when a surface is exposed to vapors of a material; the vapors are saturated and finally condensed on the surface. The distinction between the above methods is the origin of the vapors. If the vapor is created by physical means the deposition technique is categorized as PVD while, on the other hand, as CVD.

Nowadays there are many variations of the above techniques which have been developed in order to fulfill the requirements of the film's purity, growth rate, structure, morphology and other characteristics. In figure 2.2 the two major categories of vapor deposition CVD and PVD are shown as well as subcategories with representative techniques. Later on we are going to describe in detail three PVD techniques, Pulsed Laser Deposition

(PLD), Magnetron Sputtering technique (MS) and Dual Ion Beam Sputtering (DIBS) technique. These three PVD techniques were used in the framework of the current thesis.
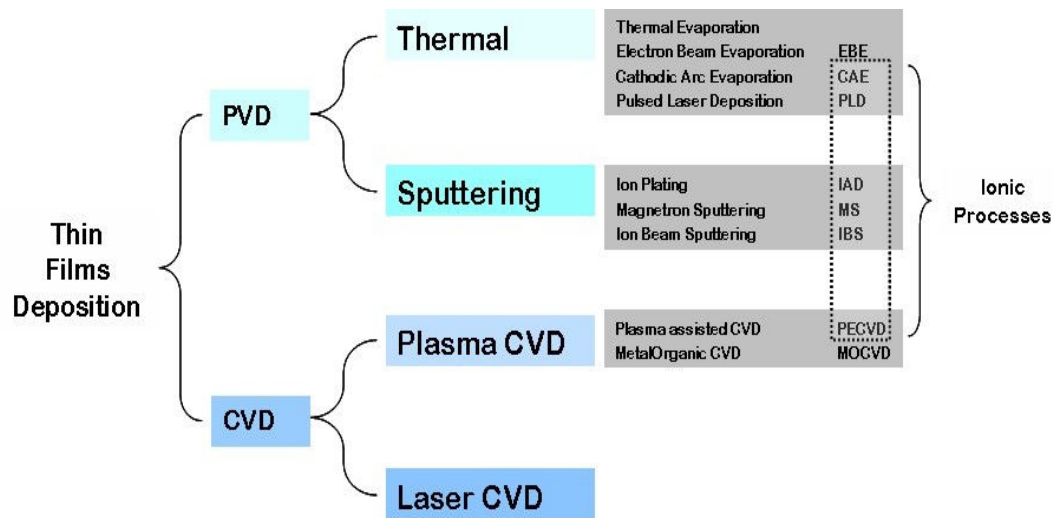
Figure 2.2: A general view and some examples of physical and chemical deposition methods for thin films. The ion based deposition processes are included in the dotted square.

The present chapter is divided in two sections. The first one starts with the qualitative description of the nucleation theory and growth of thin films. In addition, the possible thin film microstructures are presented within the framework of structural zone model. The next section is about the physical vapor deposition techniques used in the framework of the present thesis. Since there are three major components on every technique like the target, the transport medium (gas phase) and the deposition surface, we sort out the phenomena, which are taking place on each component.
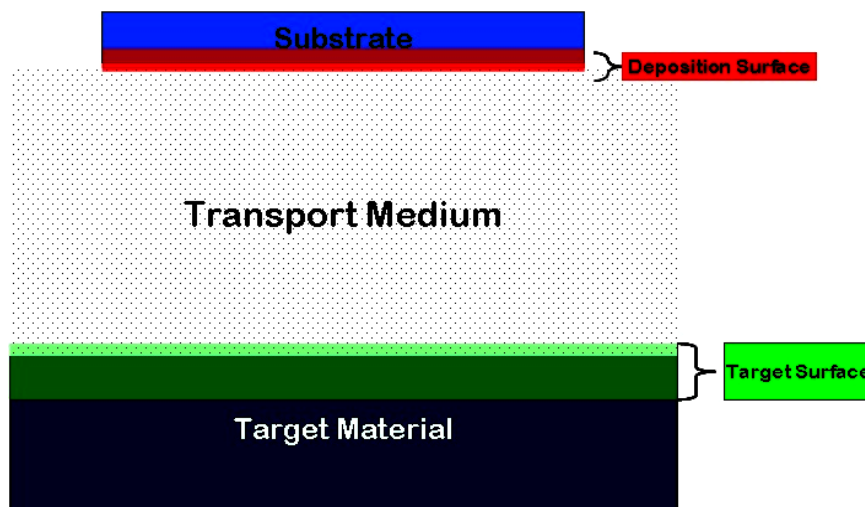
Figure 2.3: The figure shows the three major sites which take part on a deposition technique. The first one (green) is the surface of the target material; the second (dotted) is the transport medium and the third one (red) is the deposition surface.

Thus every deposition technique has a subsection about the processes on the target i.e how the material is ejected from the target (creation of vapor), about the gas phase, i.e how does the species are traveling through the medium, and finally about the deposition surface, i.e how the species arrive on the substrate (figure 2.3).

2.2 Thin film growth modes by vapor deposition

2.2.1 From vapor to adatoms

This stage is describing the transfer of atoms from the vapor phase onto the surface of a substrate. Vapor atoms arrive at the surface of the substrate, adhere to it and finally settle at equilibrium positions. For metastable or amorphous films this settlement may be interrupted preventing atoms to settle in perfect equilibrium positions, i.e lattice sites. The deposited atoms that adhere on the surface are called adatoms. Adatoms act as a two-dimensional vapor and they can diffuse on the surface, or they can return also to gas phase due to thermal fluctuations or resputtering. The temperature of the substrate must be low enough to allow the vapor to be supersaturated onto the surface. The free energy difference between the atoms in the vapor phase and the atoms in the solid phase provides a chemical potential for driving the interface towards the vapor. In order film growth to occur the free energy per adatom must exceed the free energy of an atom totally adjusted on the surface. That means that we should have a free energy reduction to attach an atom on the deposition surface. The nucleation theory is a classical approach to this mechanism and describes thermodynamically the supersaturation of vapors onto the surface.

2.2.2 Nucleation theory

Supersaturation carries a change in free energy per unit volume between the liquid and the newly created solid phase. The change in free energy consists in the gain of forming a new volume and the loss from creating a new interface. For the case of spherical nuclei this change is described by the main equation of nucleation which is:

$$\Delta G \equiv \underbrace{\frac{4}{3}\pi r^3 \Delta G_V}_{\text{Volume Term}} + \underbrace{4\pi r^2 \gamma}_{\text{Surface Term}} . \qquad (2.1)$$

28

Where, G_V is the Gibbs free energy per unit volume and γ is the energy per unit area (interfacial energy) and r is the radius of the sphere. The above equation is neglecting the strain energy of the newly created volume. Phase fluctuations (between vapor and solid) may occur as random events due to the thermal vibration of atoms. An individual fluctuation may or may not be associated with a reduction in free energy, but it can only survive and grow if there is a reduction. When the overall change in free energy ΔG_V is negative, nucleation is favored.

The cost associated with the creation of the new solid phase, the interface energy, is a penalty which becomes smaller as the particle surface to volume ratio decreases leads to a specific size of the nucleus (sphere) where after that point the system is stable and continue growth[5]. This can be derived by differentiating the equation 2.1 with respect to r :

$$\frac{\partial \Delta G}{\partial r} = -4\pi r^2 \Delta G_V + 8\pi r \gamma , \qquad\qquad (2.2)$$

When the change in free energy equals zero, then it is called ΔG_{crit} as well as activation energy barrier for nucleation and the radius at this point is called r_{crit} .
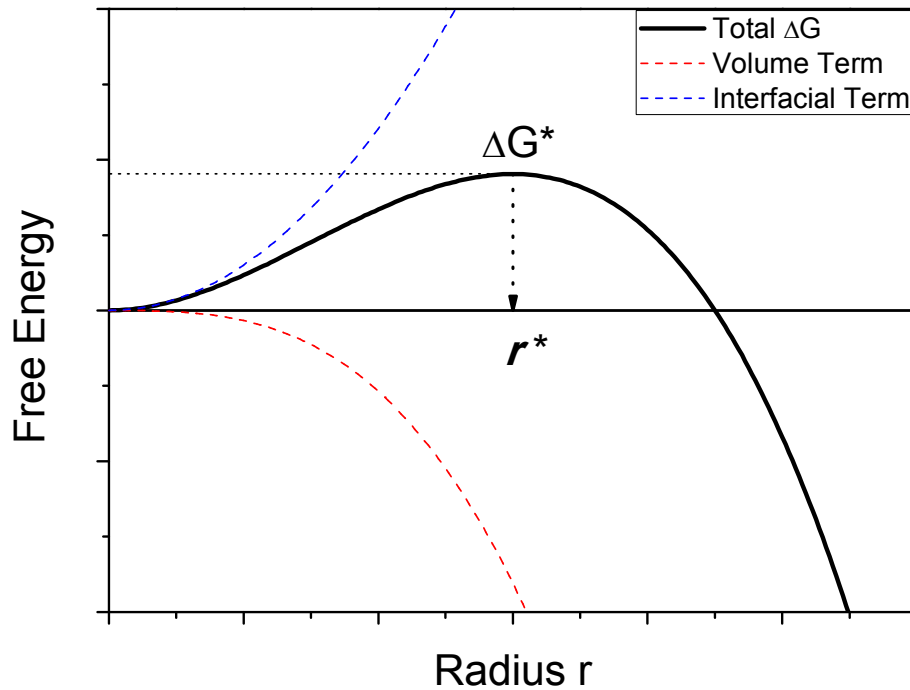
Figure 2.4: This plot shows the change of free energy as a function of r. The blue dashed line is the interface free energy; the red dashed line is the volume energy and the solid black line is the total free energy change as described by the equation 2.1

By setting the $\dfrac{\partial \Delta G}{\partial r}$ equals zero the equation which defines the r_{crit} is :

$$r_{crit} = \frac{2\gamma}{\Delta G_V},\qquad\qquad\qquad\qquad (2.3)$$

and it is the point from where the nucleus is stable and the addition of extra atoms is decreasing more the free energy thus nucleation becoming favorable. The figure 2.4 shows Mathematica calculations based on Eq. 2.1 demonstrating the trend of the free energy as a function of the radius r.

There is another expression (Eq 2.4) of the change in free energy as function of pressure which defines as previous, the activation energy barrier as a function of the pressure ratio between the vapor and the saturated vapor pressure at equilibrium. This is particularly important for the case of vapor growth (PVD, CVD), because the pressure is a key parameter. From this expression can be derived that the supersaturation of the vapor is essential for the condensation (phase change) to occur.

$$\Delta G_V = \frac{kT}{\Omega}\ln\left(\frac{P_V}{P_S}\right) = \frac{kT}{\Omega}\ln(1+S)\qquad\qquad\qquad (2.4)$$

Where k is the Boltzman constant, the T the absolute temperature, Ω is the atomic volume (volume per atom), P_V is the actual pressure in the gas phase, P_S is the saturated vapor pressure at equilibrium and $S = \dfrac{P_V - P_S}{P_S}$ is the supersaturation degree. When a nucleus reach the critical size it is stable and can be grown further. In other words at that point the growth of the cluster is no longer limited by nucleation, but by diffusion.

2.2.3 From adatoms to film growth

When each atom arrives and attaches to the surface, it resides within an energy well and it is separated from adjacent wells by an energy barrier. Because of the thermal energy, atoms are hoping at their positions and may jump to neighboring positions due to thermal

fluctuations. Surface diffusion is the result of these jumps across the surface. Up to now we considered the surface as a perfect flat surface and in that case the surface diffusion is happening without mass transport along it. If the surface is not ideal and has defects, such as crystallographic steps or dislocation line terminations, there is possibility for easy attachment of the atoms onto these nucleation sites. These sites can serve as nucleation centers and then we deal with heterogeneous nucleation. On the other hand, if the spacing of the defects is large enough, the surface migrating atoms are lowering the free energy of the system by binding together to form clusters. This is the case of homogeneous nucleation.

Consider having a number of atoms forming a cluster on the surface. This cluster will either grow to become an island or tend to disperse. This behavior is dominating by the free energy reduction of the system. The atoms inside the cluster are fully incorporated while the atoms on the perimeter are not. The different contribution to the reduction of the free energy by the inner and outer atoms is the driving force for the cluster behavior. There is a critical number of atoms which below that number the cluster will disperse, while on the other hand above that number the cluster will grow and become an island, as we have described in the previous paragraph. In real conditions, many clusters disperse for each one that grows to an island. Another important energy factor concerns the propensity for atoms to bond with the substrate and each other. Depending on this parameter, atoms can grow by planar or 2D growth (Frank-van der Merwe - FM mode) where the atoms on the surface approach to each other and stick on the perimeter of the cluster. In contrast if it is more possible to bond with each other and not to the substrate, the atoms will form three dimensional (3D) cluster on the surface. This is the Volmer-Weber (WM) mode of growth. Also there is additional growth mode, which is combination of the above, such as the island on layer mode, or the Stranski-Krastonov (SK) growth (figure 2.5).
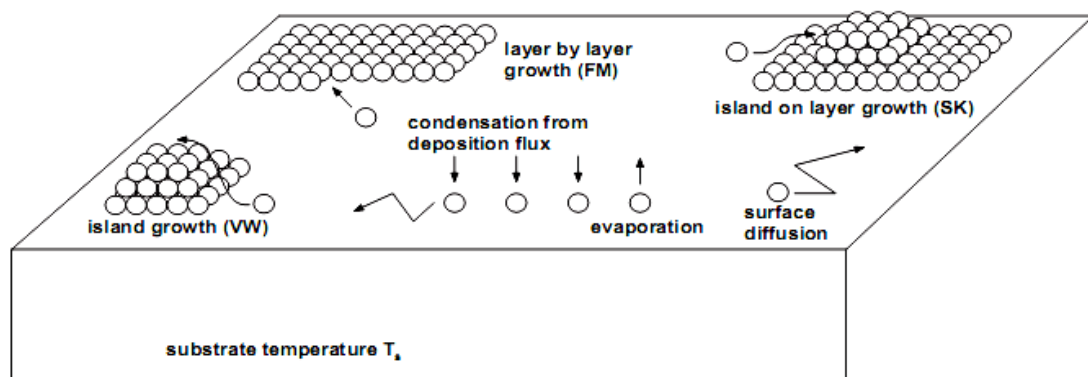
Figure 2.5: Schematic of the mechanisms leading to film growth. Initially condensation should overcome evaporation and second the surface diffusion process which leads to the three different growth modes of thin films (FM, VW, SK)[4].

Summarizing, during film growth the above described energetic parameters determine the final microstructure of the thin film. The possible types of microstructure are described below, at the next part of this chapter.

2.3 Thin film microstructures

As described in the preceding section, the early stages of film growth, under ideal conditions can lead to a specific growth mode, depending on the materials involved, the substrate temperature and the degree of the supersaturation of the vapor. Generally the deposition of thin films is heavily depending on kinetic processes which are not fully understood.

Possibly, the major parameters that influence the final grain structure of a thin film onto a substrate, is the substrate temperature, the growth flux and the kinetic energy of the arriving species. The growth flux is a parameter which describes the mass or the momentum or the volume transfer rate onto the growth surface. This is closely related to the degree of saturation of the vapor as described on the previous part of this chapter.

It is generally accepted that increasing the growth flux a finer scale structure is promoted, while increasing the substrate temperature leads to a coarser microstructure or a single crystal growth. These microstructures will be discussed in a qualitative way below.

2.3.1 Epitaxial films

Epitaxial films are the first case we are going to describe at the section of thin films' microstructure. Epitaxy is a Greek word meaning "to arrange on top" and the epitaxial growth refers to continuation of the crystal structure of the substrate to the crystal of the thin film. A more precise definition about the epitaxial growth is that the atoms on each side of the interface occupy the natural crystal positions. Additionally the interface there is called epitaxial interface. The epitaxial growth of thin film from the same material as the substrate is called homoepitaxy, while on the other hand the growth of a different material on the substrate is called heteroepitaxy (figure 2.6). Generally, the epitaxial films are films with excellent crystal quality, ideal interfaces and they have already found many applications in microelectronics and optoelectronics.

In heteroepitaxy the crystal structure of the substrate is providing the template for positioning the incoming atoms. Consequently, the newly formed layer will provide the

template for the next one. The growth mode in this case is the FM mode as described earlier, which has an average growth flux and high mobility of adatoms. The high temperature of the substrate provides high mobility to the adatoms to find the position of the minimum energy, and the moderate growth flux is providing the necessary time and space for that, since a high flux could block or stop the adatoms from finding that position.

Another important factor that rules the heteroepitaxial growth is the lattice mismatch of the materials. Usually, in stress-free situations, there is a mismatch between the lattice parameter of the substrate and the lattice of the film, in the dimension parallel to interface. However the atoms of the film are positioning themselves in order with the atoms of the substrate, continuing the crystal structure. This can be done but consequently it induces elastic strain to the film. If the mismatch is small, e.g 0.5% or lower, the heteroepitaxial growth can be accomplished. This is happening because the chemical bonding energy per atom is much higher than the elastic energy per atom. So in cases where the strain is small (below 0.5%), the bonding effect is dominating and the material is taking the necessary strain to continue the crystal structure.
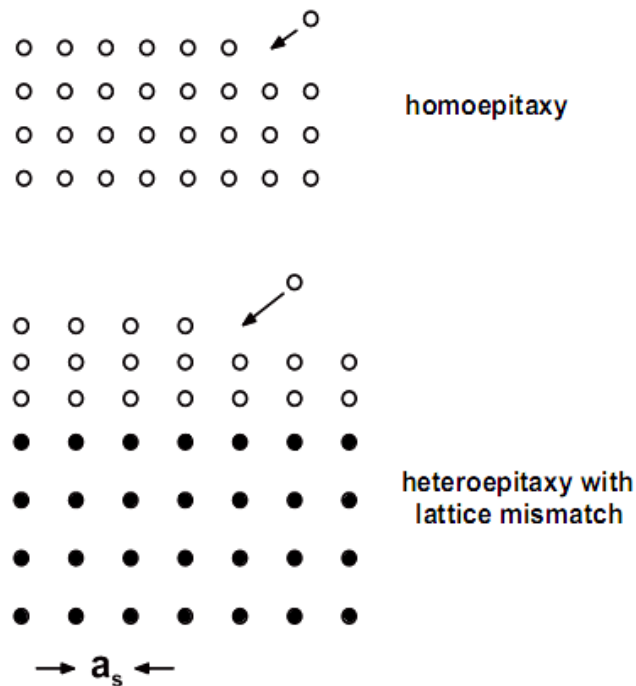
Figure 2.6: Homoepitaxy and heteroepitaxy[4].

If the strain is too large the elastic parameter is becoming dominant preventing the atoms to stick to crystal positions of the substrate. In this case heteroepitaxy can not be accomplished.

When the thickness of the heteroepitaxial film is increasing, the material is having the same strain over the total thickness. Thus the strain energy per unit volume is constant. But

the strain energy per unit area is increasing linearly at the interface with the film thickness. This increasing energy can cause many relaxation phenomena of elastic strain, such as dislocations, twins etc.

2.3.2 Polycrystalline films

As described above in order to obtain epitaxial thin films it is necessary to give to adatoms the required thermal energy, as well as the time and space to diffuse onto the growth surface and find the equilibrium positions. Also the small lattice mismatch between the film and the substrate in addition to the high possibility to bond the incoming atoms with the substrate is required to have the epitaxial films. But in most realistic cases these conditions are not fulfilled, then it is more likely that the deposition follows the VM mode, where the adatoms prefer to bond to each other and then they form three dimensional clusters on the surface. This mode of growth usually results to a polycrystalline film. A polycrystalline film is a film consisting of grains of the same material but with different crystallographic orientations. The main characteristic of the polycrystalline films is the grain structure which includes the grain size distribution, the distribution of crystallographic orientations of the grains (texture) and the grain morphology (grain shape).

All the above characteristics are correlated with the deposition parameters and are quite known for many types of material deposition. As described before, two of the most important parameters which determine the final microstructure of the thin film are the growth flux and the substrate temperature. Additionally other parameters of the deposition, are the time interval between collisions between adatoms of the deposited surface, as well as the ratio of the substrate temperature during deposition to the melting point temperature of the film. These parameters can also have a significant effect on the structure of the deposited film since they give the required energy for the adatoms to find and settle to the positions of lower energy and consequently resulting to grains with minimum energy morphology.

The growth of polycrystalline films begins initially with the nucleation of adatoms into small clusters on the deposited surface. The crystallographic orientation of these clusters may vary and it is a result of the minimization process of the interface and surface energy. This means that the nucleation rate is favored for the clusters with lower energy than with higher. Also the free energy per atoms decreases for clusters with higher volume so the nucleation rate of larger clusters is higher comparing to smaller ones. This is also known as Ostwald ripening[6] and the result is the growth of big clusters is favoring at expense of the smaller ones which finally disperse.

As the islands increase in size they finally come in contact with each other. If the energy of the joining clusters is not enough to align together their crystallographic orientation, then they continue to growth with an intervening interface, the grain boundary.

2.3.3 Structure zone models

A phenomenological summary of rules concerning the growth evolution of the grains is called structure zone model and can be used to predict the final microstructure of the deposited film as a function of various deposition parameters. The first idea for an SZD was introduced by Movchan and Demchishin[7] in 1969 for very thick films produced by evaporation. This SZM has three separate regions of microstructure as a function of the ratio between the deposition and the melting ctemperature. Barna and Adamik[8] introduced a transition zone T between zones 1 and 2. This transition zone includes the competitive growth and the V-shaped grains. It was obvious that a more realistic SZD should include more parameters for better description of the observed thin film microstructures. Thornton has proposed another SZM[9,10] which become classic for sputter deposition. The new SZM has a new variable parameter, the pressure which can serve as a manner of expressing the growth flux to the deposition surface; higher pressure means lower kinetic energy of transferred atom due to collisions. Thornton has based his results on the sputtering technique and his proposed SZM is shown in figure 2.7.
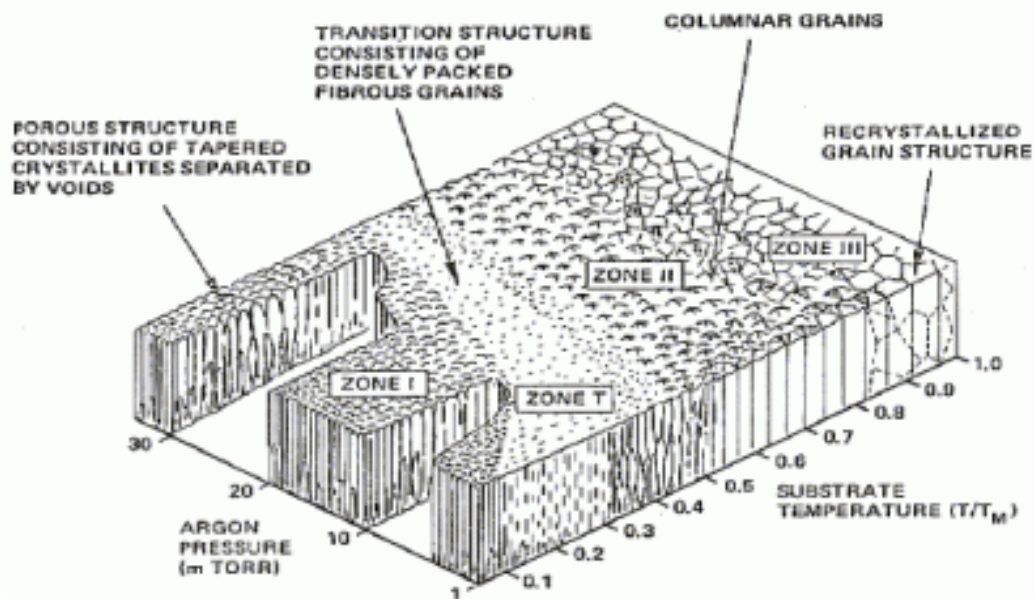
Figure 2.7: Structure zone model proposed by Thornton[9,10].

The zone I describes deposition under low energetic conditions resulting in fibrous grains and voided grain boundaries with high roughness of the film. The transition zone is describing a film with higher grain boundary density, and high density of dislocations. Increasing the mobility of adatoms on the surface the final microstructure is described by columnar grains where the surface diffusion plays a significant role and this is the main characteristics of Zone II. Increasing further the energy of adatoms, the surface diffusion is becoming bulk diffusion as well as recrystallization, leading to formation of large equiaxed grains like Zone III.

Other SZMs[11,12] have been proposed to describe the newly observed microstructures since the ion beam assistance in sputtering systems has made the margins of each zone not distinct. One of the recent SZM[13] is the one shown in figure 2.8 which is shown the microstructure as a function of the generalized kinetic energy E^* (parameter which describes the energy flux by terms of momentum and mass) and the generalized temperature T^*.
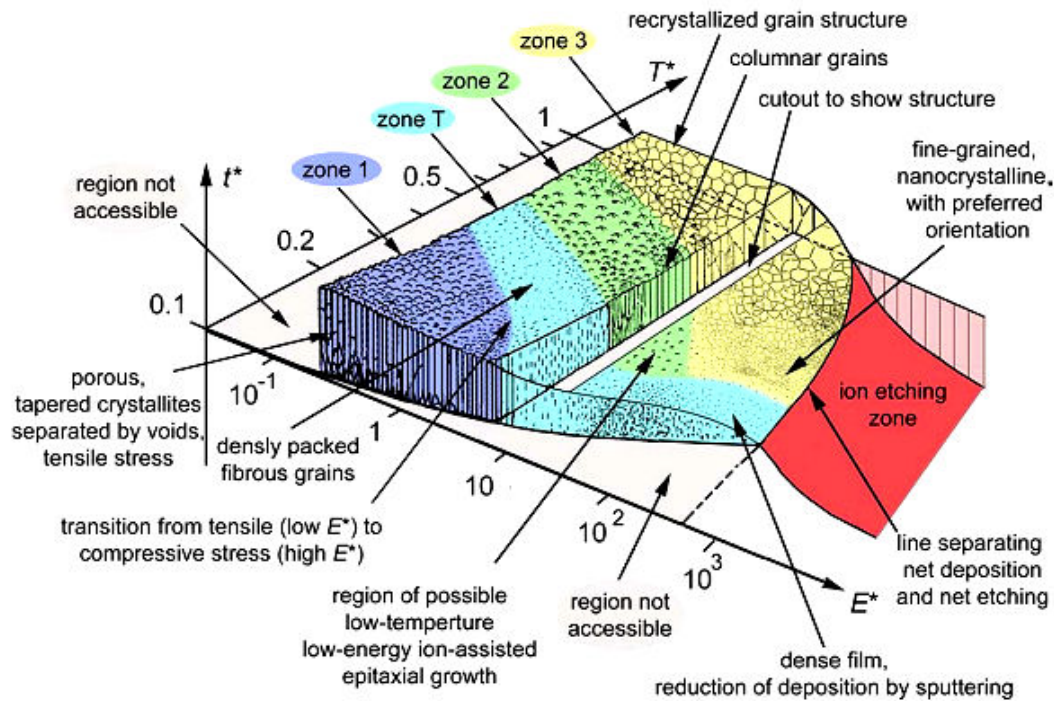
Figure 2.8: Extended Structural Zone Model[13].

2.3.4 Stress origins in thin films

In general, residual stress refers to the internal stress distribution present in a material when the material is free from external forces. Practically, any layer attached to a substrate

supports some state of residual stress. The presence of the residual stress implies that if the substrate was removed the film would change its shape to relax the stress.

There are two types of stresses present in thin films, the intrinsic stresses which are the stress present in films grown on substrates or on adjacent layers. These stresses are dependent on the materials involved, the deposition parameters and the growth flux during deposition. The other kind of residual stresses includes the induced or the extrinsic stresses. These stresses are arising from changes in the physical environment of the film material after the deposition (i.e air exposure). The residual stress of a film is the addition of the intrinsic and the extrinsic stresses. Usually after deposition (where temperature is higher than RT) the only extrinsic stress contribution comes from the thermal stress which originates from the difference in the thermal expansion coefficient between the substrate and the film. If the difference in coefficients is large and the temperature during deposition quite large, the thermal stress can be a few GPa in magnitude. The equation of the thermal stress is:

$$\sigma_{th} = \frac{E}{1-v} \int_{T_{Dep}}^{T_{RT}} \alpha_s(T) - \alpha_f(T) dT \ , \hspace{3cm} (2.5)$$

where $\alpha_s(T)$ and $\alpha_f(T)$ are the thermal expansion coefficients of the substrate and the film respectively, E and v are the elastic constants of the film (Young modulus and Poisson ratio), integrated between deposition T_{Dep} and room T_{RT} temperatures.

The most common mechanisms among others for stress generation during thin film deposition are [4,14-19]:

    — grain growth, or grain boundary area reduction

    — shrinkage of grain boundary voids

    — structural damage as a result of sputtering or other energetic deposition process

    — capillary effect

These mechanisms have been noticed during evaporation of high mobility metals. These materials during deposition exhibit a sequence of compressive-tensile-compressive stress behavior. Low mobility metals do not change to compressive state but continue to evolve in large tensile stress during thickening.

Refractory materials during energetic deposition like sputtering or pulsed laser deposition, exhibit large compressive stress which can go up to several GPa. Therefore during deposition of these materials there are two major competitive stress generation mechanisms.

The first mechanism arises from the atomic-peening process[20], which is the result of the energetic bombardment of the film during deposition bombardment. This process induces lattice parameter dilatation due to the creation of point defects[21] in the crystal of the film. In a free standing layer the effect would be the expansion of the film's dimensions to compensate the excess volume. But in an adherent film this is not possible and the result is a compressive stress state.

The second stress generation mechanism is the grain boundaries attractive forces between grains during the coalescence stage of growth. In figure 2.9 it is shown the sequence of a thin film growth. The first stage if the nucleation followed by the coalescence stage.
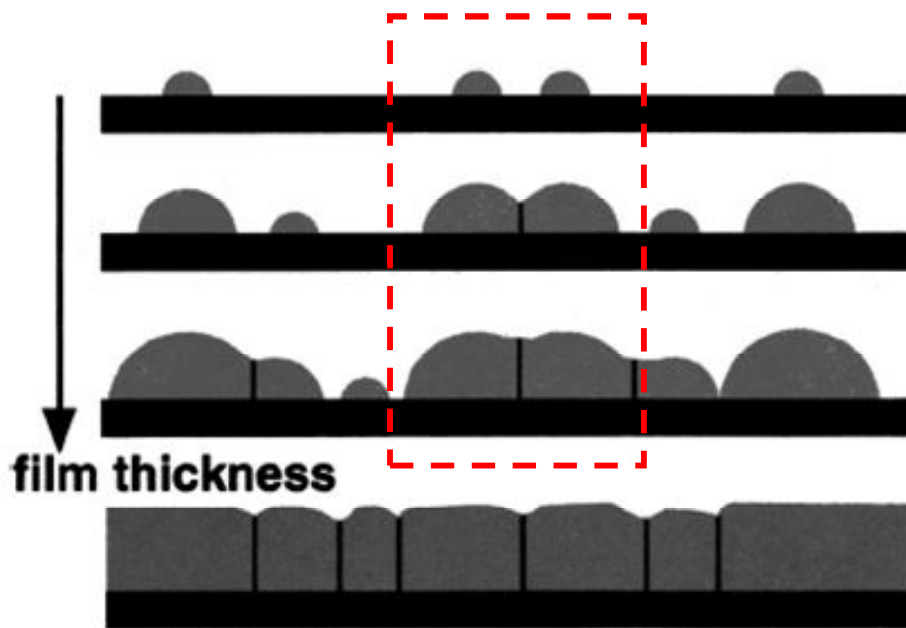
Figure 2.9: Early stages of film growth from nucleation (top) to coalesence and (middle) and up to film growth (bottom)[14].

During coalescence when two neighboring islands approach each other, the system wants to minimize the free surface. This imposes an elastic deformation of the atoms near the boundary. These elastic deformations produce a strain field which act in opposite directions but the continuous form of the film implies that the total film suffer from tensile stress. In figure 2.10 it is shown more clearly how the island boundaries are strained to minimize the free surface. When the adatom mobility is quite high, during coalescence the atoms diffuse rapidly towards the gap and relieve the stress from the elastic deformation.

This coalescence process is responsible for the tensile stress of the film during the early stages[14,18]. It is a function of the surface free energy, the grain boundary free energy and the elastic properties of the material. Thus, during the film thickening, the development of columnar microstructure retains this mechanism since the surface area is high and

38

intercolumnar forces are applied though the whole thickness. Additionally, a more open and voided microstructure enhance this process as the film is thickening further.

In most cases both stress generation mechanisms[18] are present during growth under energetic conditions[22,23]. In addition to the peening process another mechanism which contributes to the compressive stress is the entrapment of neutral gas atoms such as Ar in case of sputtering. The rate of entrapment of argon is affected by the kinetic energy of Ar and it is constant during film thickening and does not change the stress evolution. But a film grown in the zone T with the competitive grain growth can show a stress evolution during thickening[24].
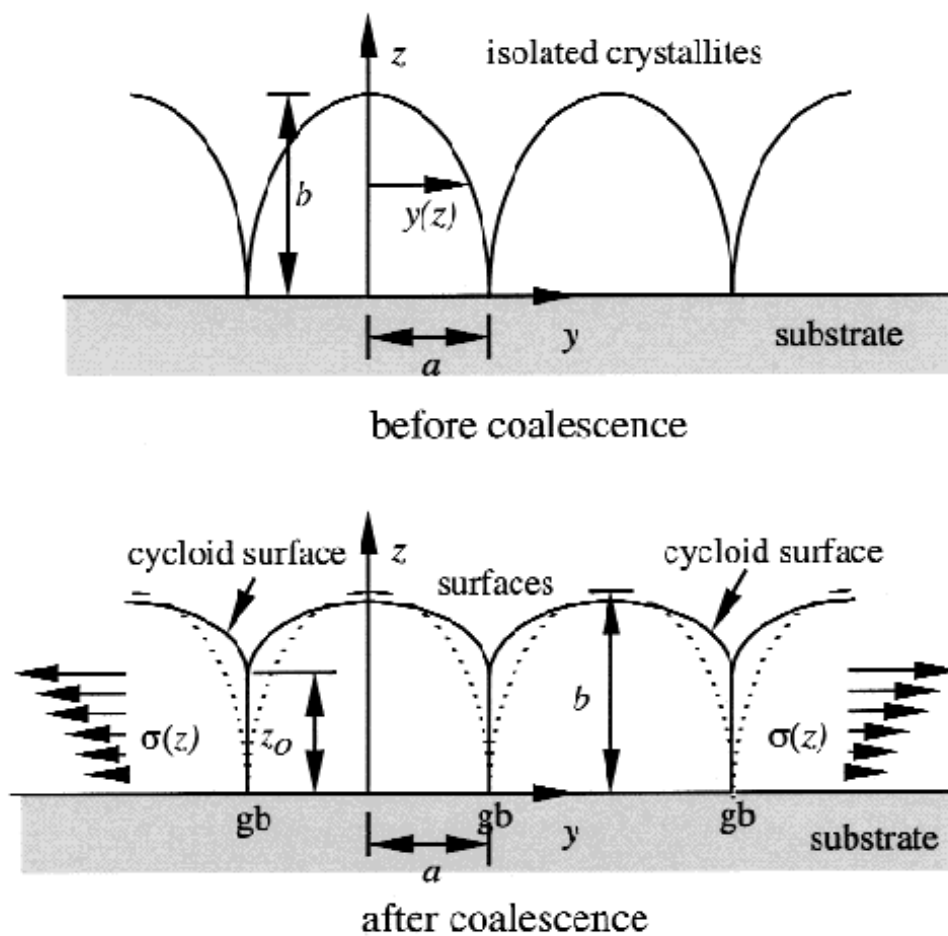
Figure 2.10: Two snapshots of film growth stage; just before and right after coalescence[18].

Section II: Physical vapor deposition techniques (PVD)

2.4 Introduction

PVD techniques rely on the creation of vapors from a solid source as a consequence of physical processes i.e melting, evaporation, or collisions. The transfer of supersaturated vapors and the condensation on a surface result to thin film growth. The way the vapors are created and the transfer through the gas phase is correlated with the growth flux which is responsible for the final microstructure of the thin film. In this section, we are going to describe the three PVD techniques used in the framework of the current thesis.

2.5 Sputter deposition

In general, sputtering is a process where atoms are ejected from a solid as a result of the energetic bombardment of the solid with particles. The transfer of these ejected atoms onto a surface is the sputtering deposition technique.
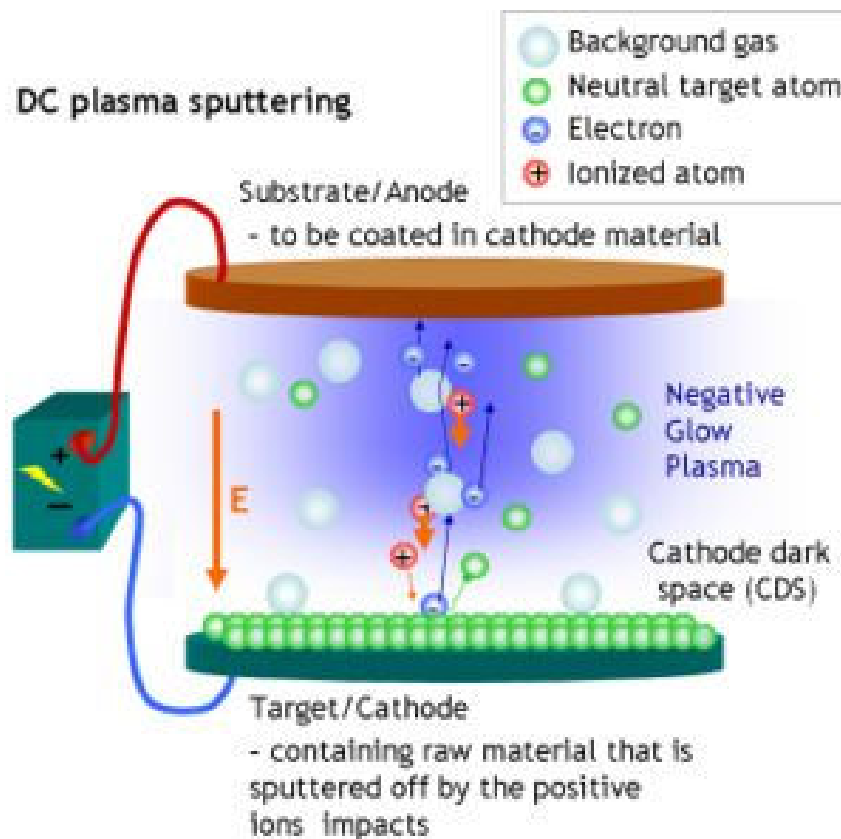
Figure 2.11: The basic configuration of a sputtering deposition chamber. (figure from www.etafilm.com).

The sputtering deposition is a very common technique for thin film growth. In that method, ions of a sputtering gas, typically Ar, are accelerated towards the target by an imposed electric field. The collision of the accelerated ions at the target surface is extracting atoms, which are traveling inside the chamber and finally condensed to the substrate surface, providing film growth. Nowadays, various sputtering-based deposition techniques are used, such as dc-sputtering, rf-sputtering, magnetron sputtering, pulsed DC sputtering, HIPIMS *etc*, but all of them rely on that main principle. Differences between these techniques arise in power supply type applied to the target, such as direct current, radio-frequency supply and the use of magnets. Below we are going to describe qualitatively all the main characteristics of the sputtering technique used in the framework of the present thesis.

In figure 2.11 it is shown the deposition chamber which consists of a sputtering elemental target, a substrate (usually Si) for the film deposition, and inlets for injection and pumping of the gases. The sputtering gas is usually a noble gas (Ar, Xe, Kr) and specifically in our case is Ar.

Initially the gas is inserted into the deposition chamber. Afterwards an electric field is imposed between the target and the substrate resulting to the ionization of the Ar gas and the creation of plasma. The plasma is consisting of neutrals, electrons and a small fraction of ionized Ar atoms which are accelerating to the target due to the imposed electric field and to the interactions with mobile electrons. The collisions of the Ar ions onto the target facilitate the transfer of momentum to the atoms on the surface. This momentum transfer enables the collision cascades in the vicinity of the surface. When such a cascade recoils and moves towards the surface and has more energy than the surface binding energy, atoms are ejected from the solid to the gas phase having a substantial kinetic energy. This kinetic energy of the outcoming atoms varies between a few eV to hundreds of eV. These atoms are creating the supersaturated vapor inside the chamber and are condensed onto the substrate providing the film growth. Following the above process, we are going to describe the phenomena divided in three sections. First we are going to describe about the **sputtering on the target**, secondly about the **travel into the gas phase** and finally the **processes on the deposition surface**, according to the figure 2.3.

2.5.1 Sputtering on the target section

One of the major parameters of the conventional sputtering deposition is the power supply to the target. In order to create the plasma above the target we need to supply a negative voltage to the target. The imposed electric field is separating charge carriers, the

ionized gas atoms and their electrons. The positive charged gas atoms are moved towards the (negatively charged) target resulting to collisions on the gas phase (ionizing more gas atoms and consequently stabilizing the plasma) and on the target, resulting to surface erosion, while electrons are accelerated to the anode. The power supply of the target can be either a direct-current (DC) or radio frequency (RF) supply. Particularly the RF supply is used for insulating targets in order to avoid charge build-ups on the surface. This is happening because the incoming particles from the plasma have charge which cannot be accommodated by the insulator target.   The power supplied on a target has a linear correlation with the deposition rate of the film. The more power applied to the target, the more collisions on the target surfaces from the plasma. The result is the increased rate of target erosion and consequently higher deposition rate. Also the increase of power supply on the target increases generally the kinetic energy of all particles involved in the deposition. The average number of atoms ejected from the target per incident ion is called sputtering yield.
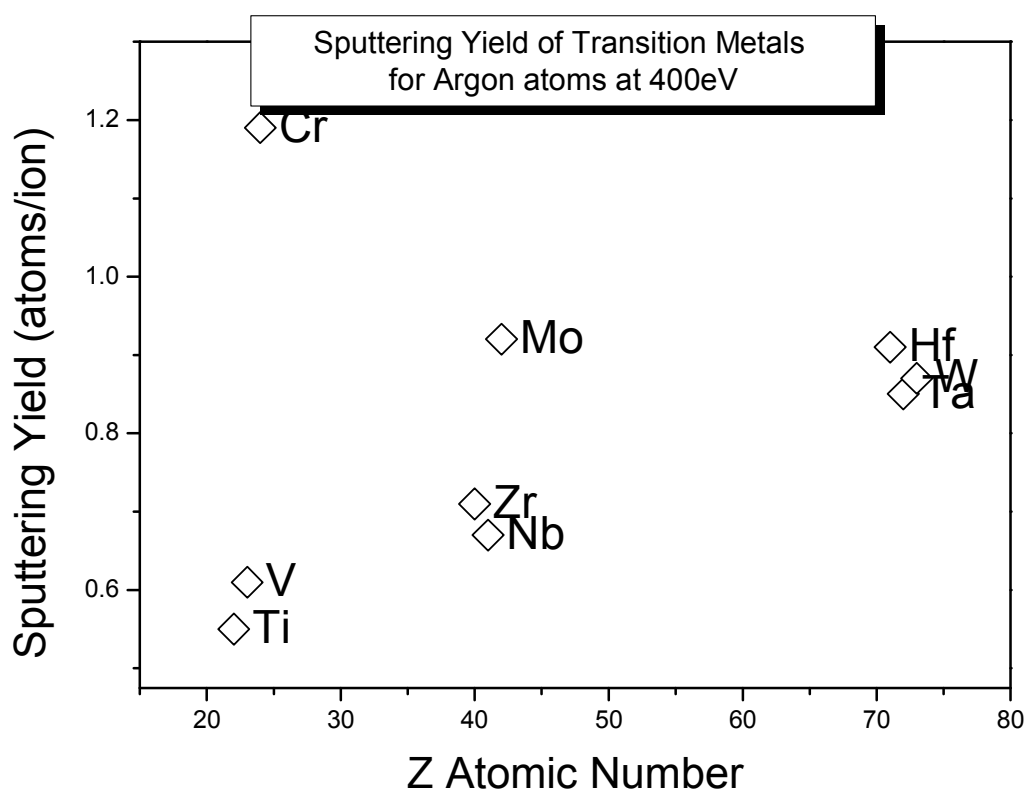
Figure 2.12: Sputtering yields of transition metals for argon ions at 400eV impinging energy. These values have been calculated from SRIM software.

Usually the sputtering gas used in sputtering systems is the Argon. This has been chosen for its inertness and its large size (higher efficiency of momentum transfer to the target). For light elements the sputtering gas can be He, and for heavier Kr or Xe is used.

Some typical values (SRIM[25] calculations) of the sputtering yield of the transition metals for Ar plasma at a common kinetic energy 400eV are shown in figure 2.12.

The sputtering mechanism (the ejection of matter from a solid) is only one result in case of ion bombardment of a solid. Other phenomena can also take place during ion bombardment. These phenomena include the emission of secondary electrons from the atoms of the target, the creation of vacancies and defects in the target structure, the formation of compounds on the target, the implantation of the incoming particles or the backscattering of some of them. The most important of these phenomena are shown in figure 2.13.
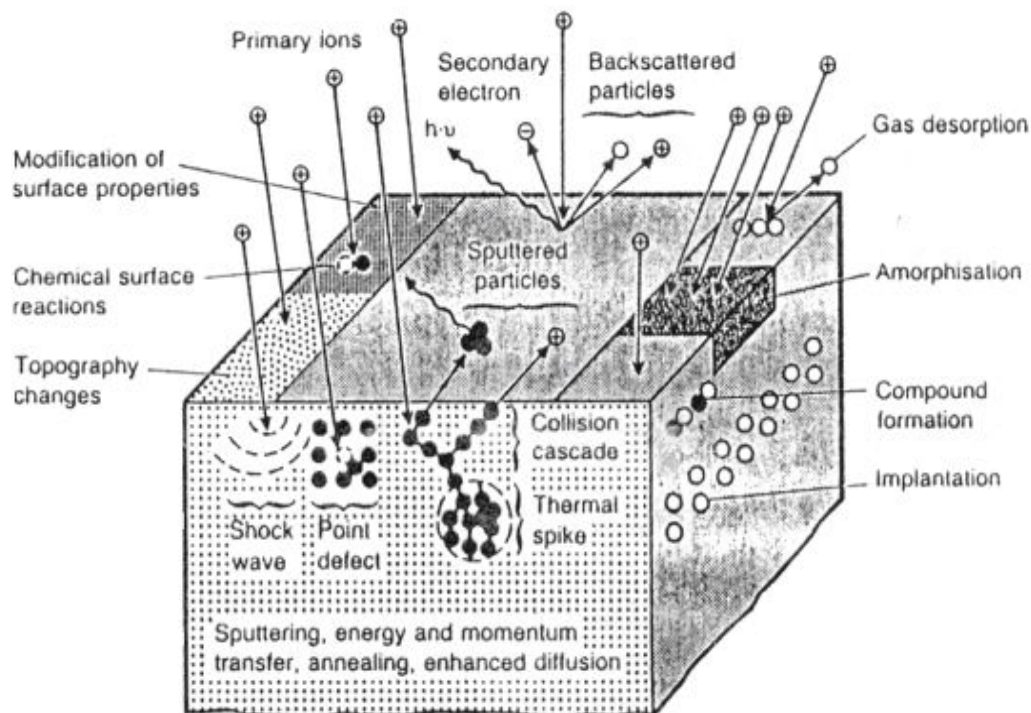
Figure 2.13: Interactions of ions with a solid.

Another process that is taking place during the sputtering of a target is the backscattering process. There is a possibility that a particle moving towards the target, it will be scattered exactly on the opposite direction than the initial. The possibility of occurring that is higher for heavier elements . This means that during the sputtering of a heavy target the backscattering particles of the gas can reach the deposition surface contributing to the growth flux. If the backscattering contribution is high then the final microstructure of the thin film is changing. In table 1 results are shown from SRIM[25] calculations ($1E^6$ atoms at 400eV vertical incidence) revealing that the backscattering process increases as the atomic number increases and can reach a value around 25%.

Table 1: Backscattered particles (%) for the transition metal nitrides of the d-block.

Elements	Ti	V	Cr	Zr	Nb	Mo	Hf	Ta	W
Backscattered Ar (%)	2.6	3.2	3.6	12.6	12.8	13.3	26.0	26.2	26.8

The ionization of the Ar atoms inside the plasma is depending on the number of free electron from the previous ionizations as well as from the secondary electrons ejected from the target. In the classical sputtering technique the majority of these electrons are lost due to collisions on the chamber. In order to avoid that and increase their density close to the target, magnets are placed below the eroded target where the magnetic lines are increasing the concentration of electrons just above the sputtered target increasing the ionization of the plasma at that area. This variation is widely used and the sputtering technique is then called magnetron sputtering. Since this alternative is widely used, the target after several depositions is under heavy erosion, especially on the areas where the secondary electrons concentration is very high.

As mentioned previously there is a possibility to introduce a reactive gas into the deposition chamber to deposit compounds on the substrate. This is the case for sputter deposition of nitrides and oxides. This capability of the technique has also a side effect, the formation of the compound on the surface of the target, which is called poisoning. This process is making the deposition more complex. One of the models describing the process is the Berg's model[26,27] which will be described right after.
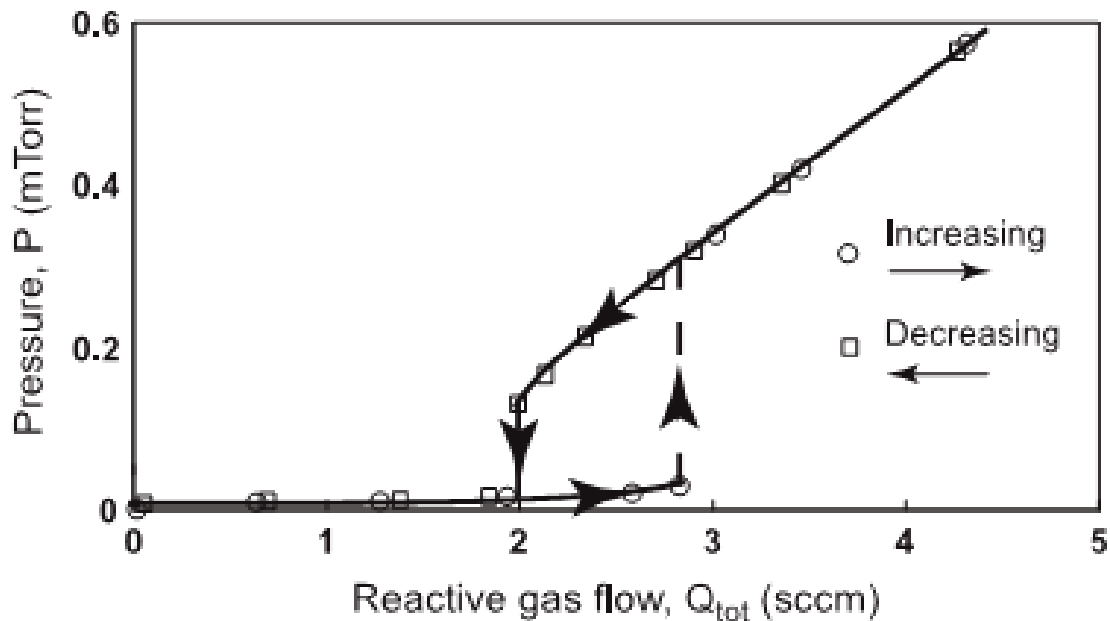
Figure 2.14: Typical experimental curve from a reactive sputtering process. It is shown the pressure of the reactive gas as a function of the reactive gas flow. The round symbols describe the initial increase of the supply of the reactive gas and the cubic the sequential decrease of flow (figure taken from[27]).

Figure 2.14 shows a typical experimental curve of the pressure of the reactive gas as a function of the gas flow to the chamber. The shape of the curve denotes that there is a hysteresis effect of the process. During the increase sequence of the reactive gas, the pressure stays at low level until a rapid burst at some point. During the decrease the pressure stays high even for the same amount of flow and suddenly decreases rapidly again. The separation width between the decrease and increase denotes the width (instability area) of the hysteresis region.

The introduction of small amounts of the reactive gas has a minor increase of the partial pressure in the chamber. This is happening because all the gas is consumed to form the compound with the sputtered particles in the gas phase. When the reactive gas reaches the equilibrium pressure for the compound formation in the gas phase the additional gas is used to create the compound on the sputtered target and the chamber walls. This starts to happen just before the instability region. Additional gas is used to form the compound on the target surface. The pressure of the reactive gas is still low due to the consumption on the target. When a significant fraction of the target surface area is fully covered with the compound the pressure increases rapidly. This is happening because the sputtering yield of the compound formed on the target is (usually) lower than the pure element. So the target erosion is lower and the available sputtered atoms on the gas phase are fewer. This provides the extra amount of reactive gas into the chamber increasing rapidly the pressure. The partial pressure after that point increases almost linearly as a function of the pumping speed of the chamber, so if were observed in the absence of plasma.

The inverse sequence is described similarly. The reduction in the supply of the reactive gas is denoted by a reduction in the partial pressure having the same values as before. When the value of gas flow reaches the previous point of rapid increase the pressure the amount of gas is not enough to completely form the compound on the target surface. Thus a small fraction of target area returns to elemental form (the continuous sputtering is dissociates the compound) increasing the erosion rate and consequently the consumption of the reactive gas. When a significant portion of the target's area is exposed to plasma in the elemental form, the higher supply of sputtered atoms consumes the reactive gas and lowering rapidly the partial pressure.

Almost all the parameters involved in the reactive sputtering have a minor or major effect on the hysteresis curve. The complete description of the contribution of each parameter is described in the paper of S. Berg and T. Nyberg[27].

2.5.2 Processes on the gas phase

The gas phase is the medium for the transfer of matter onto the deposition surface. Here the ejected particles from the solid target are subjected to collisions only with the gas atoms. The presence of other sputtered particles as well as other gas atoms (reactive gas) is neglected since their concentration is very low. These collisions are reducing the kinetic energy of the sputtered particles. If the particles subject to heavy collisions then they get "thermalise" taking the average kinetic energy of the surrounding gas atoms. Consequently by changing the pressure of the sputtering gas we can increase or decrease the collisions on the gas phase of the particles before reaching the deposition surface. The mean free path[28,29] [λ] is a parameter showing the average distance traveled by particles between subsequent collisions. The equation which gives the mean free path of an atom with mass M_s, traveling through a gas with mass M_g is:

$$\lambda = E^a \left/ \left(\pi \frac{P_g}{kT} \left(r_s + r_g \right)^2 \left(1 + \frac{M_s}{M_g} \right)^{1/2} \right) \right. \tag{2.6}$$

Where E is the kinetic energy of the sputtered particle, a is a constant ($a = 0.29$), P_g the pressure of the gas atoms and r_s and r_g the atom radius of the sputtered atom and the gas atom respectively.

The mean free path is an energy dependent parameter[28] and it is a function of the masses of the sputtering gas and the solid, their relative atomic radius, the kinetic energy of the sputtered particles and the pressure. Also there is another parameter (proposed by W.D.Westwood[29]) that is an estimation of the energy loss per collision and the average collision required for the sputtered particles to get "thermalised", which means to obtain the same kinetic energy of the surrounding gas. Based on the equation 2.6, in figure 2.15 it is shown the mean free path of zirconium atoms in Ar environment.
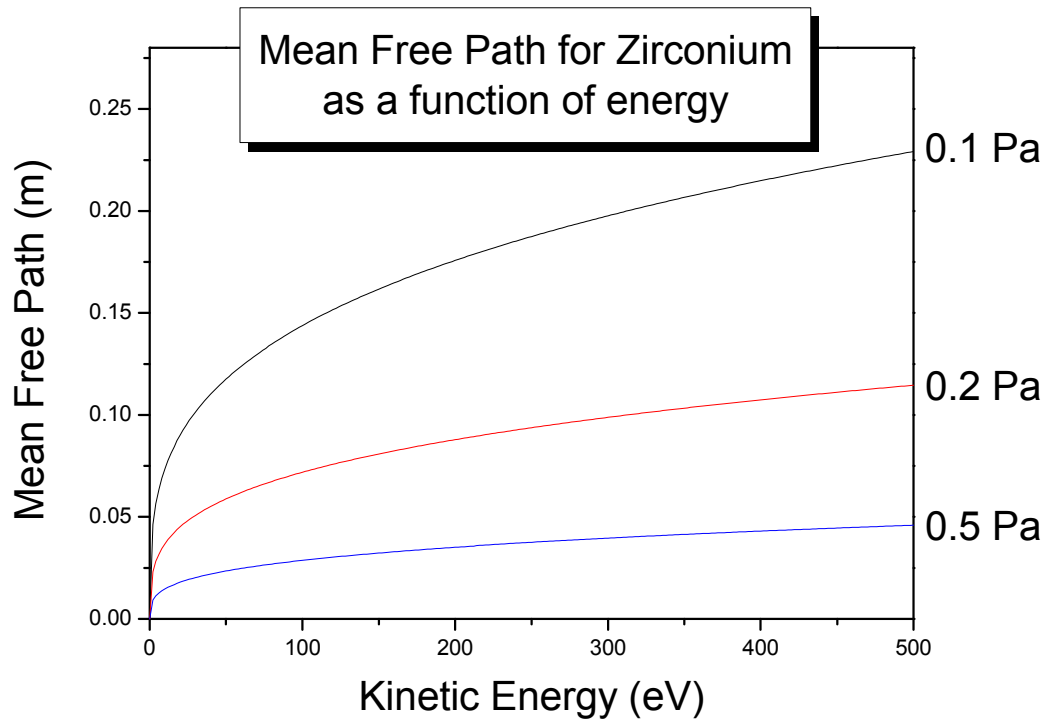
Figure 2.15: Mean free path calculations for zirconium atoms as a function of energy. The calculations have been performed using the equation 2.6.

During sputtering of a target, the incoming ions from the plasma are accelerating by the plasma discharge voltage. The distribution of their kinetic energies has a peak at around 75% of that voltage. Considering some typical values of discharge voltage which are 200-500 V, the majority of the accelerating gas ions have a kinetic energy about the 75% of the voltage applied. The sputtered atoms have a kinetic energy correlated with the energy of the incoming gas atoms. These energies are used to calculate the energy dependent mean free path in a given pressure.

2.5.3 Processes on the deposition surface

The final quest of the deposition technique is to deposit a film with a desired microstructure on the substrate. This is done by controlling all the parameters described before. These parameters have an effect on the growth flux, which is dominating the microstructure of the film. On this final section we are going to describe the processes on the deposition surface to ensure that all the mechanisms are taken into account.

The first one is the substrate temperature which is a major parameter for the final microstructure of the film. The high substrate temperature is providing to the adatoms the required energy to diffuse rapidly and find the minimal energy positions. As told before the behavior is material dependent, for the nitrides, which are refractory materials, with very

strong bonds, almost all the energy provided to adatoms is coming from the kinetic energy of the incoming particles and not from the substrate heating which is very low compared to their melting point. For quantitative reasons the ratio between the substrate temperature and the melting temperature of the material is about 0.1 (T_m~3000° C, T_s=300° C).

The kinetic energy of the incoming particles can be in the range of a few eV but sometimes it can reach up to hundred of eV. Particles with such energy can implant directly inside the substrate in a depth according to their kinetic energy. There is a surface energy threshold[30] where atoms with kinetic energy below that do not succeed to implant; this threshold is about 50eV. Atoms with higher kinetic energy can implant under the deposition surface forming compounds or create defects. Except the sputtered atoms, atoms from the sputtering gas can reach the deposition surface. This is the result of the backscattering process which occurs on target. These backscattering particles often have high energy and get entrapped in the film via a subplantation process. A big amount of backscattered particles can increase significantly the energy flux changing the microstructure of the film. In general the high kinetic energy of the incoming particles on the deposition surface induces defects which affect the stress state of the films. Another effect of the high energetic flux to the deposition surface is the re-sputtering of the already deposited film, which affects except the microstructure even the formation of the film.

Another way to control the energy flux to the deposition surface is to apply a negative voltage to the latter. This extra electric field attracts the charged sputtered species and controls their kinetic energy. Additionally, this electric field pushes away any electrons from the plasma avoiding pilling up negative charge on the deposition surface.

2.6 Ion beam sputtering

The ion beam sputtering is an alternative to the classical sputtering technique. Here the target is sputtered by a beam of ions created elsewhere and not on the vicinity of the target. The advantage of this process is that the ion beam can be controlled independently than the plasma in terms of kinetic energy and flux. Additionally there is the possibility of adding one more assistive ion beam for extra functionality and for inducing chemical reaction (reactive gas). The deposition technique then is called dual ion beam sputtering (DIBS). In the figure 2.16, the basic configuration of DIBS can be seen; the configuration includes the main ion source, the target, the substrate and finally the secondary ion source.
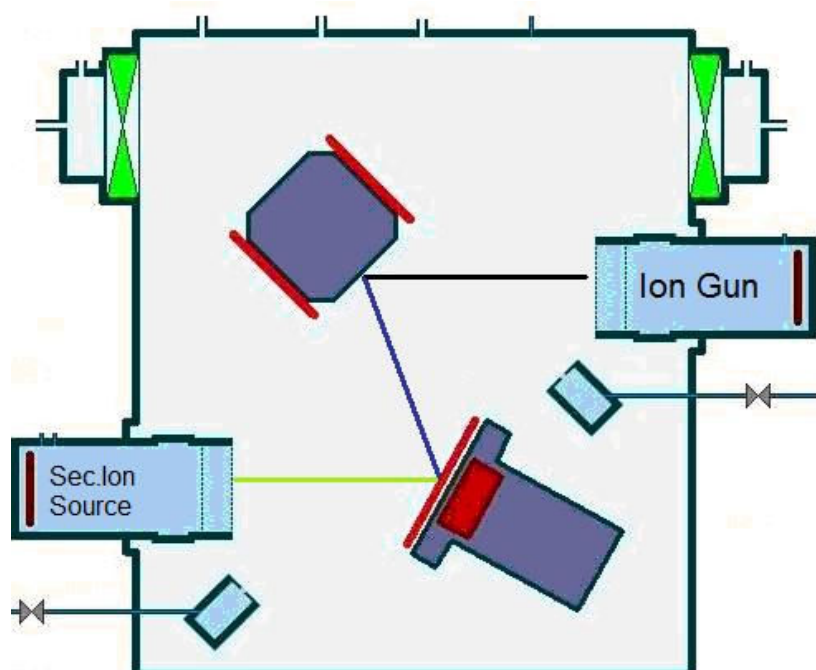
Figure 2.16: The basic configuration of a dual ion beam sputtering chamber.

Initially the primary ion beam is directed on the target where it causes cascades and recoils like the classical sputtering. The ejected particles from the target are transferred to the gas phase. During the arrival of the sputtered particles, from the target to the substrate, there is a second ion beam which is directed towards the substrate. This assisted beam can be used to make compounds if it is consisted of reactive ion species, or to control the deposition by selectively knock off particles which are not attached in equilibrium positions on the surface. Figure 2.17 shows a real image of the DIBS deposition system in P` institute, at the University of Poitiers which has been used to deposit samples inside the framework of the present thesis.

2.6.1 Processes on the target

The difference between the classical sputtering and the ion beam sputtering is the energetic distribution of the incoming particles. By using an ion beam to sputter a target, we can control separately the kinetic energy and the flux of the beam. Usually, the kinetic energy of the ions in the ion beam sputtering is in the range of a few keV. The kinetic energy of the ions has a very narrow distribution. Also the striking angle of the beam can be adjusted in contrast with the classical sputtering technique where the plasma and the target are coupled and the sputtering angle is vertical.
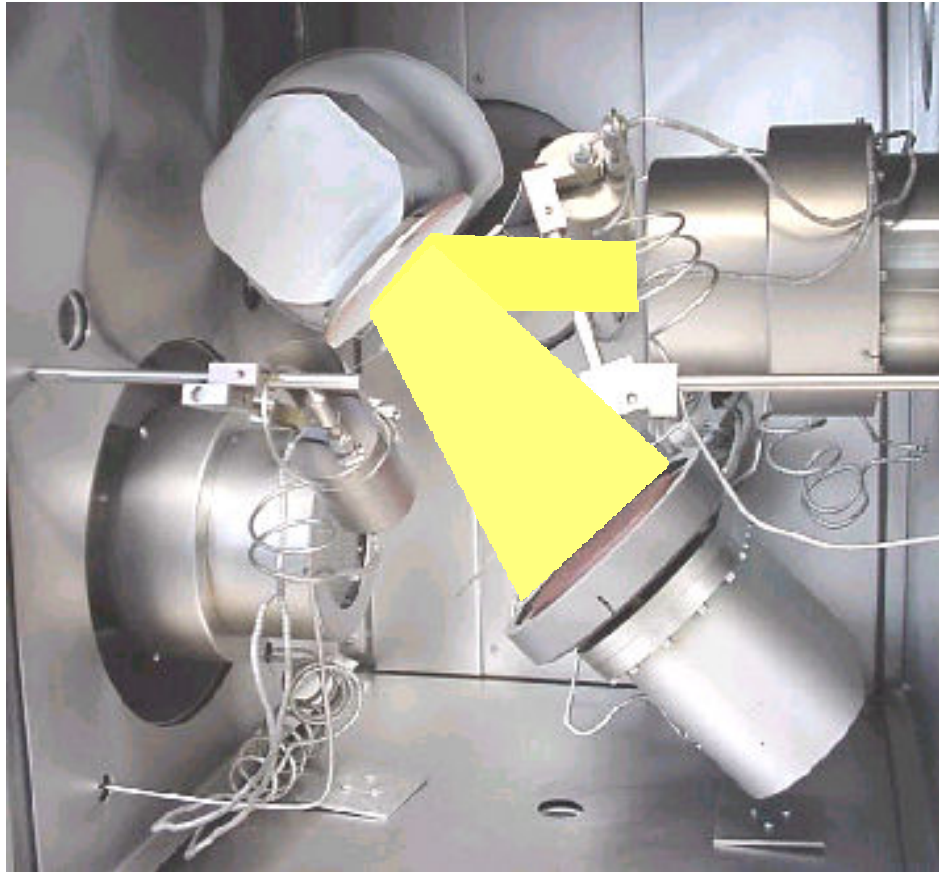
Figure 2.17: Image of the DIBS deposition system. In yellow shade the primary ion beam and the sputtered flux from the target and in red shade the secondary ion beam towards the substrate.

Like the classical sputtering technique, also in ion beam sputtering there is a possibility to insert a reactive gas in the chamber for deposition of oxides, nitrides *etc*. But the versatility of the technique is that someone can use the secondary ion beam to make the compounds and to avoid a reactive gas in the entire chamber and suffer the side effects on the target surface like poisoning. Also the assisted ion beam can be used to control the growth flux to the deposition surface, for the desired microstructure.

As told before there is a possibility the incoming ions to backscatter when hitting the target. This possibility is increasing for elements with high atomic number. But a significant detail is that the ions in the ion beam sputtering are very energetic and their contribution to the growth flux on the deposition surface is very high.

2.6.2 Processes on the gas phase

As already described before, the pressure of the deposition chamber plays a major role on the kinetic energy of the sputtered particles from the target, affecting the growth flux. During the conventional sputtering there is a need for high pressure in order to sustain the

plasma. In the ion beam sputtering there is no such need and the working pressure of the chamber can be quite low, promoting more the energetic conditions, since the gas phase collisions are fewer. These higher energetic conditions are promoting the use of DIBS in the creation of metastable films where the non-equilibrium conditions are essential.

2.6.3 Processes on the deposition surface

During the ion beam sputtering the energy flux on the deposition surface is usually much higher and it is more controllable than in conventional sputtering. The incoming particles are the sputtered particles from the target, the backscattered atoms and the particles from the secondary ion beam. The grower can control separately the contribution to the growth flux arriving to the substrate, from each source leading to a more controllable way of deposition.

The particles from the assisting beam can be used in several ways. Their energy and flux is also controllable and it can be used to make compounds like nitrides, oxides *etc*. Additionally the kinetic energy can be used to prevent the adatoms from finding equilibrium positions on the surface, promoting the creation of metastable films.

2.7 Pulsed laser deposition

Pulsed laser deposition (PLD) is a thin film deposition technique, which belongs to the category of physical vapor deposition techniques. In that technique, a focused high powered pulsed laser beam is striking a solid target inside a vacuum chamber. The solid target is vaporized and the vapors are deposited onto a substrate as a thin film. The basic setup of the technique is quite simple but the physical phenomena between the laser beam and the target is quite complex.

The basic configuration of the PLD technique is shown in figure 2.18. The main characteristics are the laser beam, the focusing lens, the vacuum chamber, the target and the substrate holder. The laser beam has some properties which are very important to the deposition mechanism. These properties are the fluence, i.e the photons energy per unit area per pulse. Usually this fluence is measured in joules per unit area. The second important parameter is the wavelength of the photons and finally the third one is the pulse duration.

(1) Laser Source
(2) Convex Focusing Lens
(3) Quartz Viewport
(4) Laser Beam
(5) Rotating Target
(6) Plume
(7) Rotating Sample Holder
(8) Heating Lamps
(9) Plume Analysis Techniques (Time Of Flight Mass
Spectrometry; Optical Emission Spectroscopy)

(a)

(b)
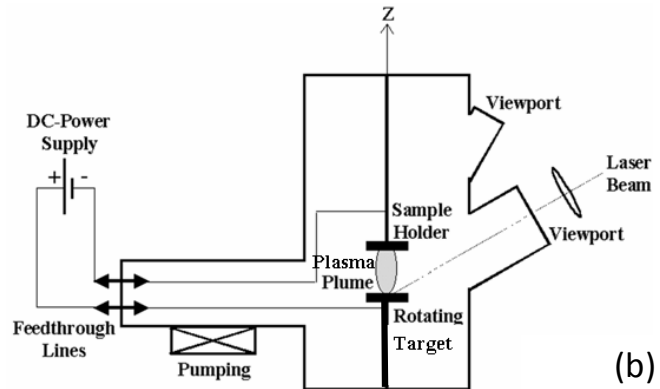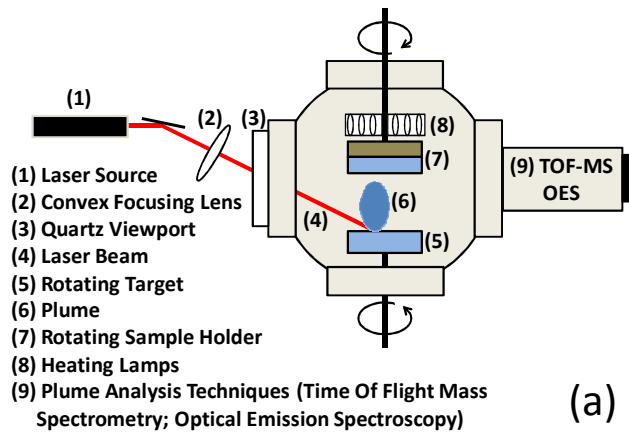
Figure 2.18: (a) The basic set-up of a PLD system. The most important parts are listed in the inset. (b) a real setup of a PLD chamber where there is an external DC supply for controlling the deposition and add extra capabilities[31] .

2.7.1 Processes on the target

The pulsed laser beam is striking the target penetrating a few nanometers inside the bulk, depending on the material refractive index and the energy of the photons. Due to high fluence of the laser beam a multi photon ionization process is happening to the near surface atoms creating a coulomb explosion and formation of plasma; this process lasts a few picoseconds. The free electrons from the ionized surface atoms are oscillating due to the electric field (the pulse duration is larger than 10ps), striking the atoms of the target surface, heating it up and finally evaporating it. This secondary effect can be enhanced or eliminated by selecting the duration of the laser pulse. For a shorter duration of the pulse (in the order of ps), the pulse is finished before the electrons are ejected, thus not providing the oscillating energy to heat the target.
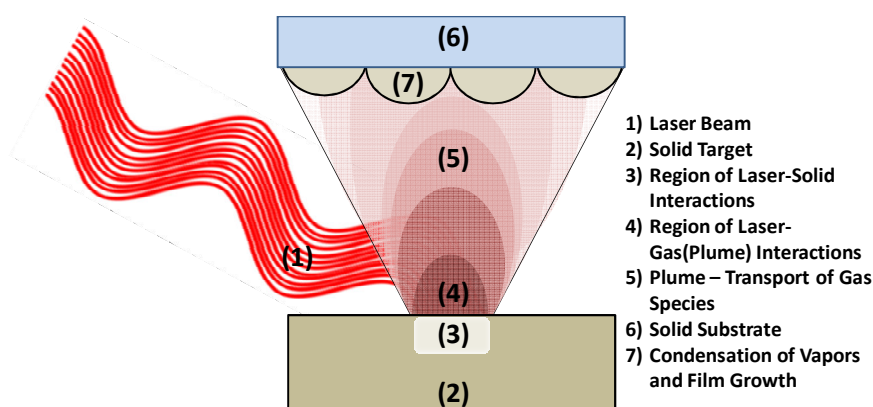
Figure 2.19: A schematic of the laser ablation process and its stages up to thin film formation[31].

The ionization potential is the required amount of energy to remove an electron from an atom at the outermost atomic shell. Thus by selecting the right wavelength of the photons, by the multi-photon excitation we can increase the efficiency of the beam. The ejected mixed species are expanding into the vacuum in a form of a plume. The plume is consisting of many energetic particles such as single atoms, electrons, molecules, ions, cluster of atoms and even molten globules. The ablation of the target and the expansion of the plume is sketched in figure 2.19.

The deposition rate of the PLD technique in a macroscopic scale is very low compared to the sputtering. This is because the *real time* of deposition is during the pulses and not between them. Generally the pulsed laser systems have a repetition rate of a few Hz; and the pulse duration is in the range of nanoseconds. Consequently there is a lot of time when nothing happens on the system and thus the deposition is very low. On the other hand the deposition rate during the pulse is very high, much higher than the other techniques.

2.7.2 Processes on the gas phase

The spatial distribution of the plume is depending on the gas pressure of the deposition chamber. If the pressure is low then the plume is narrow. Increasing the pressure, the species in the plume are subjected to collisions and the plume is having a diffusion-like behavior. The energy of the species of the plume is depending of the pressure exactly as described in the same section for the sputtering technique. The pressure can be controlled by introducing an inert gas inside the chamber. Also, similarly with the reactive magnetron sputtering the introduction of a reactive gas can lead to formation of compounds on the deposition surface; in our case the ablation took place in N_2 ambient in order to form nitrides.

In general the mass transport through the gas phase is subject to certain rules and it is independent of the creation of the vapor from the target. So the difference in PLD than sputtering is that the plume is consisting of not only single atoms but also of clusters.

2.7.3 Processes on the deposition surface

The phenomena on the deposition surface are also similar like the sputtering technique. The only difference is that the incoming species are not single atoms. So the momentum transfer to the surface is much higher. Also another characteristic of the PLD technique is that the nucleation density on the deposition surface is much higher than the sputtering.

References

[1]   A. Pimpinelli and J. Villain, *Physics of Crystal Growth* (Cambridge University Press, 1999).

[2]   J. Y. Tsao, *Materials Fundamentals of Molecular Beam Epitaxy*, 1st ed. (Academic Press, 1992).

[3]   J. A. Venables, *Introduction to Surface and Thin Film Processes*, 1 ed. (Cambridge University Press, 2000).

[4]   L. B. Freund and S. Suresh, *Thin Film Materials: Stress, Defect Formation and Surface Evolution* (Cambridge University Press, 2004).

[5]   C. Herring, Physical Review 82, 87-93 (1951).

[6]   M. Zinke-Allmang, L. C. Feldman, and M. H. Grabow, Surface Science Reports 16, 377-463 (1992).

[7]   B. A. Movchan and A. V. Demchishin, Phys. Met. Metallogr. 28, 653 (1969).

[8]   P. B. Barna and M. Adamik, Thin Solid Films 317, 27-33 (1998).

[9]   J. A. Thornton, J Vac Sci Technol 11, 666-670 (1974).

[10]   J. A. Thornton, Annual Review of Materials Science 7, 239-260 (1977).

[11]   M. Mausbach, Surface and Coatings Technology 74-75, 264-272 (1995).

[12]   J. S. Colligon, Journal of Vacuum Science and Technology A: Vacuum, Surfaces and Films 13, 1649-1657 (1995).

[13]   A. Anders, Thin Solid Films 518, 4087-4090.

[14]   J. A. Floro, S. J. Hearne, J. A. Hunter, P. Kotula, E. Chason, S. C. Seel, and C. V. Thompson, Journal of Applied Physics 89, 4886-4897 (2001).

[15]   R. W. Hoffman, Thin Solid Films 34, 185-190 (1976).

[16]   G. C. A. M. Janssen, Thin Solid Films 515, 6654-6664 (2007).

[17]   J. D. Kamminga, H. d. K. Th, R. Delhez, and E. J. Mittemeijer, Journal of Applied Physics 88, 6332-6345 (2000).

[18]   W. D. Nix and B. M. Clemens, Journal of Materials Research 14, 3467-3473 (1999).

[19]   G. Abadias, Surface and Coatings Technology 202, 2223-2235 (2008).

[20]   F. M. D'Heurle, Metallurgical and Materials Transactions B 1, 725-732 (1970).

[21]   H. Windischmann, Critical Reviews in Solid State and Materials Sciences 17, 547-596 (1992).

[22]   L. Dong and D. J. Srolovitz, Applied Physics Letters 75, 584-586 (1999).

[23]   N. Schell, W. Matz, J. BГ΅Ettiger, J. Chevallier, and P. KringhГ΅j, Journal of Applied Physics 91, 2037-2044 (2002).

24 U. C. Oh, J. H. Je, and J. Y. Lee, Journal of Materials Research 10, 634-639 (1995).

25 J. F. Ziegler, J. P. Biersack, and U. Littmark, *The Stopping and Range of Ions in Solids* (Pergamon, New York, 1985).

26 S. Berg, T. Larsson, C. Nender, and H. O. Blom, Journal of Applied Physics 63, 887-891 (1988).

27 S. Berg and T. Nyberg, Thin Solid Films 476, 215-230 (2005).

28 S. Mahieu, G. Buyle, D. Depla, S. Heirwegh, P. Ghekiere, and R. De Gryse, Nuclear Instruments and Methods in Physics Research Section B: Beam Interactions with Materials and Atoms 243, 313-319 (2006).

29 W. D. Westwood, Journal of Vacuum Science and Technology 15, 1-9 (1978).

30 P. Patsalas, C. Gravalidis, and S. Logothetidis, Journal of Applied Physics 96, 6234-6235 (2004).

31 P. Patsalas, in *Handbook of Nanoscience and Nanotechnology*, edited by S. Logothetidis (Springer, New York, 2010).

CHAPTER 3

THIN FILM

CHARACTERIZATION

3.1 Introduction

In the present chapter we discuss the techniques used to characterize the nitrides during the framework of the present thesis. The chapter is divided in five sections according to the information obtained by the techniques used. Each section starts with an introduction about the general field and afterwards each technique is described in terms of the main principle, the basic configuration and the information obtained.

The first section is about the structural and microstructural characterization of thin films. It includes techniques based on the family of X-ray diffraction in different geometries. X-ray diffraction is a powerful technique for structural analysis and it is widely used in thin film technology. Each geometry probes a different part of the crystallite part of the material and reveals information not only about the fundamental structure parameters (d-spacing, crystal group, lattice constant) but also about the long range order of the solid (grain boundaries, voids, defect concentration).

The next section is the section of the morphological characterization. The morphology of thin films is defined as the long range structure of the material and it is described in terms of grains, grain boundaries, columnar or voided/open structure an others as well. As described in chapter 2 the deposition processes lead to different microstructures-morphologies. All the macroscopic properties of the film are affected from the microstructure of the film. A fibrous or porous structure can enhance surface area while on the other hand the hardness is altered. Since the thin films in nowadays need to show a multitasking character in complex low dimensional systems the control of the microstructure is extremely important. The tools for the determination of the microstructure are plenty. Some techniques rely on indirect measurements of the microstructure aspects like density and others just inspect the surface in a 3D topology or examine the cross section images.

The third section is about the compositional and chemical characterization of thin films. Many properties of the thin films strongly depend on the exact composition as well as the presence of impurities and poisonous elements. The qualitatively and quantitatively determination of the elements in a specimen is the aim of the compositional characterization. The two techniques used for characterization in section II were the Auger Electron Spectroscopy and the Energy Dispersive X-Ray spectroscopy. The first one is a surface sensitive technique which can detect light elements in contrast with the X-ray technique which is a bulk technique and more sensitive for heavier elements like the transition metals.

The section IV is about the electronic and the optical characterization of the nitrides thin films. The scope of the electronic characterization is to define the band structure of the

material as well as the dielectric function. The interactions of the material with the electromagnetic radiation are linked with the electronic structure. The band structure of a material cannot be directly measured but according to observations it can be resembled accordingly from experimental input. This input is the dielectric function which is more than essential for the complete study. The first technique used for optical characterization is the optical reflectance spectroscopy. It is a fast, easy to perform, technique which can reveal information about the dielectric function through the reflectivity and additionally extra information about the thickness of the films or the roughness of the surface and/or interfaces. The second technique is the spectroscopic ellipsometry which can also provide information about the thickness and the roughness of the surface but it provides directly the dielectric function of the material.

The last section of the present chapter is about the stress characterization of thin films. Thin film stresses are very important in almost all areas of technology. The excess amount of stress in deposited thin films can cause reliability issues and maybe device failures. Delamination, bad adhesion, buckling and cracking of thin films are some of the most common mechanisms of failure. Beyond of these issues of reliability, the stress control can be used to tune the properties of thin films. Thus it is very important to reveal the mechanisms affecting the stress of the thin films and consequently manage to adjust it accordingly to the desired level. The first important step is to properly measure the stress in the thin films and this section describes two well known techniques for that reason. The first one is the wafer curvature technique implemented *in-situ* and *real time* during deposition and this technique is able to define the macroscopic stress of the system (substrate-thin film). The second technique is based on X-ray diffraction using the $\sin^2\psi$ method.

Section I: Structural and microstructural characterization

3.2 Introduction

The structural analysis is a very important characterization for a material. The structure of a material is one of the parameters that define the properties and the behavior of the final product. Concerning the small dimensions of the thin films along with the diversity of the deposition techniques which lead to different structures, it is safe to say that the structural characterization is the most important parameter regarding the study of materials.

A solid material such as the thin film material could have 3 major structural characteristics, as described in chapter II. They could be epitaxial, polycrystalline or amorphous. The discrimination between these types is quite easy through the diffraction pattern. But each type of the above has characteristics which are very important. For example in the case of epitaxial films the order of epitaxy is very important parameter as well as the lattice mismatch of the constituents. Similarly for the polycrystalline films there are features which need to be investigated, such as the grain orientation and size among others.

In the present thesis the majority of films are polycrystalline and further on we are going to describe all the aspects of structural characterization around these types of films as well as the techniques used to characterize the films.

3.3 X-ray Diffraction (XRD)

The X-ray diffraction is a versatile, non-destructive technique that reveals detailed information about the chemical composition and crystallographic structure of materials. It is based on the elastic scattering of the X-ray waves by the atoms inside the crystal. In figure 3.1 it is shown the XRD pattern of a NaCl polycrystalline sample showing the peaks that correspond to the interatomic planes with hkl numbers. Each peak corresponds to a constructive interference between waves scattered by atoms of the material.
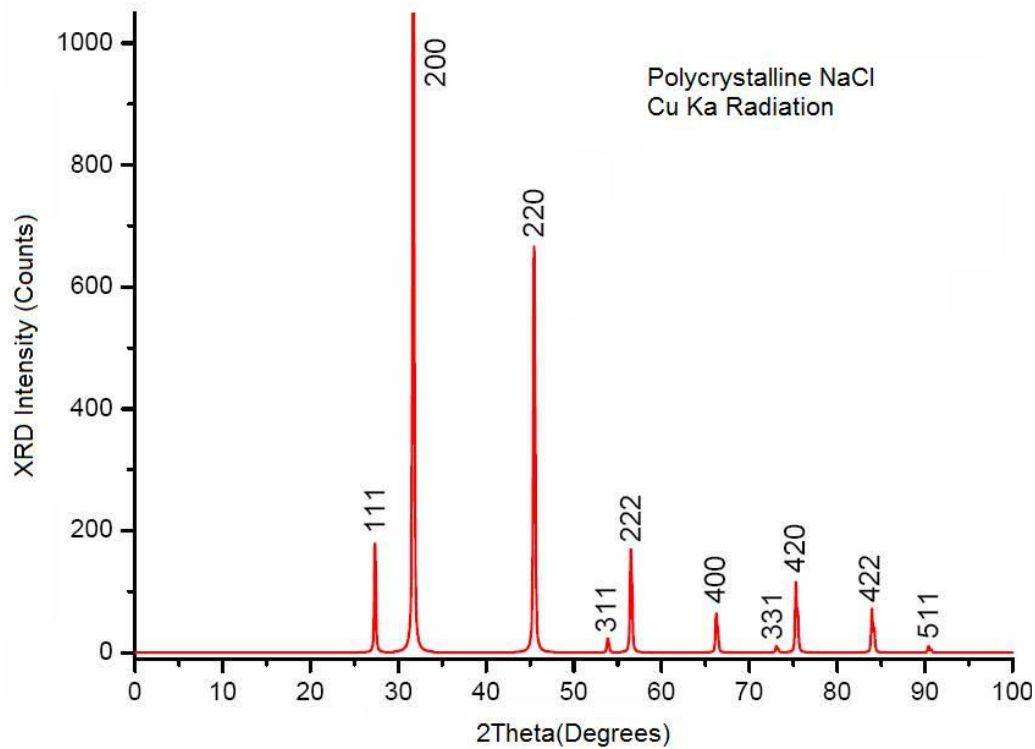
Figure 3.1: X-Ray diffraction pattern of a polycrystalline NaCl using the Cu Kα wavelength.

The constructive interference is occurring when the scattered waves have the same phase. In figure 3.2 it is shown the complete mechanism; the two incident waves are propagating up to points A and C respectively.
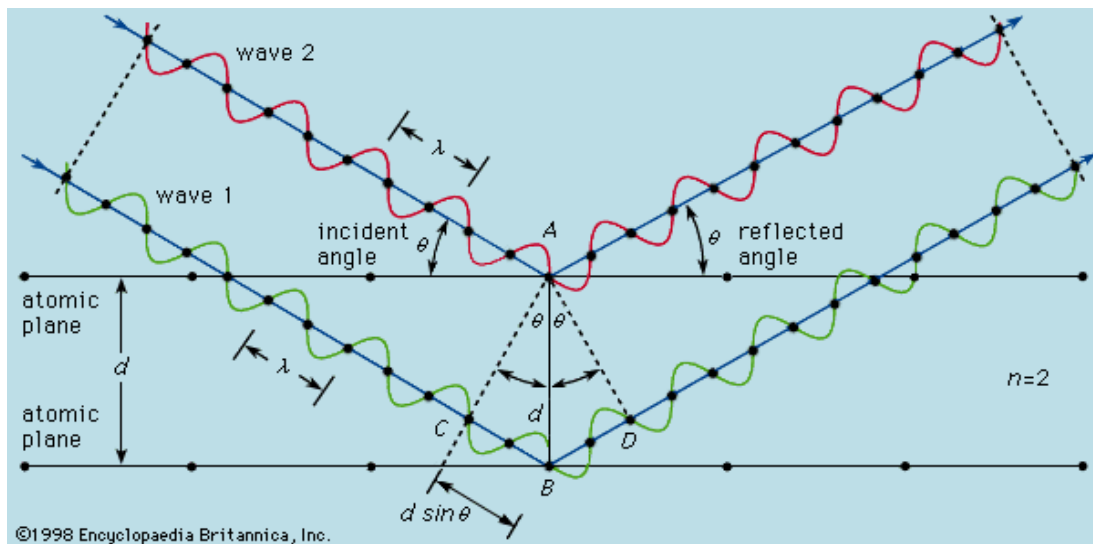
Figure 3.2: Elastic scattering of two incident X-Rays from atoms in a crystal. The constructive interference occurs when the extra route CBD is equal to a multiplayer of the wavelength λ.

After the scattering process they continue propagating from the points A and D. To have the constructing interference the distance CBD should be equal to any integer value of the wavelength of the waves. This is exactly what the Bragg's law is describing.

$$n\lambda = 2d\sin(\theta) \hspace{4cm} (3.1)$$

where n is an integer, λ is the wavelength of the radiation, d is the interatomic distance between diffracting planes and θ is the indent angle of the waves with respect of the sample surface.

For every crystal structure there are many corresponding interatomic distances which can be probed by the XRD and reveal the structure of the material. By determining the *d*-spacings of the hkl planes, the lattice constant can be calculated. For example in a cubic crystal the lattice constant *a* can be calculated by the corresponding spacing *d* of the hkl planes using the expression:

$$a = d\sqrt{h^2 + k^2 + l^2} \hspace{4cm} (3.2)$$

where hkl are the miller indices of the diffracting plane.

The above aspects are the basic features of the XRD technique. There are a lot of variations especially in scanning geometries and in data interpretation. Before presenting the basic geometries of diffraction it is useful to introduce the notion of the scattering vector which is defined as:

$$q = \frac{2\pi}{\lambda}\left(\hat{s} - \hat{s}_0\right) \hspace{4cm} (3.3)$$

Where $\hat{s}_0$ and $\hat{s}$ are unit vectors in the direction of the incident and scattered directions respectively and λ is the X-ray wavelength. The magnitude of q is related to 2θ, the angle between $\hat{s}_0$ and $\hat{s}$ with the expression $q = \frac{4\pi}{\lambda}\sin(\theta)$. The maximum intensity of q is occurring when it is normal to the plane with interplanar distance d and it has length of $2\pi/d$. This is exactly what the Bragg's law description. Generally the q orientation with the sample is kept constant and the scan is performed as a function of the angle 2θ while measuring the intensity of the diffraction (length of q). These are called radial scans while on the other hand there are scans which maintain a constant orientation between the incident and scattered beam, probing the same d spacing as a function of orientation. These scans are called rocking scans.

3.4 Bragg-Brentano geometry

The most common geometry of diffraction is the Bragg-Brentanno which is shown in figure 3.3. In this geometry a radial scan is performed by changing the incident angle θ and the detector angle 2θ at the same time in locked positions. This geometry is probing d-spacings which are parallel to the surface of the sample (diffraction vector is normal to the sample surface).
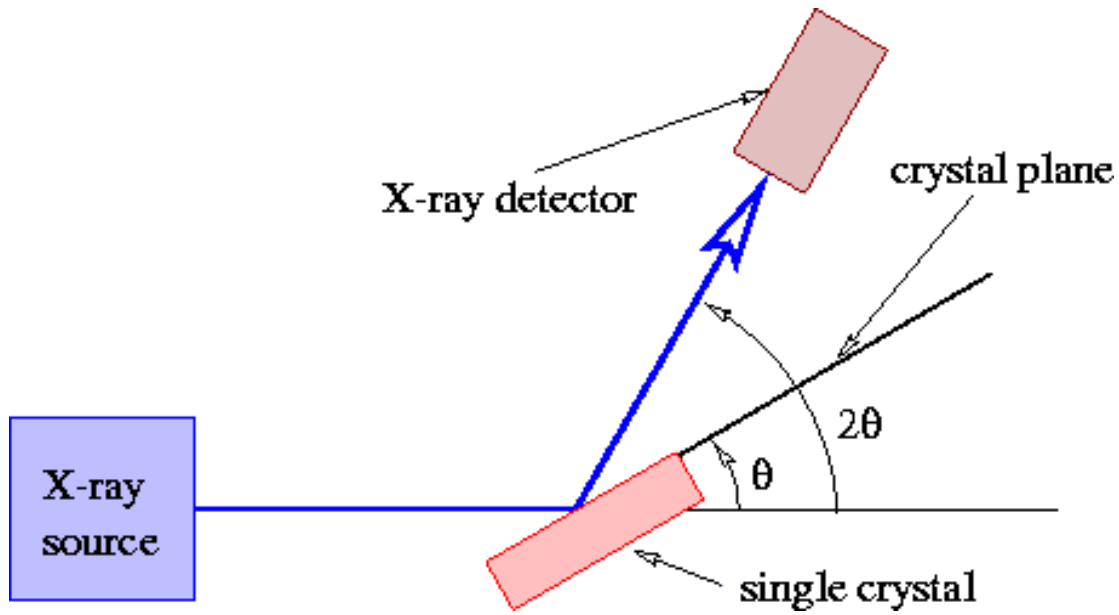
Figure 3.3: The Bragg-Brentano geometry where the incident beam angle (theta) and the diffracted beam (2theta) are coupled together.

It is the most common geometry and it is used to determine the structure of the material. In the case of thin films the deposition parameters and the substrate surface can promote only one preferred orientation of the crystallites or another. For example in figure 3.4 it is shown the diffraction pattern of two thin films of cubic zirconium nitride showing different orientation in direction parallel to the surface as measured by XRD in BB geometry. The relative ratio between one population of crystallites and the sum of all the others is the texture coefficient. For example the texture coefficient of the [111] crystallites in the sample of the image 3.4, is the intensity of the peak [111] to the sum of peak intensities of the [111], [200] and [220] peaks. The equation of any given hkl texture coefficient is:

$$TC_{hkl} = \frac{I_{hkl} / PDF_{hkl}}{\sum\limits_{hkl} I_{hkl} / PDF_{hkl}} \, , \qquad\qquad (3.4)$$

Where I_{hkl} is the integral intensity of the hkl peak and PDF_{hkl} is the nominal intensity from random polycrystalline powder as described in the Powder Diffraction File (PDF).
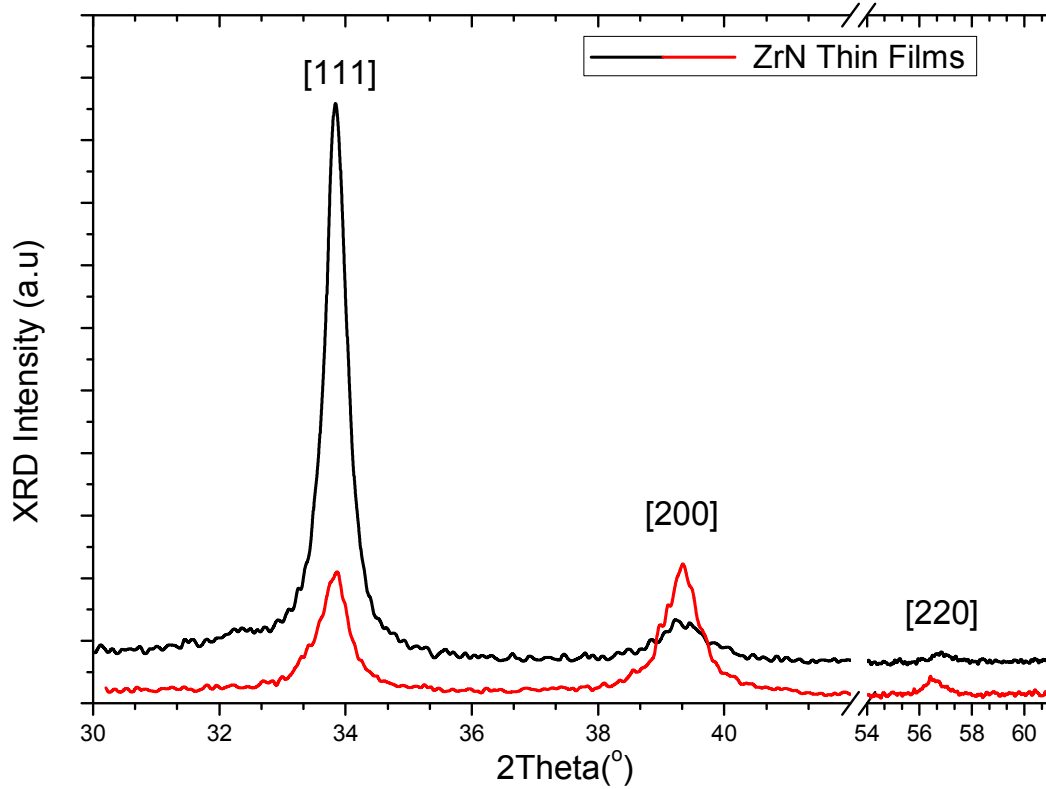
Figure 3.4: XRD pattern of two sputtered ZrN films exhibiting same crystal structure (NaCl) but different out of plane orientation (texture).

3.5 Grazing incidence

Another geometry which belongs to radial scans is the grazing incident geometry, where the incident angle is kept constant (in small values 1°-2° to ensure high diffraction volume) while the detector angle is performing the scan. This technique is ideal for low diffraction volume samples such as thin films. The low incident angle is ensuring the maximum diffraction volume and the detector scan is probing the planes inside the irradiated volume of material. The probed planes during this scan are not parallel with the surface of the sample like the Bragg-Brentano geometry. This technique cannot be used for epitaxial films as well as for highly textured films.

3.6 Texture analysis – Pole figures

In general pole figures are graphical representations of the orientation of object in space. Specifically, texture pole figures are representations of the orientation of crystalline

planes in a material. The crystallographic directions are stereographically projected onto a plane. This is the basic function of the pole figures and this is why they are used for texture analysis and representation.

First of all the scope of the texture analysis is to define the orientation distribution of crystallites in the sample as a function of direction. For example to observe the population of [111] grains the incident and scattered angle are fixed to probe the d-spacing of [111] planes and a rocking scan is performed changing the φ and ψ angles. These angles are shown in figure 3.5.
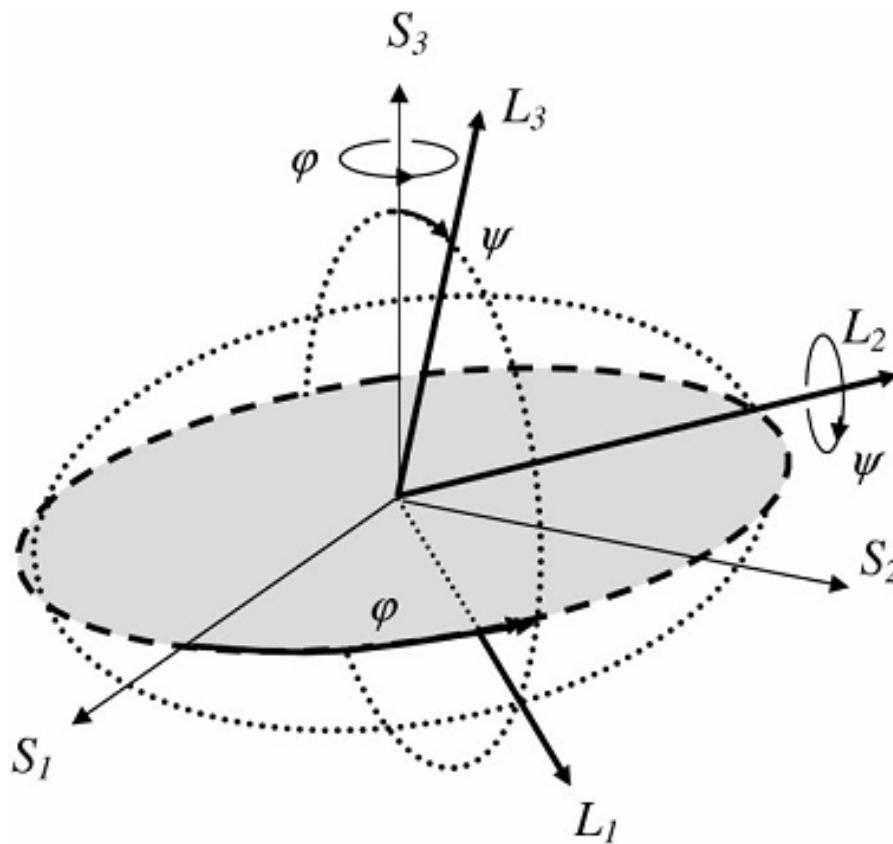
Figure 3.5: A simple drawing which shows the Euler angles φ and ψ and the correlation between the laboratory and the sample coordintate system (figure from[1]).

The measured intensity for each set of ψ and φ is linked with the population of [111] diffracting planes in that direction. The angles ψ and φ where the diffracting intensity is observed are the Euler angles of the [111] planes.

3.7 Grain size – Micro strain

The X-ray diffraction techniques can provide a lot of information about the structure of the matter and among other could provide information about the grain size distribution of the

crystallites. The grain size is a very important feature for the properties and the functionality of the thin films. The grain size depends heavily on the deposition conditions and it is very useful to control it. There are many methods which can extract information from diffraction patterns about the grain sizes. The Scherrer formula and the Williamson-hall are two among others. All these technique rely on the shape of the diffraction peaks to extract data.

A perfect infinite crystal has a very sharp diffraction peak (figure 3.6). This is why the distribution of d spacings is very narrow and the width of the peak is due to the instrumental contribution.
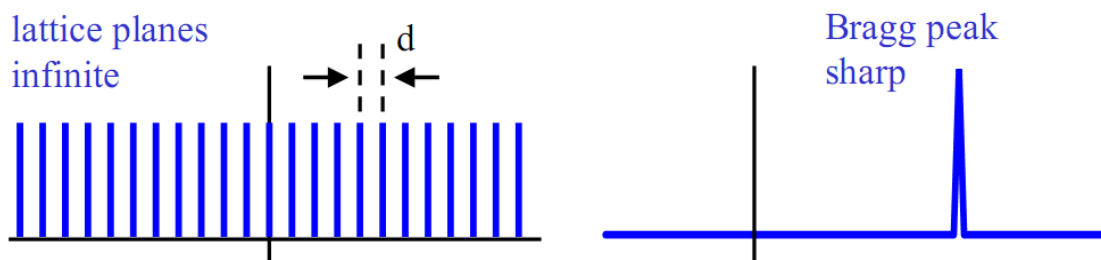
Figure 3.6: An infinite array of lattice planes produces a single very sharp diffraction line (figure from[2]).

A perfect crystal with a finite size has a wider Bragg peak (figure 3.7) because the coherency length is also finite. The coherency length is the population of the crystallites diffracting the same way. This is related to the statistical sampling and a high coherency length means a large statistical sample minimizing the variation.
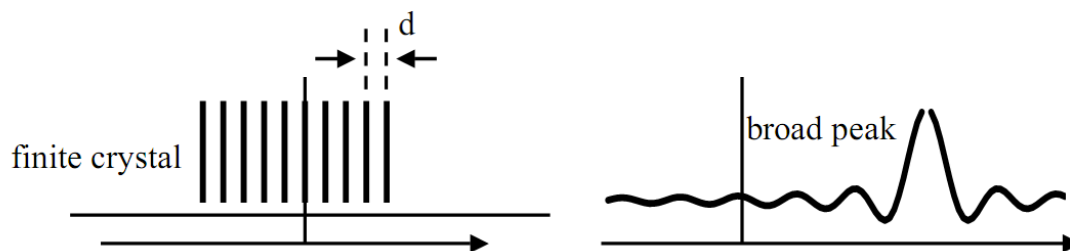
Figure 3.7: A finite array of lattice planes produces a single sharp diffraction line (figure from[2]).

As mentioned before the instrumental broadening is included in a line shape. In general a diffraction peak is a convolution of the instrumental broadening as well as the structural imperfections. A parameter which is used to describe the shape of a diffraction peak is the integral breadth β, which is the ratio between the area and the height of the peak.

Another mechanism that has an effect on the peak shape is the micro strain of the crystallites. The micro strain is due to the local variations of the interatomic distances of atoms which belong to the diffraction domains. These variations could be due to voids or

defects or to grain boundaries where dislocations have a higher density than in the interior of the grain. The total diffraction peak is a superposition of the local diffracting peaks from the material. This is shown exactly in figure 3.8.
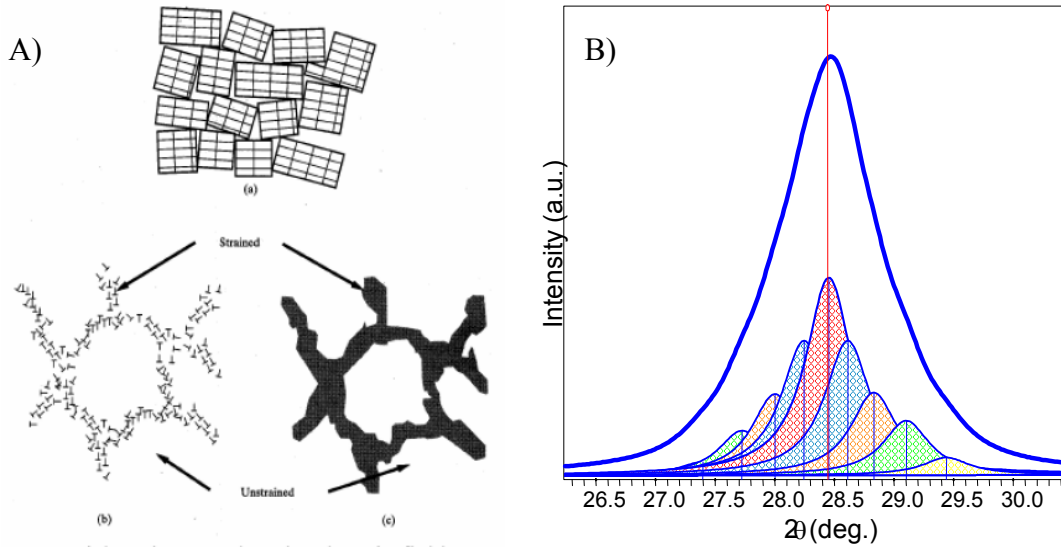
Figure 3.8: A) Dislocations near grain boundaries produce strain fields. B) The superposition of all the diffracting planes (strained or not) is the final diffraction peak.

Until now we have seen that there are two parameters affecting the width of the diffracting peaks. The first one is the finite size of the crystallites which implies a reduced coherency length and the second is the micro-strain. One analysis method is the Williamson-Hall. For this method the diffraction peaks of various hkl planes are measured and the integral breadths are plotted as a function of the angle θ or the scattering vector. The equation for the Williamson-Hall is:

$$\beta = \frac{1}{D} + 2\varepsilon_s Q \qquad (3.5)$$

Where D is the size of the crystallites and the ε_s is the microstrain. The slope of the line is linked with the microstrain and the intersection with the y axis is the size of the crystallites. In figure 3.9 it is shown an example for the implementation of the Williamson-Hall in ball milled Mo. This method works very well and gives accurate results. Additionally in the case where micro strain is zero the integral breadth is constant and this is exactly what the well known Scherrer formula is describing.

In the case of thin films and especially for highly textured there are no hkl reflection available or their intensity is very small. In this case the WH method cannot be implemented. The ideal method for this case is the single line analysis[4,5].
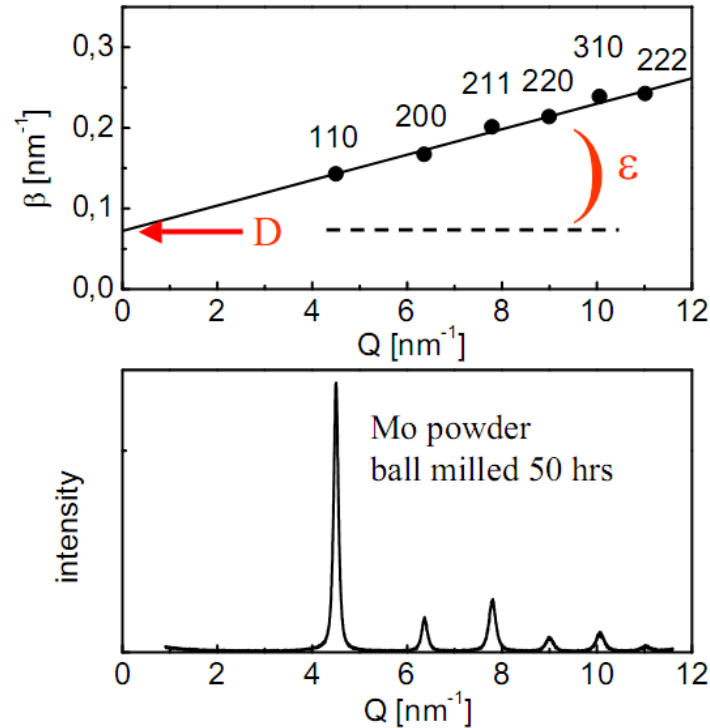
Figure 3.9: Williamson Hall method for ball milled Mo. The intersection with the vertical axis represents the grain size and the slope the microstrain[3].

The main idea behind that method is that the measured line profile is the convolution of the standard profile and the structurally broadened profile. The Cauchy (βc) integral breath is correlated with the grain size and the Gaussian (βg) with the microstrain. Thus by determining the Cauchy (βc) and the Gaussian (βg) integral breadth of a given Bragg reflection profile fitted by a voigt function it is possible to calculate the grain size and the microstrain. The complete analysis with the equations is shown in appendix.

Section II: Morphological characterization

3.8 Introduction

The microstructure of the thin films is a major characteristic which is affecting almost all the properties of the thin film. On the other hand the microstructure of the film is strongly dependent on the deposition parameters. Thus the control of microstructure, as we will see in the results section of the present thesis, is essential for the development of specific type of functional materials for specific applications. The term microstructure includes features like the grain size and morphology, the preferred crystallographic orientation of the grains, the interfaces between the independent layers and the surface, the defects concentration, the homogeneity of the materials and others. All the above characteristics can be evaluated in a direct or in an indirect way.

The techniques used for microstructural characterization of the samples in the framework of the present thesis are the X-ray reflectivity, the atomic force microscopy and the scanning electron microscopy. At the description of each technique, the basic configuration will be presented as well as all the possible information that could be obtained by the specific technique.

3.9 X-ray reflectivity

The basic idea behind the technique is to reflect a beam of X-rays from a flat surface and then measure the intensity of X-rays reflected in the specular direction (reflected angle equal to incident angle). The intensity of the reflected beam as a function of the incident angle can reveal information about the microstructure of the material such as density and roughness. The refractive index of the material in the range of X-rays is smaller than unity. This means that there is an angle where the beam does not penetrate inside the material, it is totally reflected and this angle is called critical angle. The value of the critical angle is correlated with the density of the material. For incoming angles higher than the critical angle a part of the beam is penetrating the material and another part is reflected. If there are many interfaces inside the material the reflected beams can interfere constructively or not and fringes can come out on the recorded pattern. This effect is very important for the characterization of thin films and multilayers because it can probe the thickness of each layer (the distance between the interfaces).
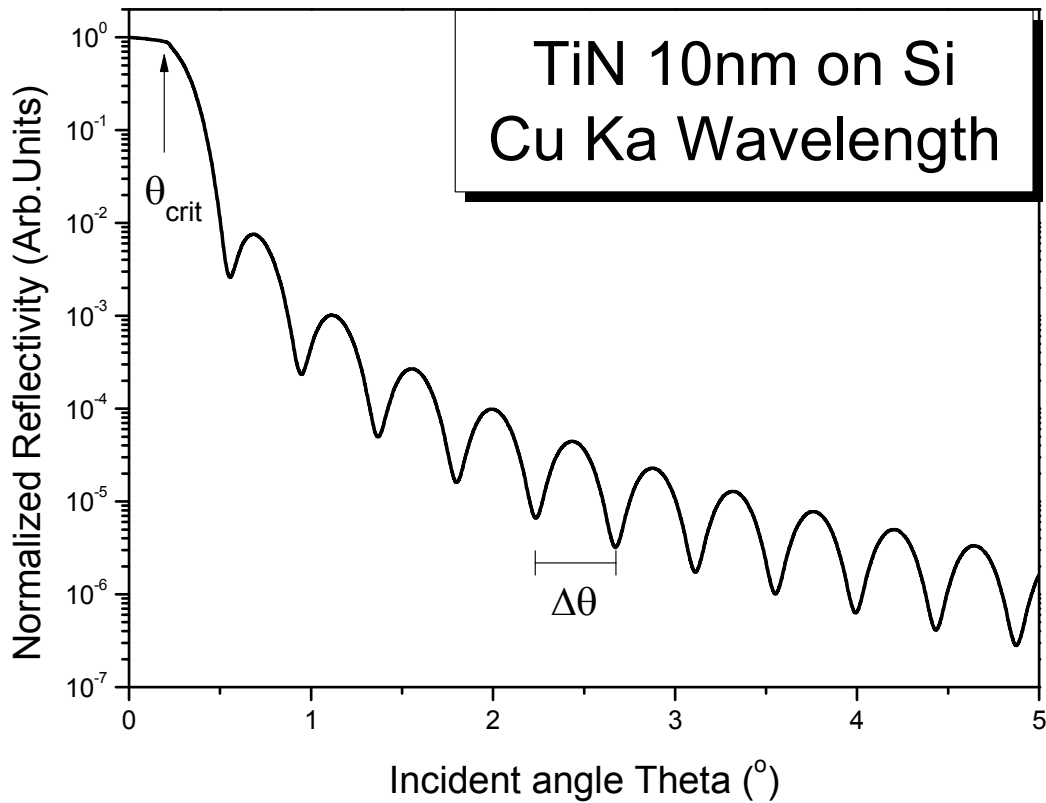
Figure 3.10: Simulated reflectivity curve of a TiN layer (thickness 10nm) on Si using Cu Ka wavelength based on ref[6] .

Additionally the roughness of each interface is having effect on the reflectivity pattern providing information from all the interfaces inside the material. In figure 3.10 it is shown a calculated reflectivity pattern of a thin film on a substrate. It is marked the critical angle and the period of the fringes. The reflected pattern is analyzed using the Parrat's formalism[7] with the appropriate model providing all the information about the films.

Summarizing, the XRR is a non destructive, versatile technique which can provide information about the density, thickness, surface and interface roughness. All these data are essential in the characterization of thin films.

3.10 Atomic force microscopy

The atomic force microscopy is a high resolution surface probing technique which belongs to the family of scanning probing techniques. This technique is based on the interaction between a tiny and very sharp tip and the surface of a sample. The tip of the cantilever is coming to the proximity of the surface and is subjected to forces. The forces cause a deflection of the cantilever which is detected from a laser beam. The basic configuration of an AFM it is shown in figure 3.11.
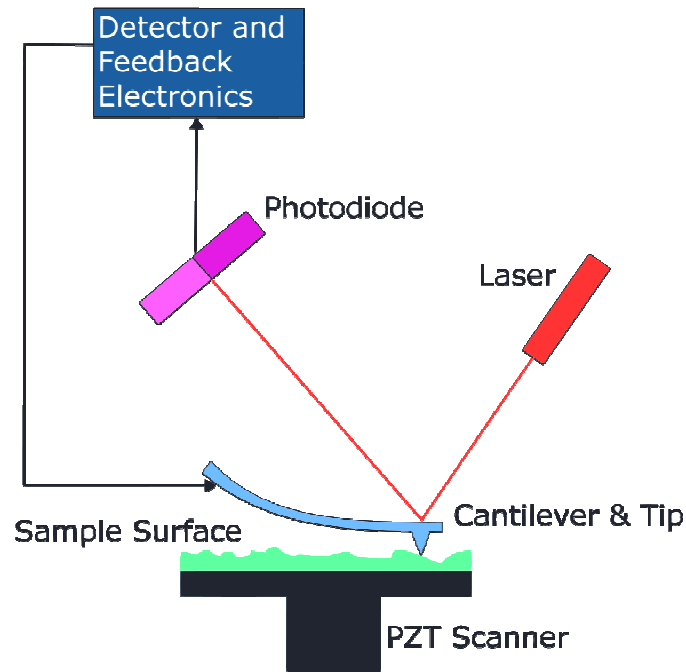
Figure 3.11: A simple diagram showing a basic atomic force microscopy setup[8].

The two major modes of operation is the tapping mode where the cantilever is oscillating near its resonance frequency and comes very close to the surface of the sample. The other mode of operation is the non-contact mode, where the cantilever is oscillating in a frequency higher that the resonance frequency far away from the surface sample
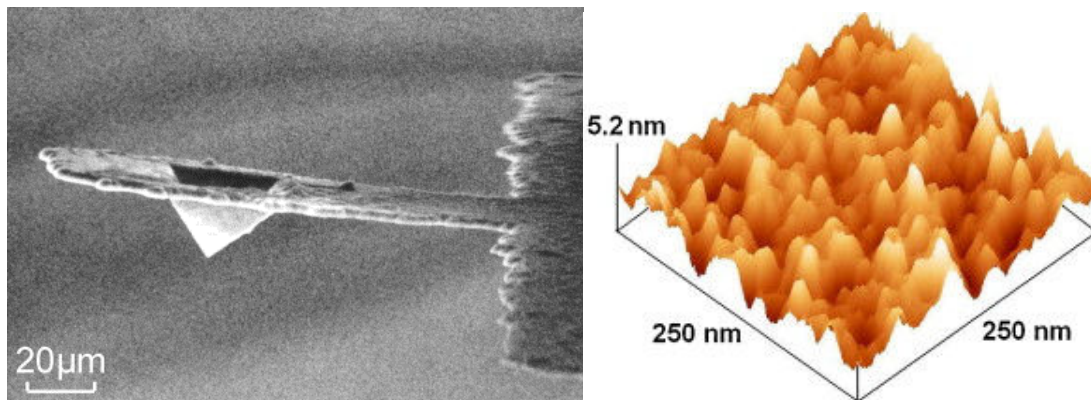
Figure 3.12: a) A cantilever tip with diamond fabrication as seen from a SEM[9]. b) A 3D AFM graph showing the topography of SnO$_2$ surface[10].

3.11 Scanning electron microscopy

The scanning electron microscopy is a technique which is based on an electron beam to scan a surface. The electron beam is irradiating the surface atoms which are emitting secondary electron. The secondary electrons carry information about the topography of the surface. In figure 3.13 it is shown the basic configuration of a SEM instrument. Except of the

imaging capabilities based on the secondary electron emission there is another way to explore the topography of a surface. This is the backscattered electron from the main electron beam. Using a backscatter electron detector it is possible to obtain a highly contrasted image based on elements on the surface since high Z elements produce more backscattered electrons. This feature can reveal different compounds and phases present on the surface of the sample.

Another feature of the technique is the compositional analysis of the samples. The high energy electron beam can produce an inner core excitation of the atoms of the surface. After that the atoms decay emitting characteristic X-ray photons. The process will be described in the EDX section.
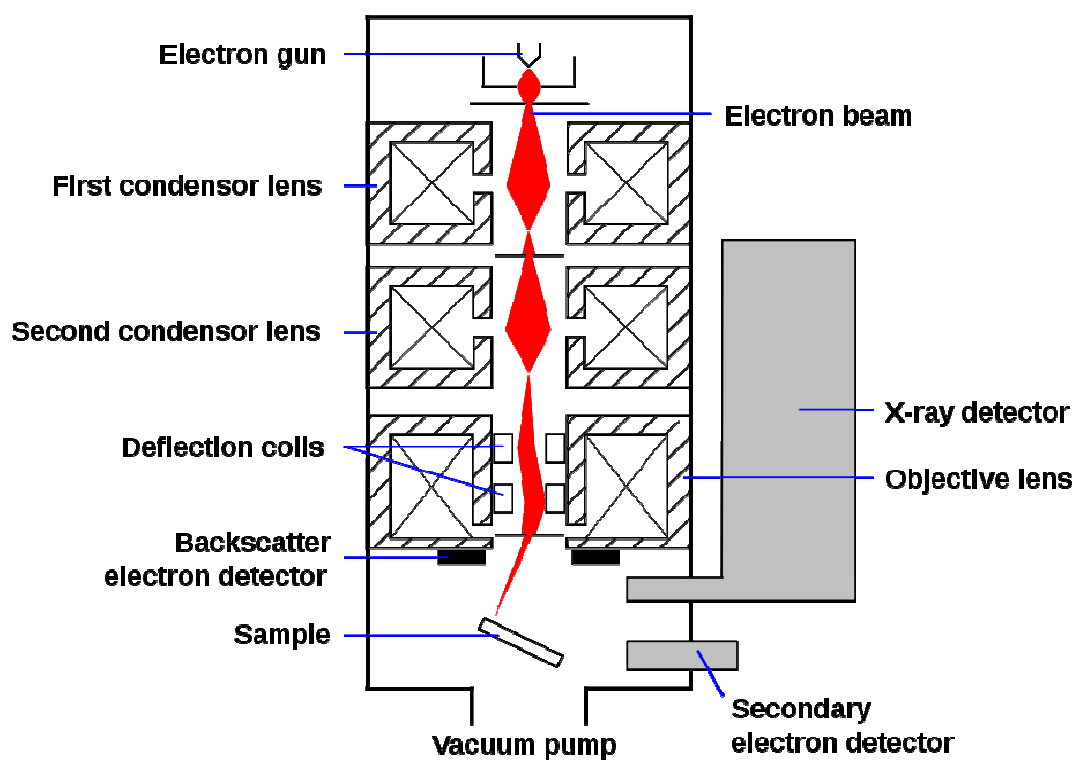
Figure 3.13: A simple sketch showing the basic design of a scanning electron microscope[8].

Section III: Compositional and chemical characterization

3.12 Introduction

The compositional analysis is a basic analysis on the thin films technology. Many of the properties of the thin films are depending on the exact stoichiometry of the sample. Additionally during the deposition of the films other elements can be present affecting deleteriously the final film. Thus the compositional analysis is required to ensure that the final film has the right concentration and it is free from contaminants.

Another feature of the compositional analysis is the phase analysis. The phase analysis ensures that the present elements have formed the right compounds. This can be done by the structure analysis and particularly the XRD technique but also can be complemented by a chemical analysis such as the Auger electron spectroscopy.

3.13 Auger electron spectroscopy

The Auger electron spectroscopy is a surface sensitive technique for chemical analysis. The main principle of the technique is the auger electron emission which is shown in figure 3.14. A transition of an electron in an atom (2s→1s), filling in an inner-shell vacancy (1s) causes the emission of another electron from another shell (2p). The ejected electron is the Auger electron and its kinetic energy is dependant on the electronic structure of the material (E_{2s}-E_{1s}). Thus the auger electron and the corresponding kinetic energy is a "fingerprint" of an element inside the material.

The initial vacancy in the inner shell can be caused by electron radiation, by X-rays or another cause and it has no effect on the auger effect. The Auger emission is a process from three atomic-shells; the first one being the shell with the initial vacancy, the second shell is the origin of the electron that fills the vacancy and the third shell is the origin of the ejected auger electron. Consequently a corresponding auger transition is named by the names of these shells participating in the process i.e KLL. In some cases, when a shell, which is participating to the Auger process, is participating to the valence band, as well, the indication V is used for the corresponding Auger peak (e.g. KVV instead of KLL).

The Auger electrons have a kinetic energy ranging from 10eV to a few keV. The escape depth of electrons with that kinetic energy is about a few nanometers of matter making the technique a surface sensitive technique. Another feature of the auger spectroscopy is the

high sensitivity in the detection on light elements, except in He and H which cannot be detected at all.
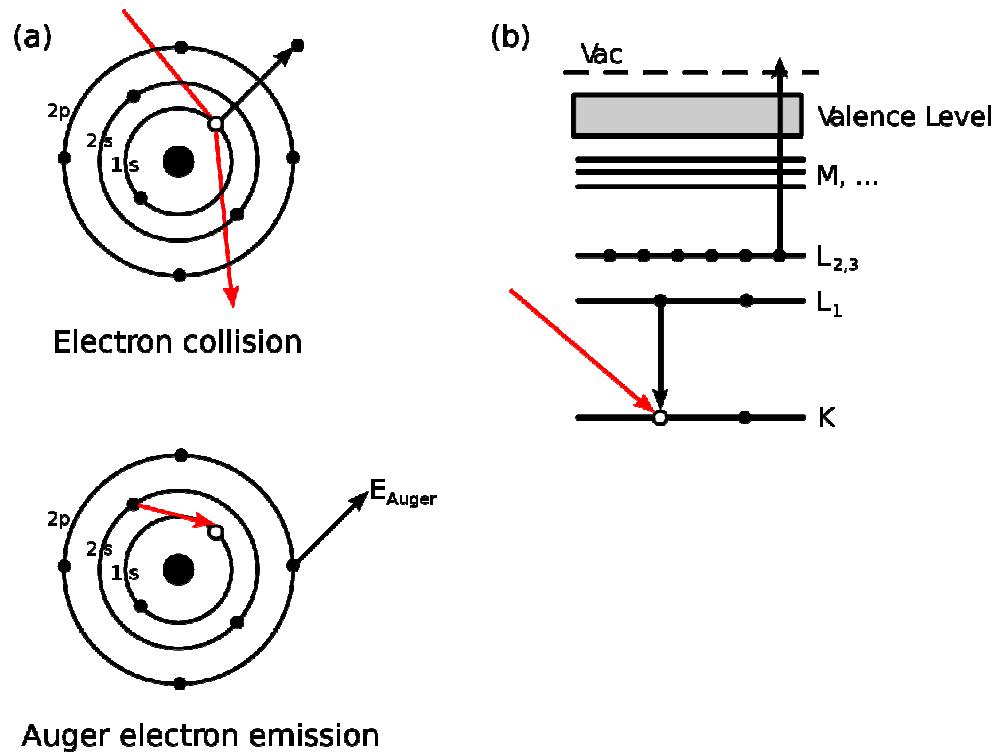
Figure 3.14: a) schematic showing the Auger electron emission process in terms of atomic orbitals and b) the same Auger process using spectroscopic notation[8].

Any excited atom with vacancies in inner shell can be decayed by two processes; the auger electron emission and the X-ray fluorescence. In figure 3.15 it is shown the auger emission yield and the X-ray emission yield for vacancies in K shell. It is obvious that low Z elements are decaying with an auger electron emission rather than X-ray emission. The same trend applies for vacancies in L and M shells. Particularly, this spectroscopic technique is used in our case for the detection and the analysis of the nitrogen content and the stoichiometry in the nitrides thin films.
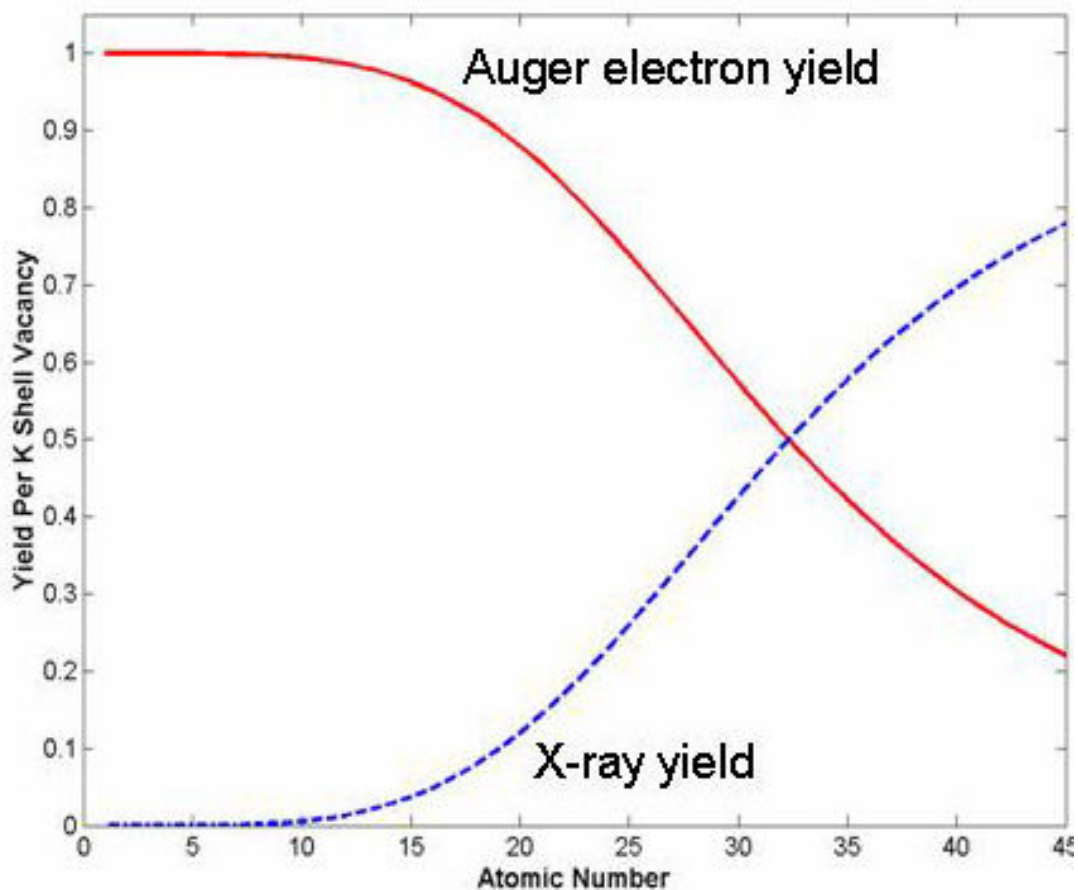
Figure 3.15: Emission yields for Auger and X-rays for K shell excitation.

3.14 Energy dispersive x-rays spectroscopy

The energy dispersive X-rays spectroscopy is a non destructive, easy to perform technique for elemental analysis. It is based on the emission of characteristic X-rays from a material that has been excited. The excitation source could be another X-ray source, or gamma rays or electron beam. The aim is to ionize an inner-shell of an atom which will decay by emission of an X-ray photon. The energy of the photon is characteristic of the electronic structure of the emitting atom. Consequently each atom emits a photon with specific energy. The energy of the X-rays photons is ranging from a few keV to several decades of keV. The escape depth of the photons with such energies is in the range of micrometers making the technique ideal for bulk analysis.
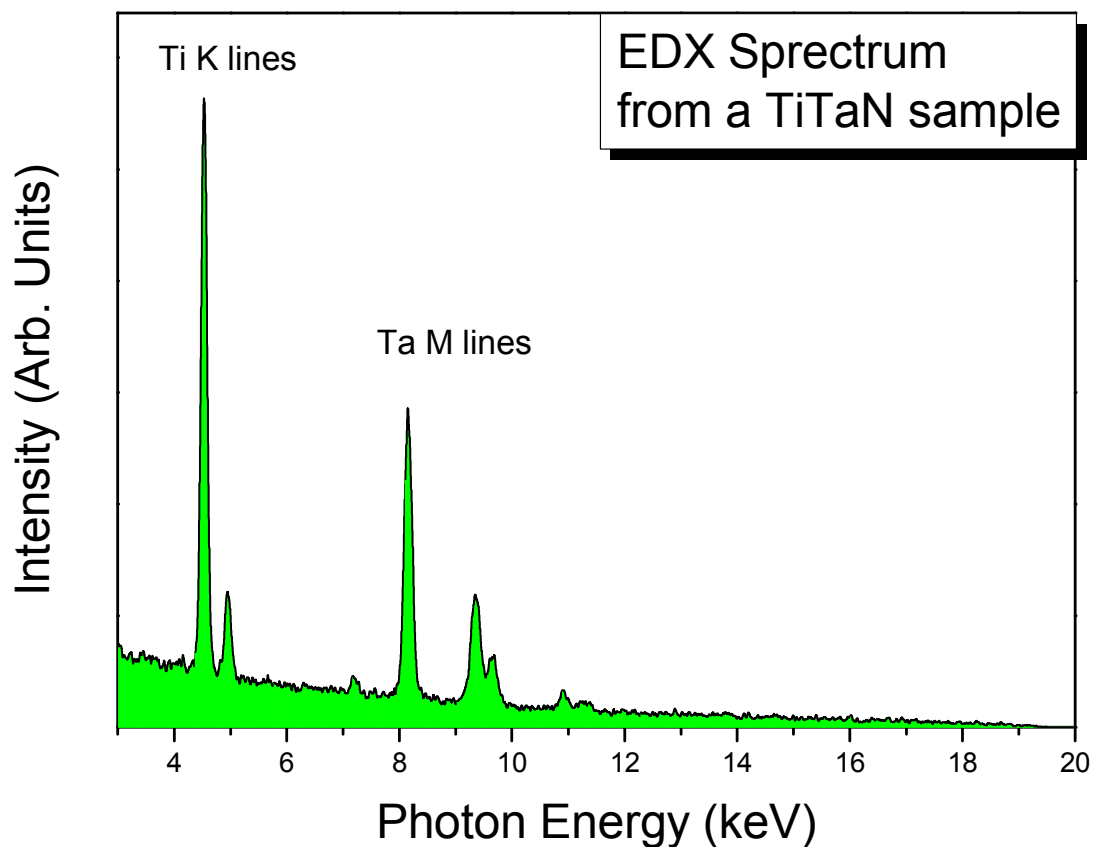
Figure 3.16: A typical X-ray energy dispersive spectrum from a TiTaN sample. The spectrum acquired using an electron beam of 20kV from a scanning electron microscope. The spectrum shows the characteristic K and M lines of Ti and Ta respectively.

In figure 3.16 it is shown a typical spectrum of a TiTaN sample measured by EDX in the chamber of a scanning electron microscope. The excitation source was a 20kV electron beam and the detector was a liquid nitrogen cooled Si(Li).

Section IV: Electronic and optical characterization

3.15 Introduction

This section is about the electronic structure of the thin films and the corresponding optical properties. The electronic structure of a material is responsible and plays a considerable role on the properties. The way the electrons of the atoms bond each other and form the solid defines the behavior of the material. The high energy spectroscopic techniques as described in the previous section, are probing the core electrons to detect elements. The following techniques are probing the outer electrons of the atoms, the low energy electrons which are locating inside the bands of the solid. These electrons are responsible for the optical and electrical properties of the material. The color, the resistivity, the energy gap, the absorption and the transmission are properties that are dominating by the electronic structure of the solid.

The dielectric function of the solid is describing the interaction of the solid with the electromagnetic radiation and is a function of wavelength. Particularly in the nitrides the dielectric constant can be assembled from the superposition of a Drude term and two Lorentz oscillators, also known as the D2L model. The Drude term describes the "free" electrons in bands and the Lorentz oscillators describe the bounded electron in the solid. Each model is characterized by some parameters, which are correlated with the properties of the material.

The Drude term is mainly characterized by the unscreened plasma energy E_{pu}, and the dumping factor Γ_D. The unscreened plasma energy depends on the concentration of the conduction electrons. The Drude dumping factor is due to the scattering of electrons and is the inverse of the conduction electron relaxation time. The determination of these parameters can reveal information about the conductivity and the microstructure of the material.

The lorentz oscillators are described by their energy positions, the oscillator strength and broadening factor. The energy positions of the oscillators are the resonance frequencies of the bonded electrons for each type of bounded electrons (p or d sheel). Additionally there is another term in the D2L model the ε_∞ which is a background constant, larger than unity due to the contributions of higher energy transitions not included in the present model (e.g X-rays transitions).

All the above parameters can reveal information about the optical properties of the film as well as the microstructure, the stoichiometry, the defect concentration and resistivity

among others. This is why the optical and electronic characterization is very important for a complete analysis of the thin film materials.

The two techniques used to characterize the optical properties of the materials were the spectroscopic ellipsometry (SE) and the optical reflectance spectroscopy (ORS).

3.16 Optical reflectance spectroscopy

The optical reflectance spectroscopy is a non destructive technique which is based on the interaction between radiation and matter as a function of wavelength (λ) or photon energy. Specifically the studied parameter is the reflectance of a material as a function of wavelength since there are other alternatives such as the study of transmission or the emission of light.

The figure 3.17 is showing the basic configuration of the ORS technique.
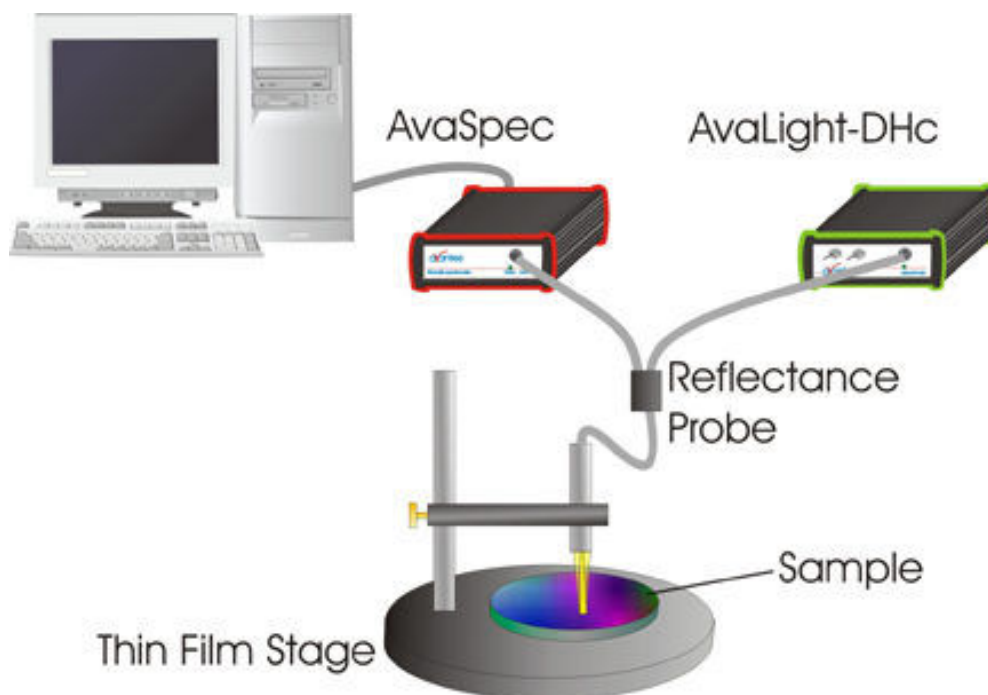
Figure 3.17: The basic experimental setup of the optical reflectance spectroscopy.

A set of optical fibers transfer the light from a source lamp to the sample surface as normal incidence and a fiber is transferring the reflected light to the spectrometer. The reflected intensity depends on reflection on the surface and interfaces if the sample absorption is quite low and the sample is very thin. In case of the nitrides the absorption is high and the film is considered as a bulk from thicknesses around 10nm and higher.

In order to have a wide range of wavelengths, two lamps have been used; a halogen and a deuterium which combined cover a photon range from 1.5eV to 5.25eV (figure 3.18).

78
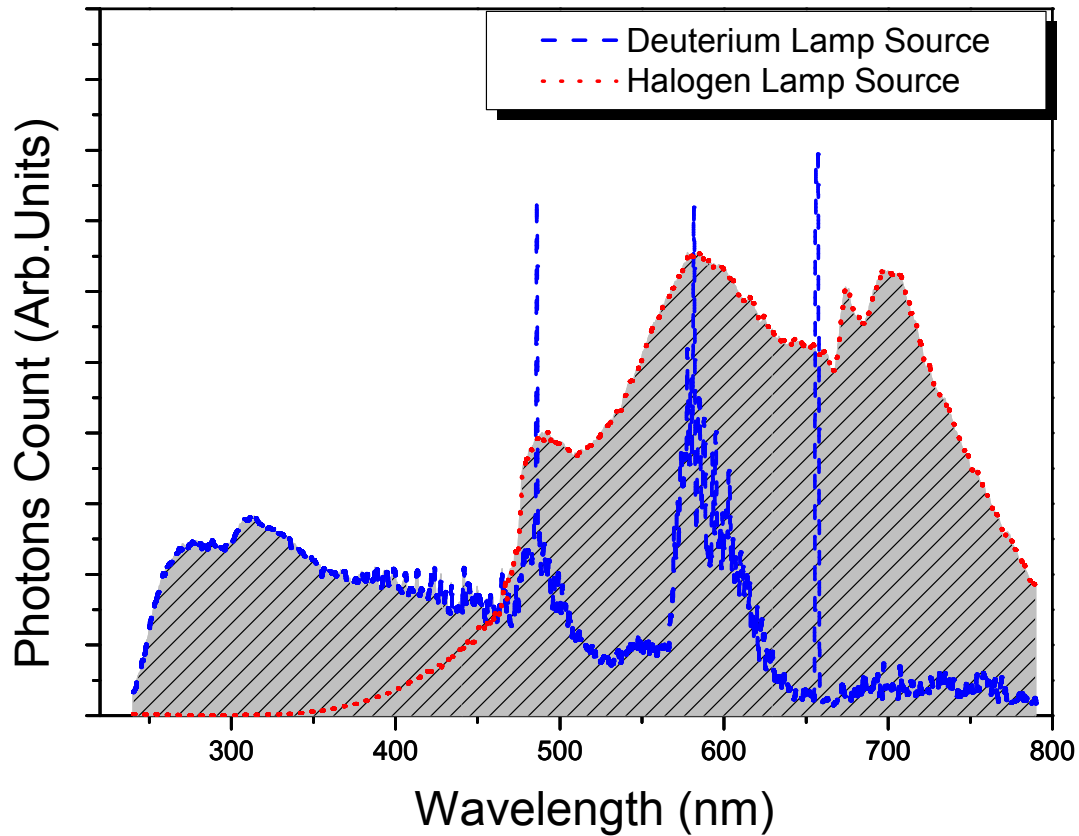
Figure 3.18: The spectra of the halogen (red line) and deuterium lamp (blue line) used for the reflectance measurements. The filled gray area is the total spectrum used for measurements.

The reflectivity of the film is a function of the refractive index n and the extinction coefficient k. The dielectric function of the material is also a function of the n and k, thus it is possible to obtain the optical properties from reflectivity measurements.

3.17 Spectroscopic ellipsometry

Ellipsometry is a powerfull optical technique for investigation of the dielectric properties of a material. It is based on the measurement of the polarization change of the electromagnetic radiation upon reflection onto a sample surface. It measures the ratio of intensities of the *p* and *s* polarized light, reflected from the surface and their phase difference. For the phase change measurement usually a rotating optical element (i.e. polarizer or analyzer) is employed; in our case we used a rotating polarizer ellipsometer. The change of the polarization status is linked with the properties of the material, such as the thickness and the dielectric function. Consequently by measuring the changes in the polarization status and applying the corresponding model it is possible to determine the value of the optical

parameters of the material. The basic configuration of the rotating polarizer spectroscopic ellipsometry is shown in figure 3.19.
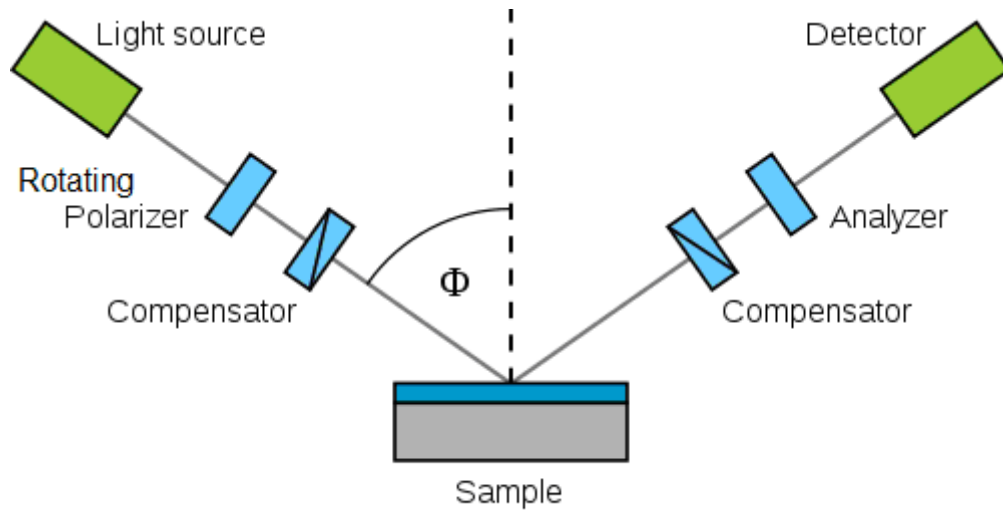
Figure 3.19: The basic experimental setup of the rotating-polarizer spectroscopic ellipsometry[8].

The light source is usually a polychromatic lamp, which is providing the initial beam. Afterwards the beam is polarized and reflected on the sample in an angle Φ. The analyzer is detecting the difference between the incident beam and the reflected beam, for all photon energies. Since ellipsometry is measuring the ratio (or difference) of two values (rather than the absolute value of either), it is very robust, accurate, and reproducible. For instance, it is relatively insensitive to scatter and fluctuations, and requires no standard sample or reference beam in contrast with the optical reflectivity. Additionally by the ellipsometric measurements we obtain directly the real and the imaginary part of the dielectric function in contrast with the reflectivity where we obtain the dielectric function in an indirect way.

Section V: Stress characterization

3.18 Introduction

Stress plays a major role in the properties and behavior of thin films. As an example, stress can result in cracking of a film in the case of tensile stress, or buckling in the case of compressive. Except the failures from excessive stresses, thin film's properties can be tailored by the stress, for example the band gap in epitaxial deposited semiconductors. For these reasons the stress characterization is very important for an unobstructed functional life cycle of the thin films.

The two main techniques used for stress characterization are the substrate curvature and the X-ray diffraction. The substrate curvature technique measures the overall macroscopic inside the film by measuring the change in curvature of a film substrate. It is a very robust technique, non destructive and can be implemented *in-situ* and *real time*. But this technique cannot probe stress to independent crystallites of the material. The X-ray diffraction technique is also a non destructive technique which probes the stress of the crystalline part of the film. The contribution from non diffracting areas such as grain boundaries or voids cannot be estimated.

3.19 Substrate curvature

The idea of measuring the stress state of the film by the curvature of the substrate is very simple. The stress of the film results in applied forces to the substrate. These forces create a bending moment that curves the substrate, changing its shape. By measuring the change in curvature, which is a macroscopic value, we can evaluate the stress state of the deposited film.

Initially the evolution of stress and strain in thin films during deposition and annealing is typically studied by sequentially iterating the process parameters and applying ex situ analysis, the so-called "cook and look" approach[11]. This approach is straightforward and labor-intensive. Recently experiments in which the dynamic stress/strain evolution is measured in real-time during growth are becoming more common. *Real time* measurements are more efficient and they can provide unique information on stress evolution that would be unobtainable though cook-and-look. In figure 3.20 it is shown the basic configuration of a multi beam optical stress sensor.
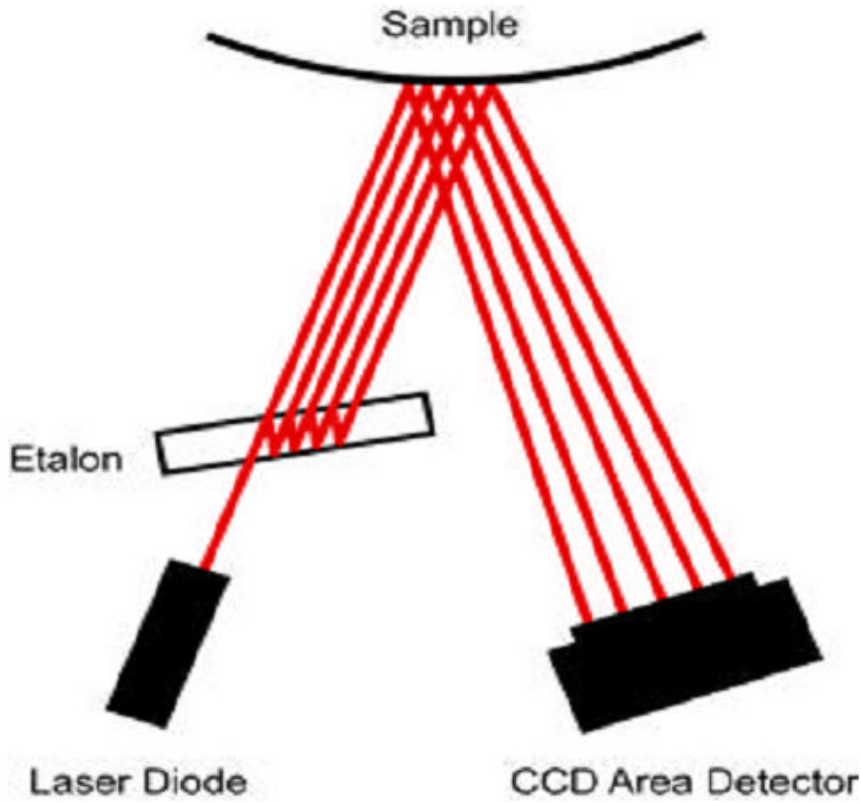
Figure 3.20: The multi beam optical stress sensor [KSA-kMOS].

The change in curvature results in a change of the distance between the laser spots. The difference in curvature, before and after deposition is linked with the stress state of the film. Lately the use of a 2D array of spots is used for the determination of a non uniform curvature of the substrate, as well as for extra functionality reasons (vibrate noise etc).

The mean (biaxial) stress σ_f of the thin film is related with the curvature of the substrate as

$$\kappa = \frac{1}{R} = \frac{6\sigma_f h_f}{M_s h_s^2}$$

(3.5)

Where R is the radius of the curvature, h_S is the thickness of the substrate and M_f is the biaxial substrate modulus of the substrate. The above equation is the Stoney equation[12].

The Stoney equation is strictly true when the substrate is flat prior to film deposition. It is the change in curvature that is required in order to obtain the film stress accurately. Therefore, for post-deposition determination of film stress, the absolute curvature both before and after deposition must be measured. However, in real-time measurement, the change in curvature is obtained by definition and the absolute value is not needed. The curvature is

inversely proportional to the square of the substrate thickness. Thus, for maximum sensitivity very thin wafers should be used. But the Stoney equation works well only when the ratio of thickness between the film and the substrate is lower than 10%.. As the film becomes an appreciable fraction of the substrate thickness, the induced biaxial compression or extension of the substrate, in response to the forces imposed by the film can relieve a measurable portion of the film stress. For a ratio of $h_f / h_s < 10^{-3}$ and typical modulus ratios, Stoney's equation is accurate to within 5%.

Curvature based stress measurements require independent knowledge of film thickness. During deposition, both thickness and stress will be evolving in general. The output of the *real time* measurements is the stress-thickness product, expressed in units of GPa-Å. The incremental stress is the first derivative of the stress-thickness product plotted vs thickness. Another term used very often is the mean stress which is obtained by dividing the stress-thickness by the film thickness.

Summarizing the multi beam optical stress sensor for wafer curvature measurements is a quick, robust and very adaptive technique for *in situ* and *real time* measurements of stress evolution of thin films.

3.20 Stress analysis of thin films by X-ray diffraction (XRD)

Among a number of methods available for stress analysis, such as wafer curvature which mentioned above and others, X-ray diffraction methods are very suitable for the analysis of thin films. X-ray diffraction is a great technique that can be implemented as a microscopic strain gauge in crystalline materials. Moreover, useful additional information can be obtained as a by-product of X-ray diffraction stress measurements: whereas the stress analysis uses the shifts of diffraction lines, the integral intensities of diffraction lines contain information on the crystallographic texture, and the shapes and the breadths of diffraction lines contain information of the size of the diffracting domains (grain sizes) and the content of crystalline defects such as dislocations and stacking faults.

The basic idea on the concept of diffraction stress analysis is shown in figure 3.21 where it is assumed that a polycrystalline specimen is subjected to a compressive stress parallel to the surface. Assuming a biaxial compressive stress parallel to the surface the d-spacing of the crystallites will change as a function of the angle ψ (figure 3.21).
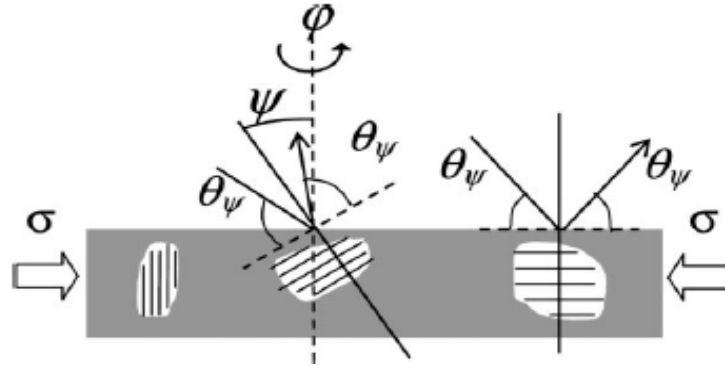
Figure 3.21: A biaxial compressive stress σ implies d-spacing variations as a function of angle ψ rotation (figure from[13]).

A crystallite oriented parallel to the surface ($\psi = 0$) will show a higher d-spacing because of the stress. At higher ψ angles the d-spacing is lowering significantly and the lowest value is the value at 90° where the d-spacing is the smallest. This behavior of the lattice constant as a function of the $\sin^2\psi$ is plotted in the graph of the figure 3.22. This representative $\sin^2\psi$ plot is plotted from three measurements on ψ angles at 0°, 60° and 90° of the same {hkl} planes (fixed θ-2θ angle). The slope of the graph is related with the stress state of the grain family; a negative slope means compressive stress while a positive slope implies tensile stress. The same measurements should be performed also at the other {hkl} planes of the film. Since this technique probes the strain of a crystallite, for the same stress value, the strain is not the same for crystallites of different orientation because the elastic constants of each family planes are different.

For the case of figure 3.21, assuming a thin film in rocksalt structure; the lattice constant (calculated from [001] planes) as a function of the $\sin^2\psi$ can be described by the relation:

$$a_{\psi}^{001} = a_0\left[1 + \left(2s_{12} + \left(s_{11} - s_{12}\right)\sin^2\psi\right)\sigma_{biax}\right]$$ (3.6)

Where a_0 is the stress free lattice parameter, s_{ij} are the elastic constants of the material and σ_{biax} the biaxial stress. As implied from the equation, there is an angle where the lattice constant equals the stress-free lattice constant. This is the ψ_o angle and it is shown in the figure 3.22.

The implementation of the technique requires the knowledge of the elastic constants of the material as well as the stress free lattice constant. This is not trivial though for compounds or metastable materials. The complete analysis of the model is described in appendix.

84
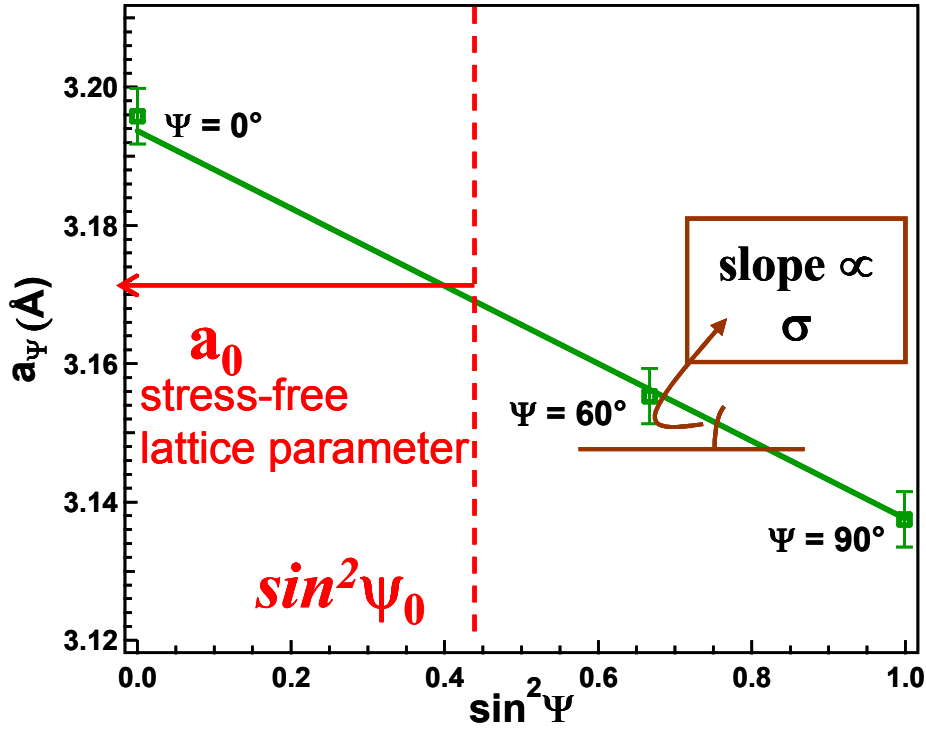
Figure 3.22: Plot of the lattice parameter as a function of the $\sin^2 \psi$.

Usually this technique is used on high order of {hkl} planes eg [422] so the error of the diffraction angle is small. But in case of thin films these high order reflections are very weak in intensity due to low diffraction volume, or in case of highly texture thin films these reflections are not accessible. A method which overcomes this problem is the crystalline group method. This method is based on the assumption that the stress is equally distributed around a probed crystallite and the crystallite behaves as a single crystal. This implies that the internal directions (planes) of the crystallite will have a different strain according to their elastic constants. So it is possible to probe high order {hkl} planes in a grain with low order {hkl} orientation. Particularly in transition metal nitrides the common structure is the rocksalt and usually the available reflections are the [111] and [002]. In table 1 are shown the values of ψ and φ angles corresponding to {hkl} intensity poles of the [001] stenographic projections.

A) Growth texture along the [001] direction						
{hkl}	**200**	**311**	**220**	**111**	**311**	**220**	**200**
$\psi\left(^{o}\right)$	0	25.24	45	54.74	72.45	90	90
$\varphi\left(^{o}\right)$	-	45	0 90	45	18.43 71.57	45	0 90

B) Growth texture along the [111] direction							
{hkl}	**111**	**311**	**220**	**200**	**311**	**111**	**311**	**220**
$\psi\left(^{o}\right)$	0	29.5	35.26	54.74	58.52	70.53	79.98	90
$\varphi\left(^{o}\right)$	-	90	30	90	0 60	30	90	0 60

Table 2: Values of ψ **and** φ **angles corresponding to {hkl} intensity poles of the A) [002] and B) [111] stereographic projection.**

3.21 Additional characterization and computational techniques

In the framework of the present thesis additional techniques have been used to obtain supplementary information about the grown samples. This extra information is about elemental composition, electronic structure as well as ab-initio calculations which provide a bunch of data about bonding, optical properties and crystal structure.

The computational method used was the linear augmented plane wave method LAPW, within the DFT using the WIEN2K[14] software. The LAPW method expands the Kohn–Sham in atomic like orbitals inside the atomic [muffin tin (MT)] spheres and plane waves in the interstitial region. The exchange correlation functional was treated either using the generalized gradient approximation[15] (GGA) or the local spin density approximation[16] (LSDA).

The analysis of the growth flux for the sputtering techniques has been done using the SRIM software. SRIM is a group of programs which calculate the stopping and range of ions (up to 2 GeV/amu) into matter using a quantum mechanical treatment of ion-atom collisions (assuming a moving atom as an "ion", and all target atoms as "atoms"). This calculation is made very efficient by the use of statistical algorithms which allow the ion to make jumps between calculated collisions and then averaging the collision results over the intervening gap. During the collisions, the ion and atom have a screened Coulomb collision, including exchange and correlation interactions between the overlapping electron shells. The ion has long range interactions creating electron excitations and plasmons within the target. These are described by including a description of the target's collective electronic structure and interatomic bond structure when the calculation is setup (tables of nominal values are supplied). The charge state of the ion within the target is described using the concept of effective charge, which includes a velocity dependent charge state and long range screening due to the collective electron sea of the target.

The SRIM software provides also details, energies and trajectories of sputtered atoms from a target as well as backscattered particles. All these results since are Monte Carlo simulations require a big sampling which varied between $1E^6$ and $1E^7$ atoms.

For compositional analysis the Rutherford backscattering spectroscopy (RBS) has been used to determine the elemental composition as well as the nitrogen stoichiometry. The RBS technique is based on the interactions between charged particles (usually alpha particles) and the nucleus of the atoms. The angle of backscattered particles as well as their energy depends on the elements present in the sample and they can be used for quantitative analysis.

Another technique used for electronic characterization is the Electron Energy Loss Spectroscopy (EELS). This method measures the energy losses of electrons from inelastic collisions on the sample. A primary beam of electrons is accelerated towards a sample and the backscattered electrons are measured as a function of energy. The amount of energy loss from the initial energy is linked to the interband and intraband absorptions of the material providing information about the band structure.

The hardness of the films was measured by nano-indentation. The nano-identation is based on the principle of the classic indentation technique but this time is for low volume materials, particular in micro or nano scale. A very small tip of known geometry is used with a very small load. The load on tip increases as the tip penetrates deeper in the material until reaches a user defined values and then retracts (in most cases). From the load-unload curve the hardness and the elastic modulus of the film evaluated using the appropriate models.

References

[1]   B. M. Clemens and J. A. Bain, MRS Bulletin **17,** 46 (July 1992).

[2]   H. P. Lamparter, in *International Max Plank research school for advanced materials*.

[3]   I. Lucks, P. Lamparter, and E. J. Mittemeijer, Journal of Applied Crystallography **37,** 300-311 (2004).

[4]   T. H. de Keijser, J. I. Langford, E. J. Mittemeijer, and A. B. P. Vogels, Journal of Applied Crystallography **15,** 308-314 (1982).

[5]   R. Delhez, T. H. de Keijser, and E. J. Mittemeijer, Fresenius' Zeitschrift für Analytische Chemie **312,** 1-16 (1982).

[6]   B. L. Henke, E. M. Gullikson, and J. C. Davis, Atomic Data and Nuclear Data Tables **54,** 181-342 (1993).

[7]   L. G. Parratt, Physical Review **95,** 359-369 (1954).

[8]   Unknown, Wikipedia Media Commons **Free Media Repository**.

[9]   T. Shibata, K. Unno, E. Makino, Y. Ito, and S. Shimada, Sensors and Actuators A: Physical **102,** 106-113 (2002).

[10]   M. Kwoka, L. Ottaviano, N. Waczynska, S. Santucci, and J. Szuber, Applied Surface Science **256,** 5771-5775.

[11]   L. B. Freund and S. Suresh, *Thin Film Materials: Stress, Defect Formation and Surface Evolution* (Cambridge University Press, 2004).

[12]   G. G. Stoney, Proc. R. Soc. Lond. A **82,** 172 (1909).

[13]   U. Welzel, J. Ligot, P. Lamparter, A. C. Vermeulen, and E. J. Mittemeijer, Journal of Applied Crystallography **38,** 1-29 (2005).

[14]   P. Blaha, K. Schwarz, G. K. H. Madsen, D. Kvasnicka, and J. Luitz, WIEN2k, An Augmented Plane Wave + Local Orbitals Program for Calculating Crystal Properties (2001).

[15]   J. P. Perdew, K. Burke, and M. Ernzerhof, Physical Review Letters **77,** 3865-3868 (1996).

[16]   J. P. Perdew and Y. Wang, Physical Review B **45,** 13244-13249 (1992).

CHAPTER 4

STRUCTURE AND

MICROSTRUCTURE RESULTS

4.1 Introduction

Transition metals include the elements of the groups IVb-VIb of the periodic table. All these materials in elemental form have either the hcp or the bcc crystal structure (Figure 4.) and additionally the valence electron configuration is not always the same. The miscibility of these elements to each other is defined by the valence configuration and varies from total miscibility (Ti-Zr) to immiscibility (Ti-Ta).

Ti $3d^2 4s^2$ *hcp*	V $3d^3 4s^2$ *bcc*	Cr $3d^5 4s^1$ *bcc*
Zr $4d^2 5s^2$ *hcp*	Nb $4d^4 5s^1$ *bcc*	Mo $4d^5 5s^1$ *bcc*
Hf $5d^2 6s^2$ *hcp*	Ta $5d^3 6s^2$ *bcc*	W $5d^4 6s^2$ *bcc*

Figure 4.1: The transition metals of groups IVb-VI with their electronic structure as well as the stable crystal structure.

The transition metals form nitride compounds. The case which we are interested in is the case of mono-nitrides. All the transition metal nitrides, except TaN and WN, crystallize in the cubic rocksalt crystal where the metal and the nitrogen atoms exhibit octahedral symmetry (Figure 4.).

The first topic of this chapter is the general structural features of binary nitrides grown by PLD. A complete series of nitrides has been grown by PLD and studied in terms of crystal structure, lattice size and density. All the grown thin films exhibited the rocksalt crystal structure and varied lattice size according to the atomic number of the metal. A more detailed study follows about the stability of cubic δ-TaN which is a metastable phase of the Ta-N system. Surprisingly, it has attracted less attention than the others and there are very scattered data about the stress-free lattice parameter as well as the general features. The detailed study includes measurements for determination of the stress-free lattice parameter as well as ab-initio calculations to validate the results.

The next topic is about the microstructure of the films. In this section the case study was the ZrN films. ZrN films exhibit different microstructure than the well studied TiN and the question is about the global validity of microstructure. The results from the ZrN films showed that the microstructure depends only on the deposition (which in turn define the energetics) conditions. The results on ZrN also have shown that the stress evolution depends on microstructure and consequently on deposition techniques.
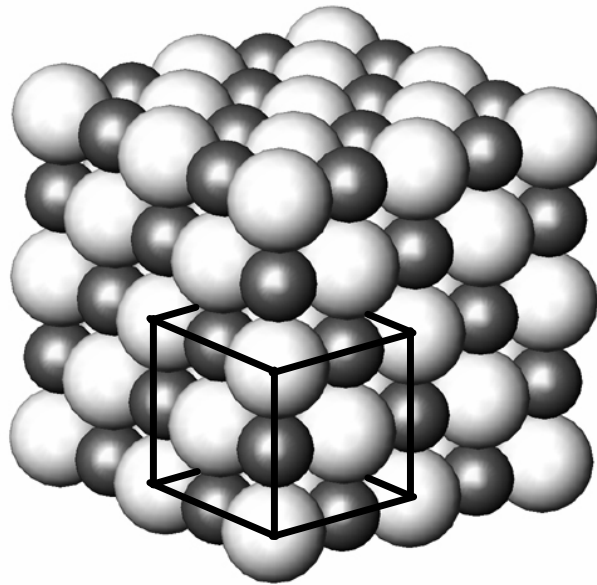
Figure 4.2: The rocksalt structure and the corresponding primitive cubic fcc cell.

Further on the next step was the growth of ternary nitrides. The ternary nitrides is the main object of the present thesis but it was essential to study first binary systems in order to predict and reveal the possible mechanisms which control the structural features of the ternary nitrides. This chapter in general deals with the structural features of the ternary transition metal nitrides such as the crystal;l structure, the bonding, the size of the lattice constant, the grain size and shape as well as the residual stresses of the grown films.

4.2 Structural features of binary nitrides

4.2.1 Binary nitrides (General)

A complete series of binary nitrides (except V and Cr) has been grown by reactive pulsed laser deposition under the same deposition conditions, on commercial n-type Si[001] crystal wafers. The growth parameters have been chosen in order to obtain pure stoichiometric

films with the $[Me]/[N]$ ratio very close to unity $(\leq \pm 2\%)$ as measured by AES. The Auger electron spectroscopy measurements have been performed in an ultrahigh vacuum (UHV) chamber, which is connected to the PLD chamber through a UHV transfer line. The AES spectra have been acquired using an electron gun (excitation energy 3keV) in a cylindrical mirror analyzer. A representative example of differential in-situ AES spectra from $\delta - TaN$ film is shown in figure 4.3. The $[Ta]/[N]$ ratio has been determined from the relative intensities of the Ta_{MNN} and N_{KLL} peaks.
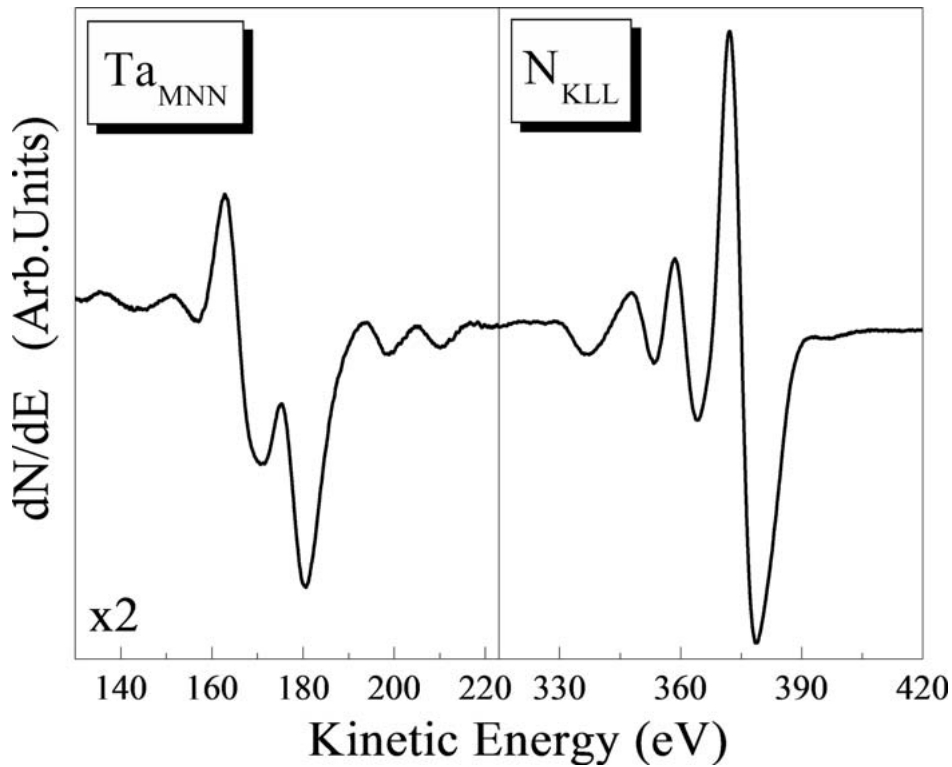
Figure 4.3: AES spectra of TaN thin film grown by PLD showing the Ta$_{MNN}$ and N$_{KLL}$ peaks.

The reproducibility of the $[Me]/[N]$ ratio for the rest nitrides grown under the same conditions was better than 2%. The acquisition of the AES spectra has shown no other elements present except some minor surface contamination of C and O.

The crystal structure of the film was studied by X-ray diffraction in Bragg-Brentano geometry using the W_{L_α} line and a line focus in a Rigaku powder diffractometer. Measurements have shown that all the binary nitrides exhibit the characteristic (111) and (200) peaks of the rocksalt structure. The cell size was calculated from the (111) interplanar spacing and the corresponding graph as a function of the metal atomic number is plotted in the figure 4.4.

92
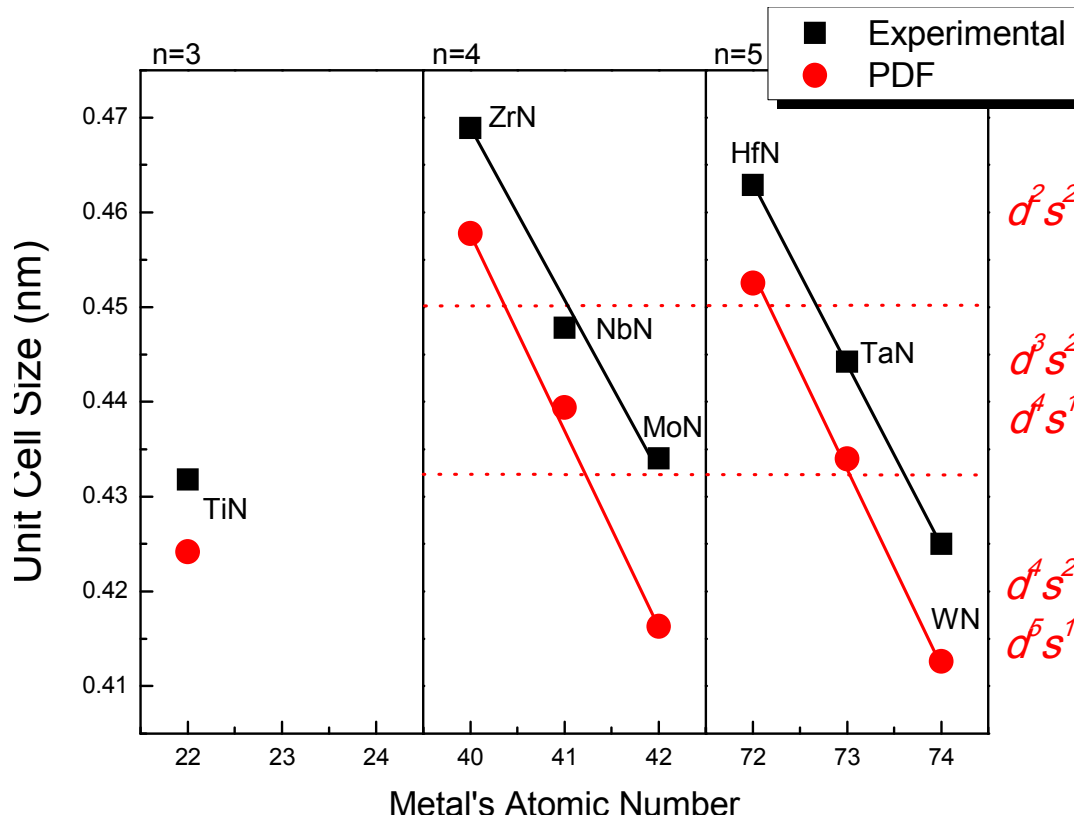
Figure 4.4: The cell size of the binary nitrides grown by PLD as a function of the metal atomic number. The cell size was calculated from the (111) peak.

The experimental cell sizes are consistently larger comparing to the values of the PDF database. This is exclusively due to in-plane compressive stresses, which are relieved after vacuum annealing.

The density of the films has been measured by XRR using a Siemens D5000 diffractometer using the Cu K_a and a Goebel multilayer mirror as monochromator. The density of the binary nitrides is shown in figure 4.5 and for all films is lower than the density in the bulk form except for TiN. The creation of voids inside the deposited film is reducing its density and it is very common for deposition under room temperature. The difference between the bulk and the experimental values for the other nitrides except TiN, is due to the lower energetic deposition conditions. The target atoms require more photons to be ionized (multi-photon ionization potential) thus making the ionization less probable and the films are deposited with voids. Only in the case of TiN the films were denser than the bulk value because of the ionized atoms.
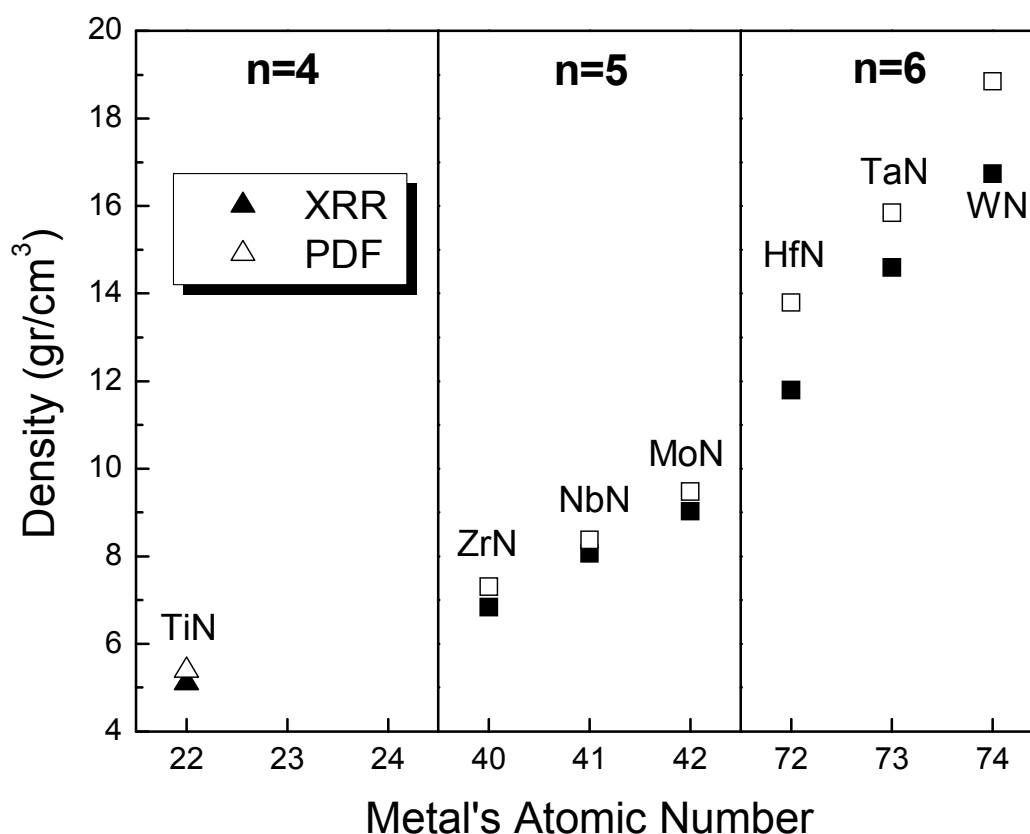
Figure 4.5: The experimental and the bulk values of density as a function of the metal atomic number fror PLD-grown films.

4.2.2 Case study TaN; Stability

A very good candidate system for this study is the tantalum mononitride. The Ta-N system has many stable compounds like the hegaxonal TaN, the Ta_3N_5 and Ta_2N as well as the metastable cubic rocksalt TaN. Surprisingly, the δ-TaN phase did not attract as much attention as the equivalent δ-TiN, δ-CrN and δ-ZrN, despite its technological importance. There is still lack of data regarding the density, the stress-free lattice parameter and the texture of the stoichiometric δ-TaN, which can be used as a model system for understanding the behavior of other d^3 transition metal nitrides.

The δ-TaN films, >300 nm thick, were grown on commercial Czochralski-grown n-type Si [001] crystal wafers using reactive PLD. The PLD experiments were performed in conditions same as the growth of the binary nitrides in the start of this chapter. Representative samples were vacuum annealed at 850°C for 3h in order to change the stress state and evaluate the stress-free lattice parameter. The stoichiometry of the films was evaluated by *in-situ* AES

and the crystal structure by XRD in Bragg-Brentano geometry. The density of the films as well as the stress state has evaluated by XRR and the $\sin^2 \psi$ method, respectively.

The *in-situ* AES spectra have shown (see fig 4.3) that the films consist exclusively of Ta and N. The nitrogen to metal ratio has been evaluated and found to be 0.98 ± 0.02. The XRD pattern of the films (see fig 4.6) exhibited exclusively the (111) peak of the rocksalt structure indicating that the TaN films were strongly textured along the [111] direction. The determined lattice parameter from the (111) peak was a_{111}=0.443 nm, which is larger than the value of 0.434 nm corresponding to δ-TaN powder. This implies that the films were in-plane compressed. The usually forbidden Si(200) peak was also manifested weakly due to wafer orientation[1].
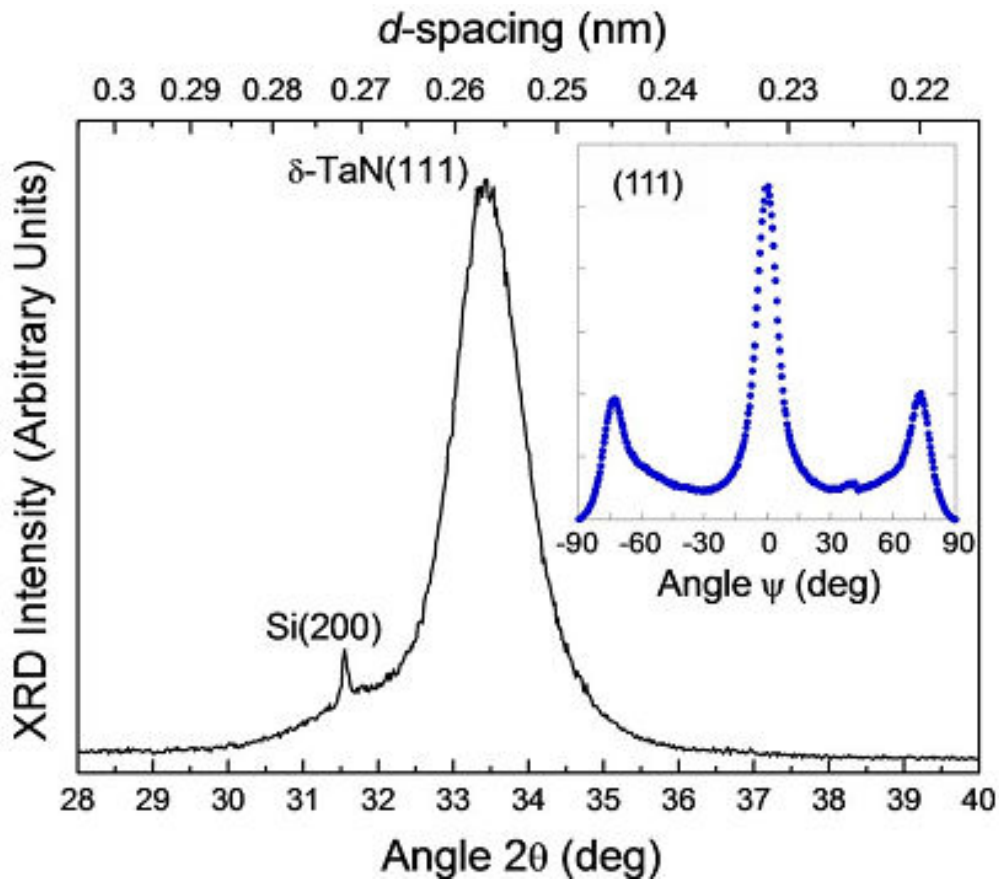
Figure 4.6: XRD pattern of a textured PLD-grown δ-TaN film; the inset shows a tilt ψ scan for the {111} planes family, demonstrating the [111] fiber axis.

The residual stresses in δ-TaN thin film in the as-grown and annealed states were determined using the $\sin^2 \psi$ method[2,3]. Since the films grown by PLD were highly textured with a [111] fiber axis (see Fig. 4.6 inset), the ideal direction method, also known as the crystallite group method[2,4-6], was employed to measure intragrain elastic strains in specific, directions, where ψ is the tilt angle between the sample surface normal and normal to the {hkl} diffracting planes and ϕ is the azimuthal angle between two in-plane principal axis along which the

biaxial σ_{11} and σ_{22} stresses are defined. For a {hkl} reflection at given ψ value, the angle ϕ was fixed according to the {111} pole figure in order to probe the same subpopulation of grains. Using linear elasticity theory and assuming an equibiaxial stress state $\sigma_{11}=\sigma_{22}=\sigma_{biax}$, one may relate the evolution of the lattice parameter a_0 with ψ angle; a simple and direct graphical determination of a_0 can be made by performing a strain-stress analysis on the same sample with at least two different stress states, corresponding in the present case to the as-grown and annealed states.
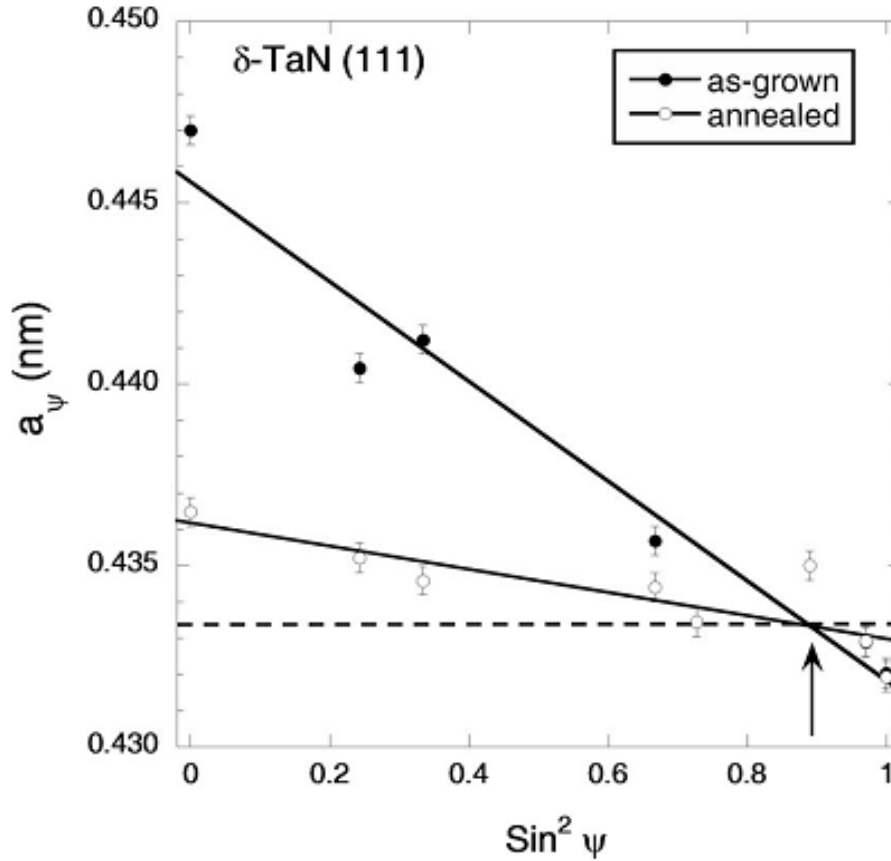
Figure 4.7: $\sin^2 \psi$ **plot of δ-TaN films as grown (black circles) and vacuum annealed (white circles). The dotted line points the stress free lattice parameter.**

The $\sin^2 \psi$ plots for the as-grown and annealed TaN samples are presented in figure 4.7. It is evident from the negative slopes of the $\sin^2 \psi$ lines that the films are under compression. Moreover, the significant decrease in the slope after annealing attests for a stress relaxation. The two lines are intersecting at a $\sin^2 \psi$ value of 0.9, the ordinate of this intersection point being 0.433 nm. As originally stated by Cornella et al[7]. the intersection of the plot of the respective a, versus $\sin^2 \psi$ indicates the stress-free lattice parameter directly i.e., without any knowledge on film elastic data.

The obtained a_0=0.433 nm value is in good agreement with the value of 0.435 nm reported by Shin et al.[8-10] on polycrystalline δ-TaN films using a similar strain-stress analysis and the value of 0.433 nm reported by Wang et al.[11] on epitaxial TaN layers. However, it may be noticed that the position of the intersection point does not correspond to the expected $\sin^2 \psi_0$ value calculated using a biaxial stress model.
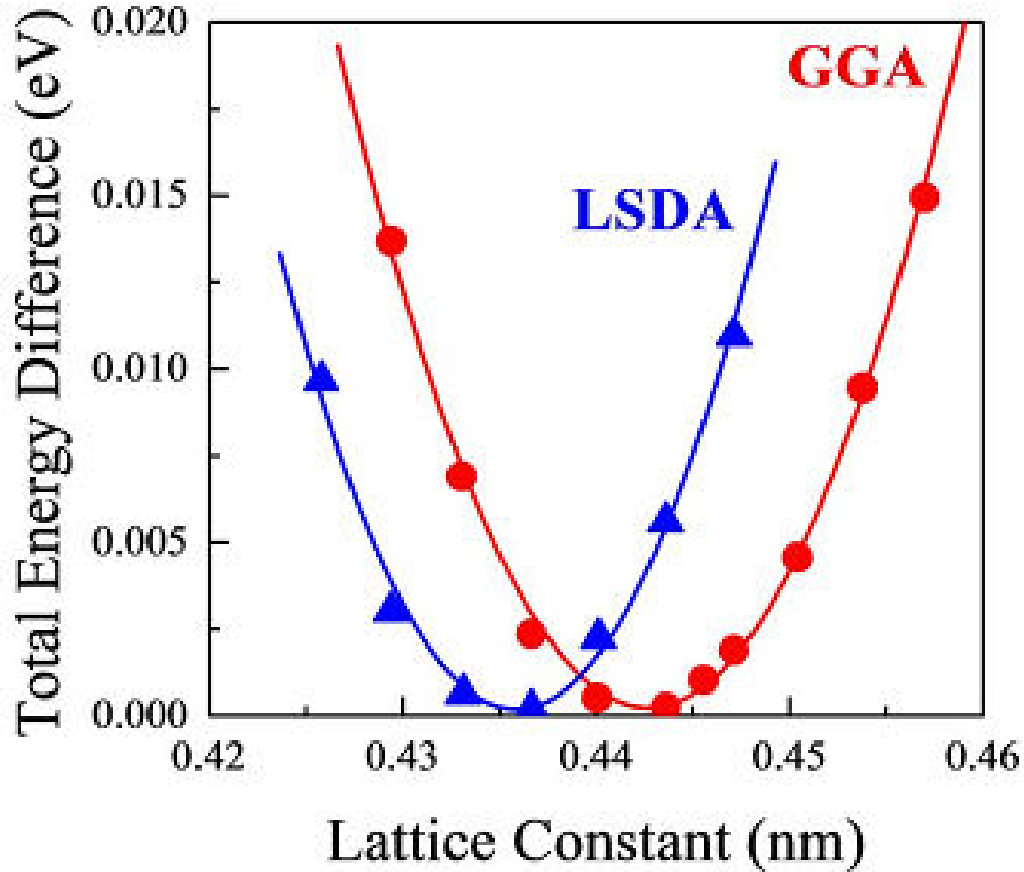
Figure 4.8: Total energy of δ-TaN calculated using the GGA and the LSDA methods

This departure can be explained by assuming a triaxial stress state, including a hydrostatic growth stress component σ_{hyd} due to the introduction of defects during deposition with energetic species. This behavior has been observed in magnetron or dual ion beam sputtered TiN films and rationalized using appropriate stress modeling.

The lattice parameter of δ-TaN was also determined by *ab-initio* calculations using the GGA (circles) and LSDA (triangles) approximations, as shown in figure 4.8. We note that in this figure we shifted the minimum energy values to zero for comparison reasons (by 31 361.84 and 31 342.72 eV for GGA and LSDA, respectively). It comes out that the LSDA value of the equilibrium lattice parameter (0.4336 nm) is in very good agreement with our

experimental estimation (0.433 nm), while the GGA value (0.4419 nm) is overestimated, a finding that is common in these calculations. From these curves we also determined the bulk modulus 337.5 and 413 GPa from both GGA and LSDA methods, respectively.
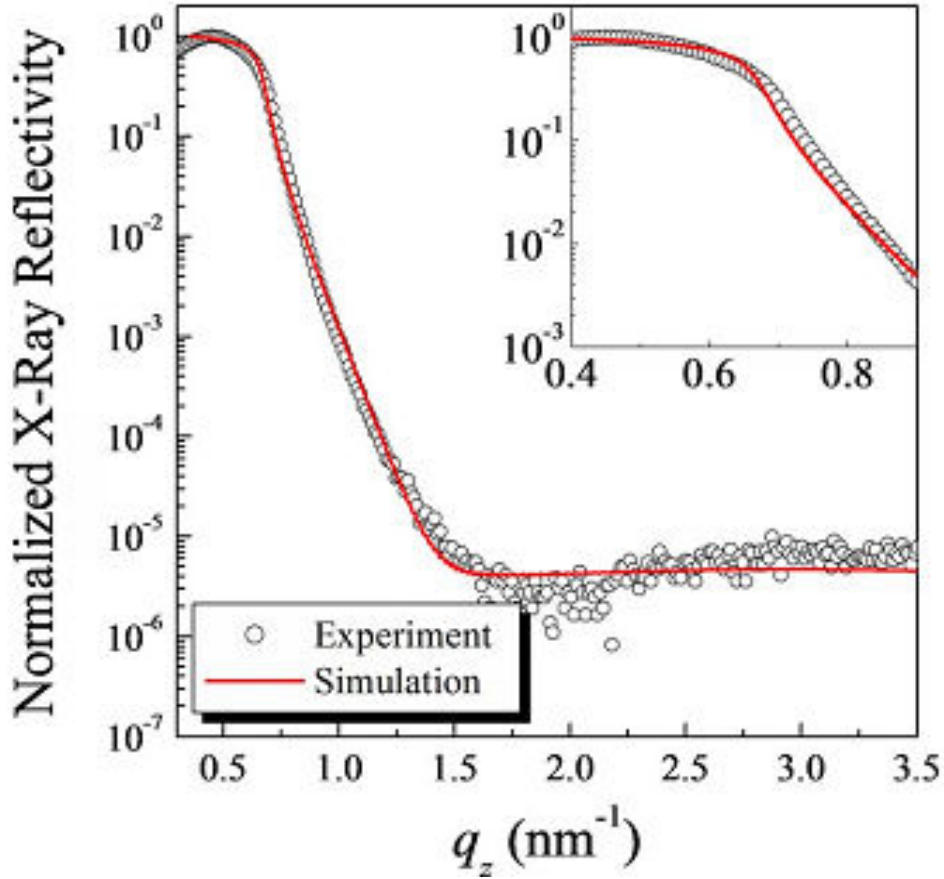
Figure 4.9: XRR scan from δ-TaN film and the corresponding Parratt fit; the inset shows the details around the critical angle.

The XRR scan from a representative δ-TaN film is depicted in figure 4.9. No interference fringes are manifested due to the relatively large thickness of the sample (>300 nm). The XRR data were simulated using Parratt's formalism[12]. The surface roughness was found to be 1.9 nm and the average density was found to be 14.6±0.9 g/cm3, suggesting that there exists a void volume fraction of fV=7%. This value of fV is rather small for nitride samples grown at RT[13].

The stabilization of δ-TaN was not trivial in the case of magnetron sputtering deposition. The deposition in the same conditions as other binary nitrides like TiN and ZrN could not lead to stable cubic TaN. Several tries with different parameters (nitrogen flow, substrate temperature) resulted always in a mixture of phases figure 4.10), included the cubic TaN. The only parameter that allowed the formation of pure cubic TaN films was the pressure. By increasing the pressure one order of magnitude higher than the conditions of the TiN or

ZrN the δ-TaN was stabilized. The heavier element of Ta in addition to the low working pressure resulted in high kinetic-momentum flux to the deposition surface. This energetic bombardment induced a lot of stress in the crystallites not allowing the stabilization of cubic crystallites in contrast with the lighter atoms of Ti and Zr.
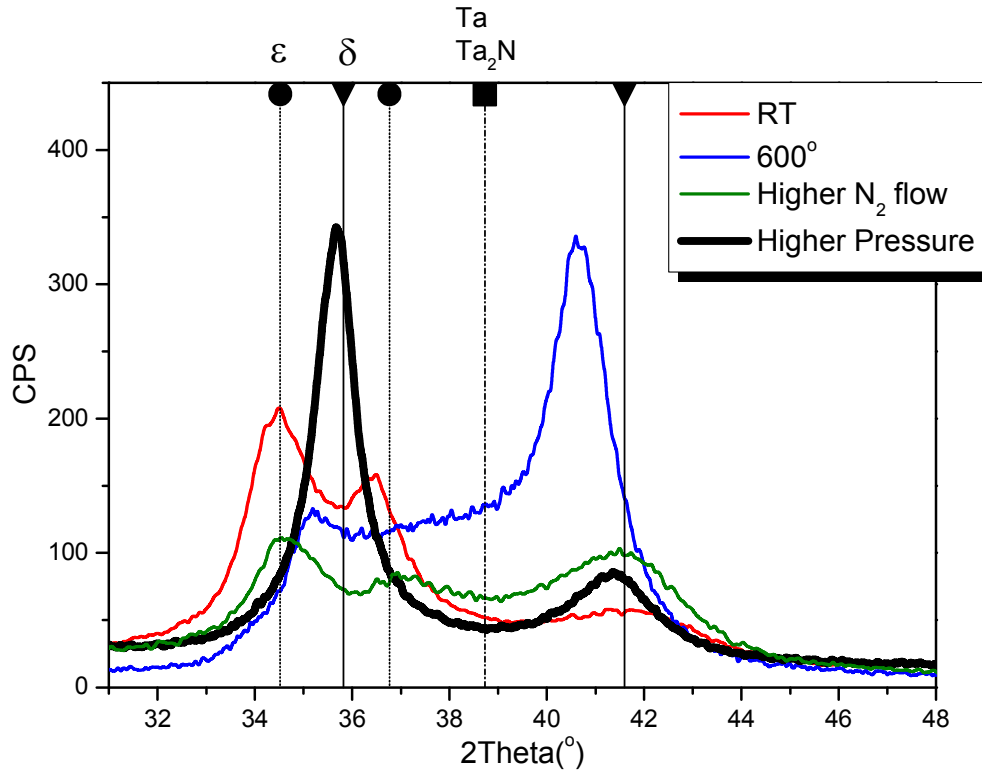
Figure 4.10: XRD pattern of reactively sputtered TaN. Several deposition parameters changed (from the standart parameters of other binary TMN) in order to obtain the δ-TaN. The cubic TaN was only stabilized at higher working pressures.

4.2.3 Case study ZrN; Microstructure

As described in chapter 2 the microstructure of the thin film is a very important parameter. In order to study the microstructure as a function of the deposition parameters we deposited various samples by magnetron sputtering and examined them in terms of microstructure. As a case study the ZrN was chosen in order to find the similarities and the differences between the well studied in the literature TiN.

ZrN_x films were grown at T_s=300°C using reactive magnetron sputtering from a 7.5-cm-diameter Zr (99.92 % purity) target in Ar+N_2 atmosphere. All films were grown on Si (001) substrates covered with amorphous native oxide (~2 nm), so that no texture inheritance from the substrate is expected to play a role on the preferred orientation of the ZrN_x films. The target to substrate distance was 18 cm and the base pressure of the vacuum chamber 2×10^{-6} Pa. Films with thickness ranging from 30 to 300 nm were deposited under various deposition

conditions (total pressure between 0.13 and 0.42 Pa, balanced/unbalanced magnetron configuration) at a fixed substrate bias of ~−60V. The N_2 flow was adjusted to 0.7sccm so as sputtering occurred in metallic mode, just before the hysteresis cycle (see fig. 4.11).
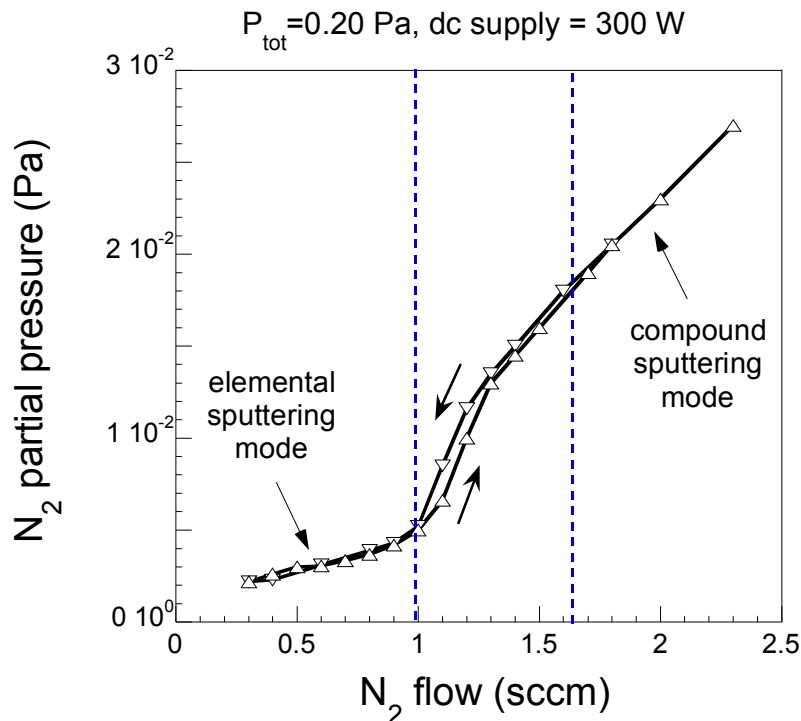
Figure 4.11: The hysteresis curve of a Zr target as a function of the nitrogen flow.

This led to the formation of ZrN_x films with x~0.96±0.04 and Hf impurity lower than 0.3 at.%, as determined by Rutherford backscattering spectroscopy (RBS), and a typical growth rate in the range 2.1-3.1 Å/s depending on the total pressure (see Table 1). Complementary RBS analysis have shown that ZrN_x films sputtered at a higher N_2 flow (typically 2.0 sccm, corresponding to a poisoned target mode) were closer to stoechiometry (x=1) but exhibited a lower degree of crystallinity.

Unlike TiN films, for which a clear columnar growth with 'V-shaped' facetted columns were formed as a result of competitive grain growth[14] , ZrN films grown at 0.20 Pa exhibited a denser structure with columns composed of more globular grains. Figure 4.12 shows two XRR scans representative of medium (0.20 Pa) and high (0.42 Pa) pressure sputtering conditions. With increasing pressure an increase in surface roughness and a decrease in film density are observed. In particular, the film deposited at 0.42 Pa exhibits a density of 5.8 g.cm^{-3}, which is 20% lower than the bulk value of 7.3 g.cm^{-3}.

Table 3: Deposition conditions and characterization results for magnetron sputtered deposited ZrN samples.

Sample	ZrN-M08-19	ZrN-M08-25	ZrN-M08-6	ZrN-M09-7	ZrN-M08-24
Working pressure (Pa)	0.13	0.20	0.19	0.30	0.42
Substrate temperature	300°C	300 °C	300°C	300°C	300 °C
Bias voltage (V)	-64	-64	-52	-60	-64
Magnetron Configuration	balanced	balanced	unbalanced	balanced	balanced
Thickness (nm)	103	117	269	131	157
Growth rate (Å/s)	2.10	2.34	2.40	2.63	3.11
Density (g.cm^{-3})	7.3 ± 0.1	7.3 ± 0.1	7.4 ± 0.1	6.9 ± 0.1	5.8 ± 0.1
Surface roughness σ_{XRR} (Å)	8	19	/	25	36
T_{111} *	0.41	0.53	0.64	0.60	0.83
(111) FWHM (Deg.)	0.53	0.36	0.52	0.31	0.38
(002) FWHM (Deg.)	0.62	0.73	0.66	0.73	0.91

*For randomly oriented grains, T_{111}=0.47

The formation of underdense and relatively rough films may be explained by the presence of voids in the film due to low-mobility conditions. Indeed, at a pressure of 0.42 Pa, a relatively large energy loss of the incoming particles (Zr sputtered atoms and backscattered neutrals) takes place due to collision with the gas phase[15].
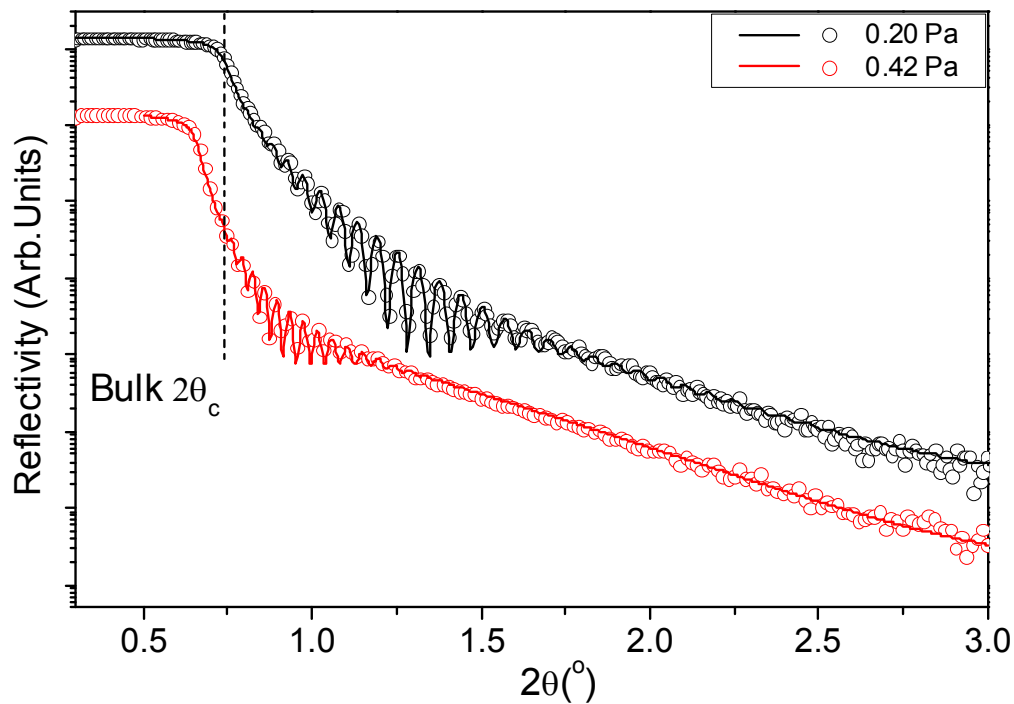
Figure 4.12: XRR scans from two ZrN samples grown at low and high pressure.

Consequently, surface roughness develops as a result of a wider angular distribution of the deposition flux, shadowing between columns and limited surface diffusion[15-17]. This open (porous) film structure favours substantial oxygen incorporation along the column (grain) boundary[18], which can also contribute to the decrease in film density. Note also that an increase in deposition rate is found at higher pressure (see Table 1), attesting also of shadowing effects and formation of outgrowths. Molecular dynamics simulations have shown that these outgrowths can explain to the formation of closed-off voids and possible alignment of voids along the film growth direction[19].

Figure 4.13 shows the evolution of θ–2θ XRD patterns of ~120 nm thick ZrN_x films with total pressure. All films exhibit the Na-Cl type cubic structure with (111), (002) and (220) main reflections. A change from (002) to (111) preferred orientation is observed with increasing pressure.
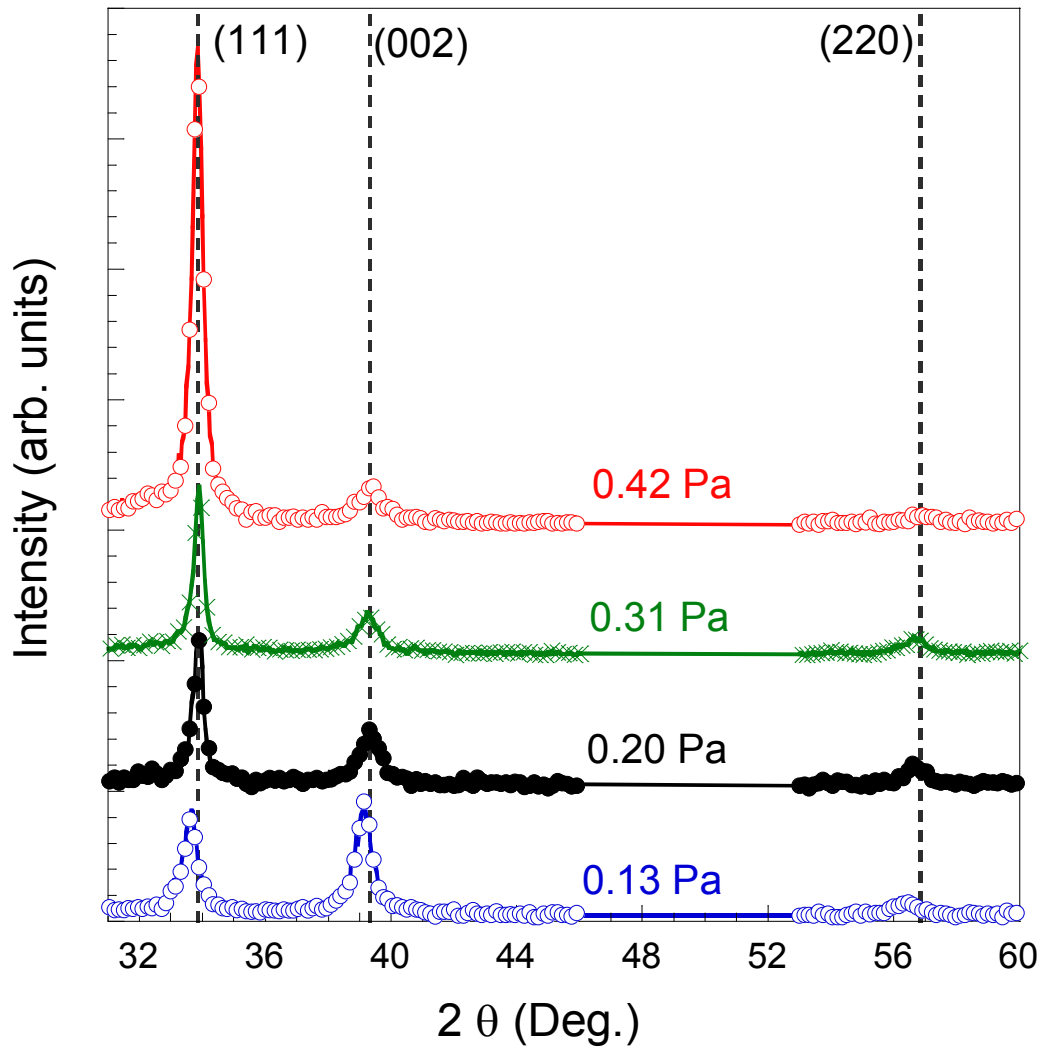
Figure 4.13: XRD pattern of ZrN films grown at various pressures.

The (111) texture coefficient defined as $T_{111}=I_{111}/(I_{111}+I_{002}+I_{220})$, where I_{hkl} is the integrated intensity of the corresponding (hkl) Bragg reflection, and the full width at half maximum (FWHM) of (111) and (002) peaks are reported in Table 1. A progressive increase of T_{111} together with a systematic larger FWHM for the (002) peak is seen with increasing pressure. If we assume the same level of microstrain in both grains, this would indicate a lower vertical coherency length (grain size) for (002) grains. This could indicate that (002) grains, which have the lowest surface energy, are formed during renucleation due to ion bombardment, which is more effective at lower pressure. Modifications of FWHM and T_{111} texture coefficient are noticed at larger film thickness, indicating that preferred orientation evolves in a complex way.
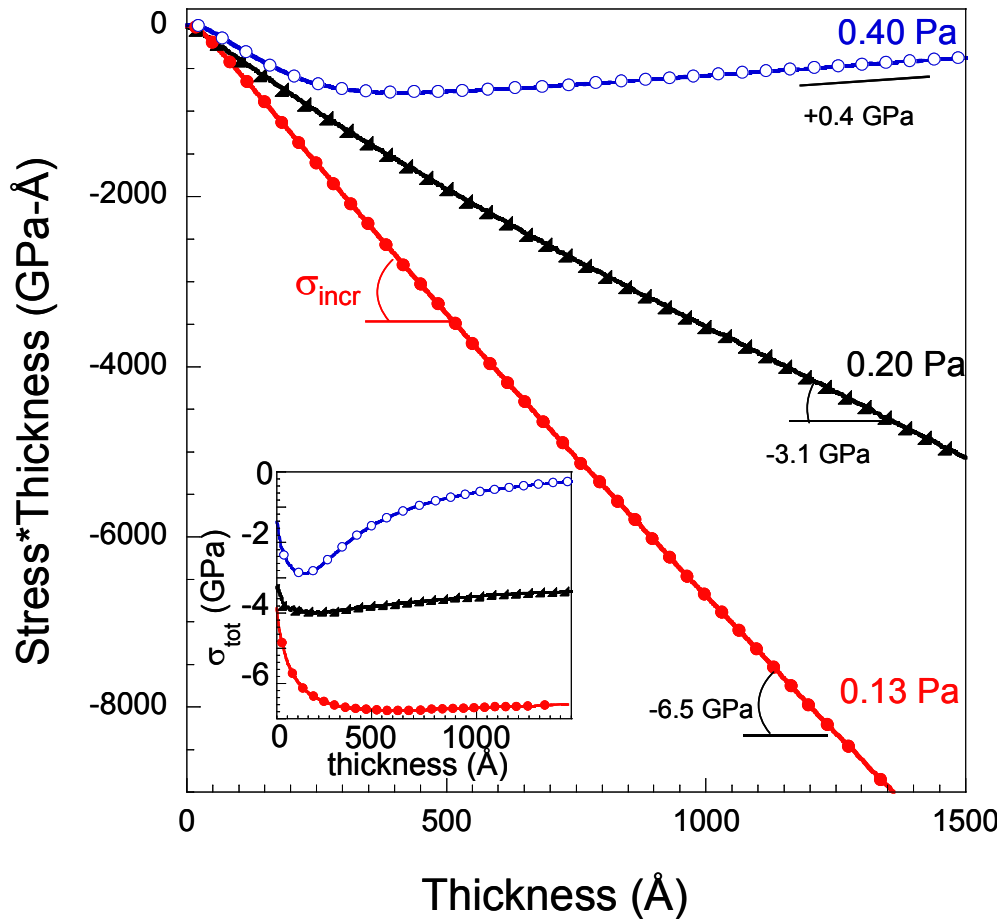
Figure 4.14: Evolution of the stress*thickness product vs. film thickness recorded in *real time* during magnetron sputtering of ZrN films at different total pressures.

From established structure zone models[20,21] (SZM), a 'Zone Ib' or 'Zone-Ic'-type structure would be expected at high pressure conditions (0.42 Pa), but the presence of an out-of-plane preferential orientation and textural evolution with pressure and thickness suggest that adparticles have sufficient mobility to diffuse from one grain to another[16]. It may be inferred that the bombardment of energetic particles provide this delivery of kinetic energy to

103

the film. This film bombardment is manifested by a compressive stress contribution to the overall film stress, as shown from the *in situ* stress experiments reported in figure 4.14.

A compressive steady-state stress is observed for ZrN films deposited at 0.13 Pa, with a very large incremental stress $\sigma_{incr} \sim -6.5$ GPa (σ_{incr} is given by the slope of stress*thickness product vs. thickness and reflects the stress change due to additional amount of a newly deposited layer or relaxation in the underneath film). At higher pressures, a decrease or even a reversal from negative to positive σ_{incr} values is noticed, indicating a change in the predominant stress build-up mechanism, as relaxation effects were ruled out previously[18]. The overall stress σ_{tot} is plotted in the insert of fig. 4 as function of film thickness, where gradients are clearly evidenced at high pressure conditions (> 0.2 Pa). These gradients originate from two kinetically competing intrinsic stress sources: ion/atomic peening[22] creating ingrown defects and associated compressive stress and attractive forces between under-dense neighboring columns[23] as well as possible voids formation leading to the development of tensile stress, this latter contribution is becoming predominant at later growth stages in the case of low mobility conditions. The values of σ_{tot} are reported in Table 2 for the different samples also investigated by XRD.

Table 4: Stress results from XRD and wafer curvature technique of ZrN samples grown by magnetron sputtering.

	ZrN-M08-19	ZrN-M08-6	ZrN-M08-24
σ_{tot} (GPa)	-6.6	-3.1	-0.25
σ_{XRD}^{111} (GPa)	-3.3 ± 0.3	-3.0 ± 0.3	-1.0 ± 0.2
σ_{XRD}^{002} (GPa)	-4.1 ± 0.5	/	/
a_0(Å)	4.596 ± 0.003	4.582 ± 0.003	4.582 ± 0.003
σ_{th} (GPa)	0.2(±0.1)	0.2(±0.1)	0.2(±0.1)
$\overline{\sigma_i}$ (GPa)	-4.0 ± 0.5 /	-3.2 ± 0.3 /	-1.2 ± 0.2
$\Delta\sigma = \sigma_{tot} - \overline{\sigma_i}$ (GPa)	-2.6 ± 0.5	0.1 ±0.3	1.0 ± 0.2

Figure 4.15 shows the evolution of the $\sin^2\psi$ plots of ZrN_x films deposited at 0.13, 0.20 and 0.42 Pa. Measurements from the (111)-oriented grains are reported for films grown at higher pressures (for which $T_{111} > 0.6$), while for the film grown at 0.13 Pa (T_{111}=0.42), data for both (111) and (001) textures have been measured. A standard stress model assuming an equi-biaxial stress in the specimen plane and elastic compliance data of Nagao et al.[24]

(C_{11}=537 GPa, C_{12}=118 GPa and C_{44}= 120 GPa, giving an anisotropy factor of 1.75) was used to fit the data.

Since all films were grown at the same deposition temperature T_s=300°C, the thermal stress contribution was identical (σ_{th}~0.2 GPa, as calculated using linear thermal expansion coefficients taken from Refs. [25] and [26] for Si and ZrN, respectively) and was subtracted from the σ_{XRD} values to get the intrinsic stress σ_i. Values are reported in Table 2.
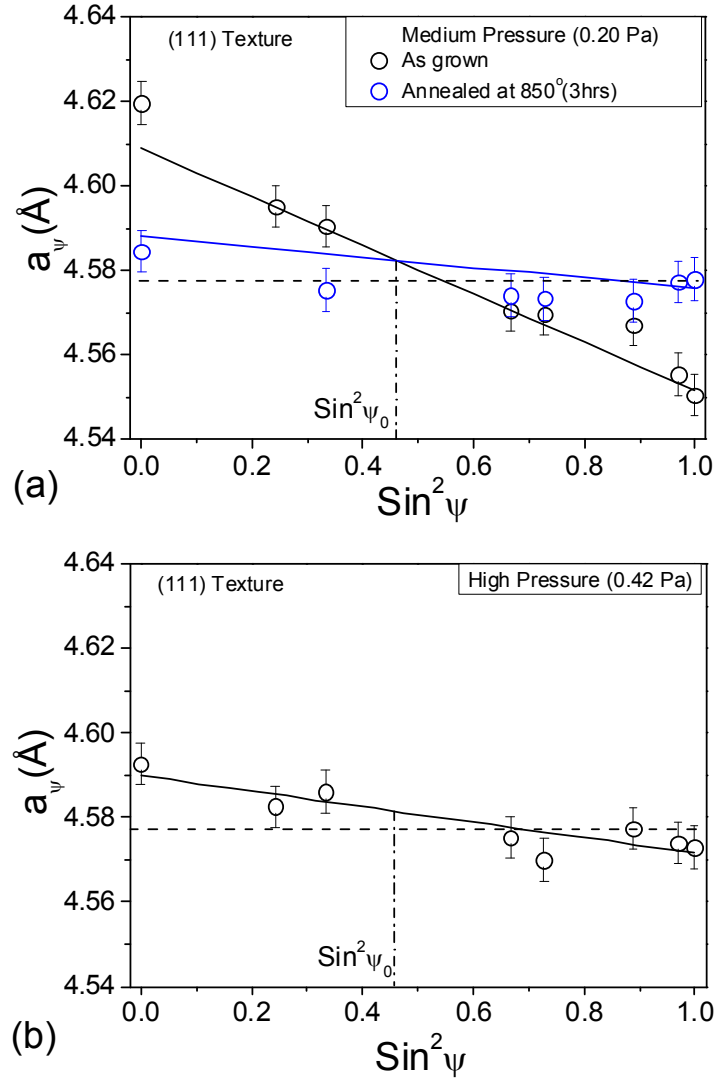
Figure 4.15: $Sin^2\psi$ **plots of ZrN films sputtered at 0.20 Pa (a), 0.42 Pa (b) and 0.13 Pa (c). Horizontal dashed line corresponds to the ZrN bulk lattice parameter (4.578 Å)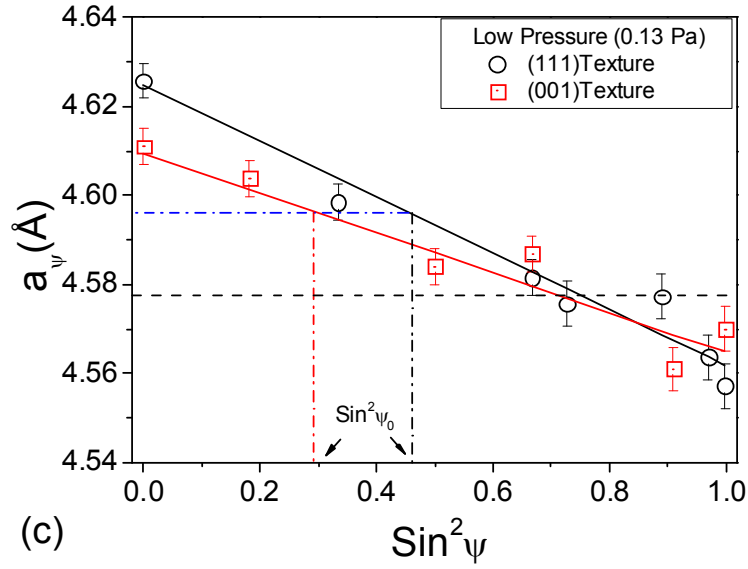. Vertical dashed-dotted lines correspond to strain-free directions at $sin^2\psi_0$ as determined using a standard biaxial stress analysis.**

For the film grown at 0.20 Pa, data are shown for the as-grown and annealed samples (fig. 4.15.a). A reduction of the stress is clearly visible after annealing at 850°C for 3h, indicating that the majority of the growth-induced defects have been relieved, similarly to TiN films grown by dual ion beam sputtering[27]. Fitting the whole data yielded stress values σ_{XRD} of -3.1 ± 0.3 GPa and -0.65 ± 0.3 GPa for the as-grown and annealed states, and a stress-free lattice parameter $a_0 = 4.582 \pm 0.003$ Å, close to the bulk value (4.578 Å). The a_0 value can be also determined graphically from the intersection points of the two $sin^2\psi$ lines at $sin^2\psi_0 = 0.46$ for the (111) texture. Also, for this sample grown at 0.20 Pa, the σ_i and σ_{tot} values are found to be equal within the experimental uncertainty (see Table 2). For the film grown at 0.42 Pa, the compressive stress level is significantly reduced but still compressive (see fig. 4.15.b). A value of $\sigma_{XRD} = -1.0 \pm 0.2$ GPa is obtained, which is different from the σ_{tot} value of -0.25 GPa derived from *in situ* experiment. The quantity $\Delta\sigma = \sigma_{tot} - \overline{\sigma_i}$, which one can relate to the contribution of column (grain) boundary, is found to be positive in this case (+1.0 GPa). For the film grown at low pressure (0.13 Pa) where a mixed (111)+(001) texture exists, the stress is found to be compressive in both subset of grains (see fig. 4.15.c). However, in this case the quantity $\Delta\sigma$ is largely compressive (-2.6 GPa). Note that a higher stress level is found for (002)-oriented grains. Therefore strain-energy minimization cannot be invoked to explain the (001) preferred orientation ($T_{111} < 0.47$). Also, the value of a_0 is found to be larger (4.596 Å), which corresponds to a lattice expansion of 0.3% compared to bulk. Part of this expanded stress-free lattice parameter can be accounted for by a higher Ar entrapment due to the high

energy of backscattered Ar at 0.13 Pa[15]. In that case a more appropriate stress modelling would require the use of a triaxial stress including a hydrostatic stress component[3].

Concluding, the comparison of stress values determined from *ex situ* XRD and *in situ* wafer curvature provides some interesting insights into the stress producing mechanisms in TM nitride thin films, and in particular into the contribution of grain boundary. At low pressure, the continuous ion/atom bombardment creates intra-column growth-induced defects (the magnitude of this stress source is estimated at -4 to -3 GPa) but promotes also the incorporation of excess atoms in the column boundary. Compared to high-mobility metals[28], this flow of atoms into the grain boundary is not reversible for the case of TM nitrides. The resulting structure is fully-dense with a mixture of (002) and (111) grains and has a smooth surface. As pressure increases, the mobility of the adatoms is reduced and a lower mass transport along the surfaces and grain boundaries occurs. At intermediate pressure, the overall stress remains compressive, as atomic peening process is still predominant; the development of a (111)-oriented film could be explained by anisotropy of adatoms surface diffusion. At higher pressure, due to thermalization, surface mobility is much lower and under-dense films grow in a global tensile stress due to grain boundary attractive forces, while crystallites can remain under in-plane compression as some defects can still be created. The resulting stress is inhomogeneous along the growth direction and the microstructure consists of (111)-oriented and voided columns with rough top surface.

4.3 Structural features of ternary nitrides

4.3.1 Introduction

Until now the structural features of binary nitrides have been studied. We have seen how the energetic conditions affect the microstructure which is not material related but depends on the deposition condition. The next section focuses on the addition of another element, in order to form single phase ternary nitrides.

The first case study is the ternary nitride from metals in the same group IVb. These metals share the same valence configuration $d^2 s^2$ and are soluble to each other in the elemental form. The question is how does structure and microstructure is affected by adding a third element. Since the results on binary nitrides have shown that the energetic conditions are responsible for the microstructure, the addition of another element increases significantly the energy flux thus changing considerably the microstructure. The elements used for the first case study are the Ti and Zr.

4.3.2 Case study Ti-Zr-N

4.3.2.1 PLD-grown Ti-Zr-N

We have grown $Ti_xZr_{1-x}N$ ternary transition metal nitrides on Si{001}, by reactive pulsed laser deposition and reactive magnetron sputtering technique. The growth conditions implemented on this study, of ternary $Ti_xZr_{1-x}N$, were used previously to grow stoichiometric cubic binary nitrides. The sample composition, in the case of PLD, was changing by using mixed Ti-Zr targets (99.95% purity) of varying fractions; the deposition took place in N_2 ambient at Room Temperature (RT). The sputtered samples were deposited at T_s=300°C from 7.5cm diameter water-cooled targets electrically connected to a DC power supply.

The composition of the sputtered samples was changed by varying the power supply of the targets. The composition of the films was determined by Auger Electron Spectroscopy (AES) and by Energy Dispersive X-rays (EDX). The crystal structure was investigated by X-Ray Diffraction (XRD) in Bragg-Brentano geometry, using the Cu K_α monochromatized line.

The XRD patterns of the films exhibited only the (111) and (200) peaks of the rocksalt structure without any fine structure, indicating perfect solid solutions over the full range of x (0<x<1), demonstrating the general property of TiN and ZrN being fully miscible to each other. In figure 4.16 it is shown the comparison between binary ZrN and ternary $Ti_xZr_{1-x}N$ XRD patterns, as well as the substitution of one metal with the other (inset).
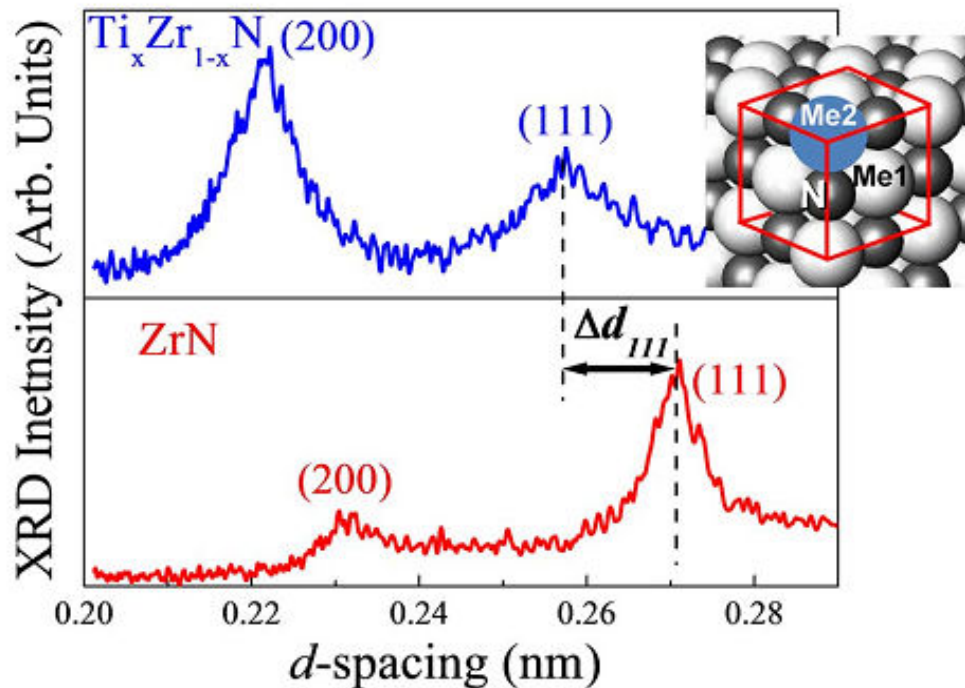
Figure 4.16: XRD patterns from ZrN and $Ti_xZr_{1-x}N$ films revealing their rocksalt structure with the one metal being in substitutional positions of the other (inset).

The cell sizes (a_{111}) were calculated from the (111) interplanar spacings and are displayed in figure 4.17 as a function of the composition x. The lattice constant versus composition follow a line resembling Vegard's rule but not coinciding exactly.
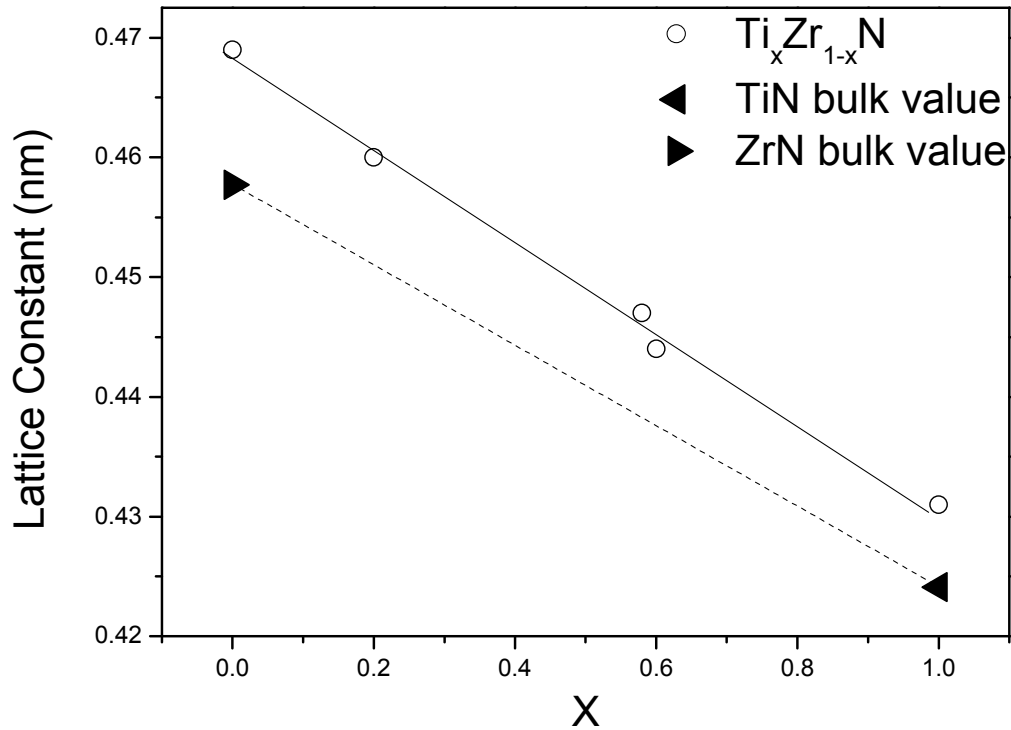
Figure 4.17: The lattice constant of Ti$_x$Zr$_{1-x}$N films as a function of composition x and the corresponding values from Vegard's rule (dotted line).

The a_{111} is expanded compared to the expected values of Vegard's rule, defined by the values of the bulk TiN and ZrN. This is attributed to in-plane compressive stresses induced by the deposition process as mention earlier in this chapter.

Ab-initio calculations have also been performed using LAPW-DFT algorithms for the Ti$_x$Zr$_{1-x}$N system for various x. The total valence charge density is shown in figure 4.18 for three distinct cases, ZrN, Ti$_{0.5}$Zr$_{0.5}$N and TiN. The pure metallic features of the ZrN and Ti$_{0.5}$Zr$_{0.5}$N are clearly seen as well as a change in the TiN case where a very minor ionic bond appears.
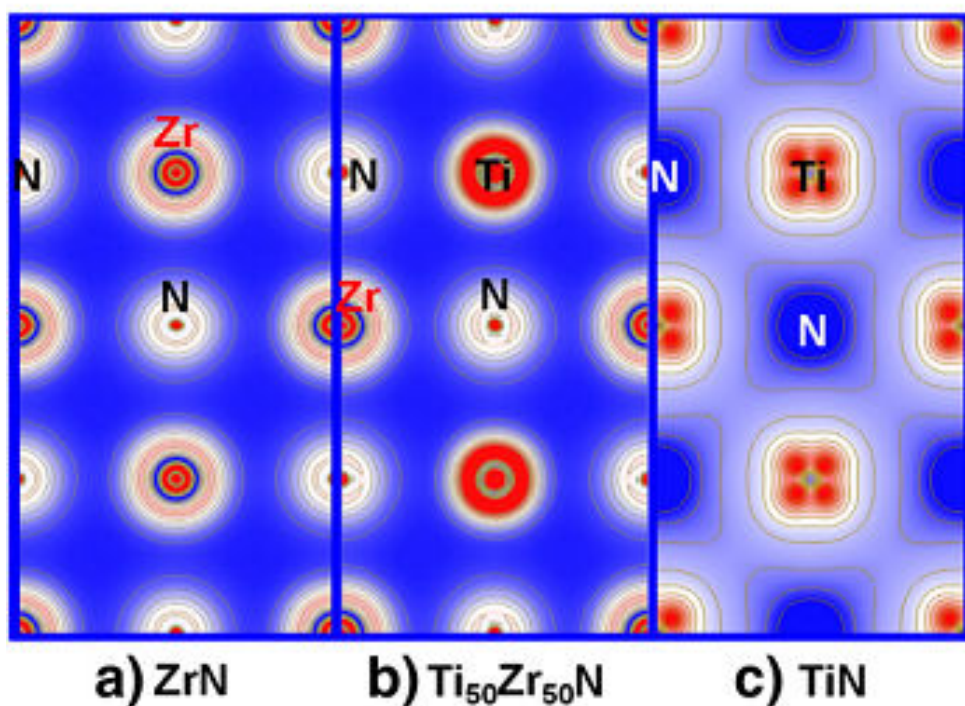
Figure 4.18: Valence charge density in the (001) plane, a) ZrN, b) Ti$_{0.5}$Zr$_{0.5}$N and c) TiN

4.3.2.2 DCMS-grown Ti-Zr-N

Another set of ternary Ti$_x$Zr$_{1-x}$N films were deposited at T$_s$=300°C on Si (001) wafers covered with native oxide (~2 nm) using a magnetically-unbalanced magnetron sputtering system equipped with three confocal planar magnetron sources. The Ti (99.995% purity) and Zr (99.2% purity, including Hf) targets were 7.5-cm-diameter water-cooled discs electrically connected to a dc power supply. A negative bias of −60 V was applied during deposition to the substrate using an RF power supply. The sputtering was monitored at constant power and the atomic fraction x(or y) in the Ti$_{1-x}$Zr$_x$N films was varied by changing their respective target powers. The total pressure used to grow the Ti$_{1-x}$Zr$_x$N films was 0.19 Pa. In all samples, the N$_2$ flow was adjusted so as sputtering occurred in metallic mode with a relatively large deposition rate. Film thickness was varied between 60 to 300 nm.

The elemental composition of the films was determined using Rutherford backscattering spectroscopy (RBS) using 2 MeV He+ ions at normal incidence to the sample surface with a PIPS (Passivated Implanted Planar Silicon) detector located at a scattering angle of 165°. The spectra of backscattered alphas particles were analyzed using the SIMNRA computer code[29]. The elemental metallic ratio, Zr/(Zr+Ti), was also checked by Energy Dispersive X-ray spectroscopy (EDX).

The density, thickness and surface roughness of the films were determined from X-Ray Reflectivity (XRR) measurements using a four-circle XRD 3000 Seifert diffractometer

equipped with a line focus Cu source, a channel cut Ge (220) monochromator and a scintillation detector with a resolution slit of 0.02°. More details may be found in ref[27]. The crystal structure and preferred orientation of as-deposited alloys were determined from x-ray diffraction (XRD) patterns using a D8 Discover Bruker diffractometer and Cu Kα wavelength (1.5418 Å). In order to avoid reflections from the Si substrate, the XRD scans were recorded in the ω-2θ geometry using a 0.5° offset along ω. Since the typical grain mosaic spread was around 15° independently of sputtering conditions, this offset along ω had only minor influence on the maximum diffracted intensity. The peak position, full width at half maximum (FWHM) and integrated intensity were calculated from the fit of the Bragg reflections using Voigt functions, after background subtraction.

The surface morphology of the films was characterized by Atomic Force Microscopy (AFM) using a Multimode Digital Instrument device operating in tapping mode, while film cross-section views were imaged by scanning electron microscopy (SEM) using a JEOL JSM 7000F equipped with a field emission gun.

Table 5: Deposition conditions and characteristics of the $Ti_{1-x}Zr_xN$ films grown by magnetron sputtering.

ZrN fraction, x	Sputtering mode	Power (W)		Working pressure (Pa)	Ar/N$_2$ flow (sccm)	N$_2$ partial pressure (mbar)	RBS			Zr/(Zr+Ti) (%) (EDX)	Growth rate (Å/s)
		Ti target	Zr target				Ti (%)	Zr (%)	N (%)		
0	metallic	300	/	0.19	9.0/0.3	4.5 10^{-5}	50	/	50	0	1.40
0.14	metallic	300	52	0.19	9.0/0.5	3.0 10^{-5}	45.0	7.3	47.6	15	2.02
0.42	metallic	300	154	0.19	9.0/0.9	2.0 10^{-5}	28.2	20.5	51.2	41	3.06
0.68	metallic	195	300	0.19	9.0/1.7	1.8 10^{-5}	16.6	35.9	47.2	68	3.80
1	metallic	/	300	0.19	9.0/0.7	4.0 10^{-5}	/	53.9	45.4	100	2.50

A representative RBS spectrum of a $Ti_{1-x}Zr_xN$ thin film sputter deposited on Si at 0.19 Pa is reported in fig. 4.19. In addition to the Ti, Zr and N elements, a small atomic fraction of Hf (<0.4%) is detected for ZrN-rich alloys. This small contamination in the $Ti_{1-x}Zr_xN$ films comes from the Hf impurity of the Zr target. No O or C contamination was detected in the bulk of the films. The results of the chemical analysis are reported in Table 5.
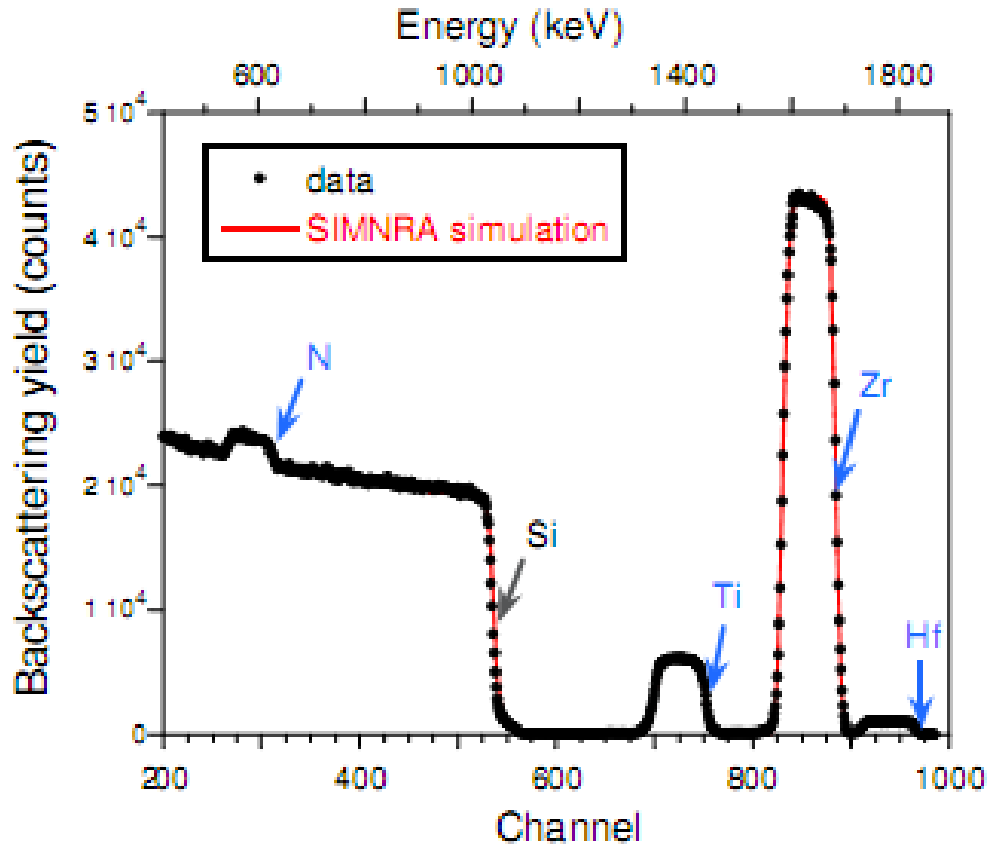
Figure 4.19: Representative RBS spectrum of a Ti$_{1-x}$Zr$_x$N thin film sputter deposited on Si for an incident particles charge of 200 μC.

The atomic fractions of metallic elements determined from RBS were in good agreement with EDX analysis. For all samples, the N atomic fraction was found to be in the range 0.45-0.54 ± 0.05, i.e. stoichiometric nitride films were obtained within the uncertainty limit of the RBS technique.

The evolution of the ω−2θ XRD spectra from 300 nm thick Ti$_{1-x}$Zr$_x$N films, sputtered respectively at 0.19 is shown in fig.4. For Ti$_{1-x}$Zr$_x$N films, a solid solution with rocksalt structure is stabilized in the whole compositional range, as attested by the presence of single reflections located between the TiN and ZrN positions. The TiN films exhibit a clear (111) preferred orientation. For the Ti-Zr-N system, the intensity ratio I$_{111}$/I$_{002}$ increases when Zr atoms substitute for Ti up to x~0.5. Higher Zr contents resulted to a less sharp (111) texture and a peak broadening. For pure ZrN film, the (111) texture coefficient T$_{111}$ is found to be 0.64, close to the value for random orientation (0.47).
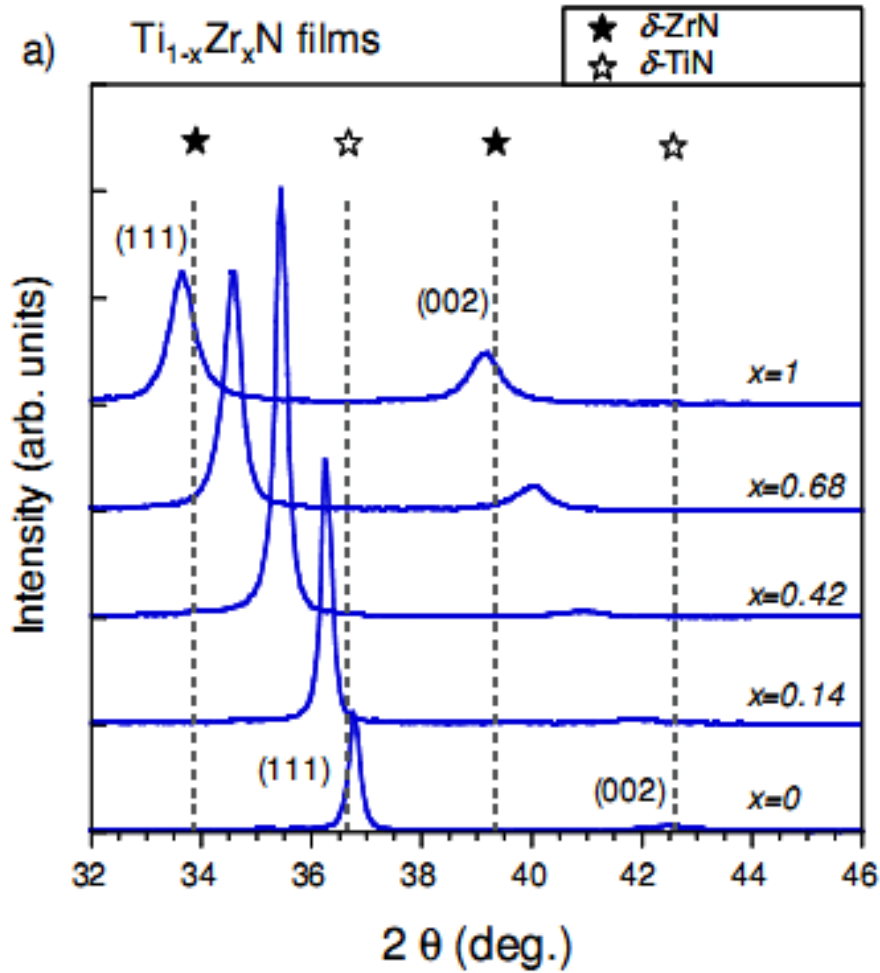
Figure 4.20: Evolution of XRD patterns of ternary $Ti_{1-x}Zr_xN$ films (~300 nm thick) with ZrN fraction x

The lattice parameters, $a_\perp$, calculated from the (111) film peak position, are reported in figure 4.21a for $Ti_{1-x}Zr_xN$ films. A deviation from Vegard's rule is clearly observed for both systems. However, the reported values correspond to data of as-deposited samples and may therefore be strongly affected by the residual stress state.

To derive the contribution of microstrain e and average grain size (or column length) <L> to XRD peak broadening, the use of the Williamson-Hall method was not appropriate since highly textured films were obtained. The peaks profile were rather analyzed using the single-line analysis of de Keijser et al.[30], which consists in determining the Cauchy (βc) and Gaussian (βg) integral breadth of a given Bragg reflection profile fitted using a Voigt function. The results are reported in figure 4.21b and 4.21c. Distinct behavior in the evolution of the average grain size <L> determined from (111)-oriented grains with composition are evidenced. For Ti1-xZrxN films, <L> reaches a maximum at x~0.25 and then gradually decreases with increasing ZrN fraction.
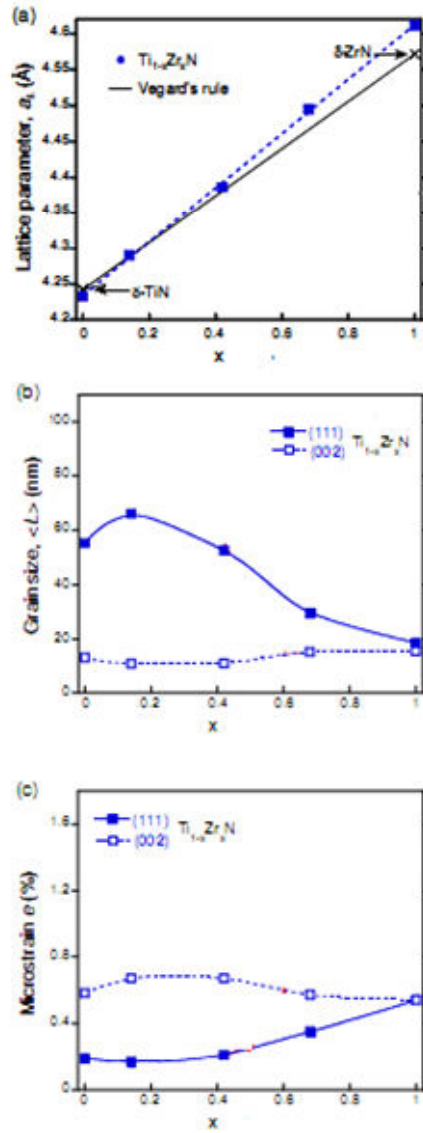
Figure 4.21: Evolution of a) the out-of-plane lattice parameter, $a_\perp$, determined from (111) Bragg reflections, b) vertical grain size, <L>, and c) micro-strain, e, of $Ti_{1-x}Zr_xN$ films as a function x content.

For $Ti_{1-x}Zr_xN$ films, the values of <L> remain in the range 65-20 nm. When two textures coexist, <L> values of (002)-oriented grains are much lower than those of (111)-oriented grains, which support the hypothesis of renucleation. Since the surface energy of (002) planes is lower than that of (111) ones in TMN with rocksalt structure, new grains are expected to grow with their (002) planes parallel to the surface[27]. For the ZrN film, a grain size value of ~18 nm is found for both (111) and (002)-oriented grains, which confirm the almost random polycrystalline microstructure of this sample.

Strong variations in the microstrain values (e varies from 0.15 to 1.20%) are also observed, depending on the film composition and texture (fig. 4.21c), but correlate well with the evolution of the vertical grain size. For TiN-rich films, (111)-oriented grains undergo systematically less microstrain than (002)-ones, which can be easily understood from the

114

preferred growth of (111) columns. When (002) grains form, mostly from renucleation, they store much more elastic energy. With increasing fraction of Zr atoms, more defects are introduced by atomic peening[22], as discussed above, which explains the strong increase in microstrain. Someone can address this increase in microstrain to the size mismatch of Ti and Zr which is quite high but further on we will see that the microstrain is more pronounced in the case of a heavier atom such as Ta which has lower mismatch in size with Ti. This means that distortions are distortions are essentially due to growth-induced defects (related to the larger deposited energy of the heavier Ta sputtered atoms and larger contribution of backscattered Ar).
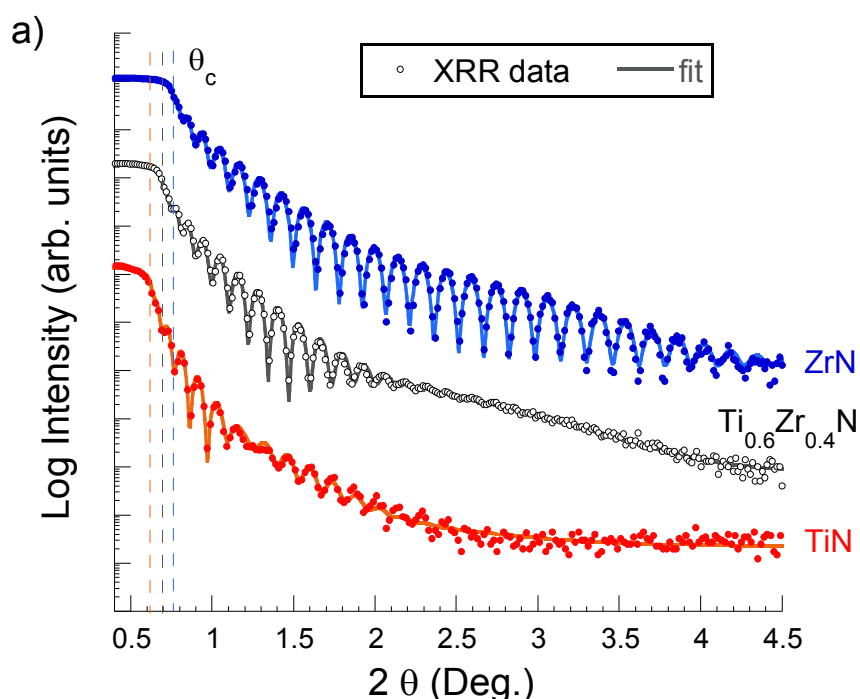
Figure 4.22: Representative XRR spectra of binary TiN, ZrN and Ti$_{1-x}$Zr$_x$N films.

Representative XRR spectra of ~120 nm thick Ti1-xZrxN films are reported in figure 4.22. Kiessig's fringes are clearly observable, indicating relatively low surface roughness. The density of the Ti$_{1-x}$Zr$_x$N ternary nitride films (fig. 4.23) follows a rule of mixture behavior from the binary TiN and ZrN compounds, whose density at 0.19 Pa is close to bulk values within the uncertainty limits. The density value for the TiN compound is lower than the reference bulk because of the columnar microstructure itself; the presence of intercolumnar voids reduces the density and it is also manifested in the presence of tensile strength during growth (as manifested in lower values of $a_\perp$).
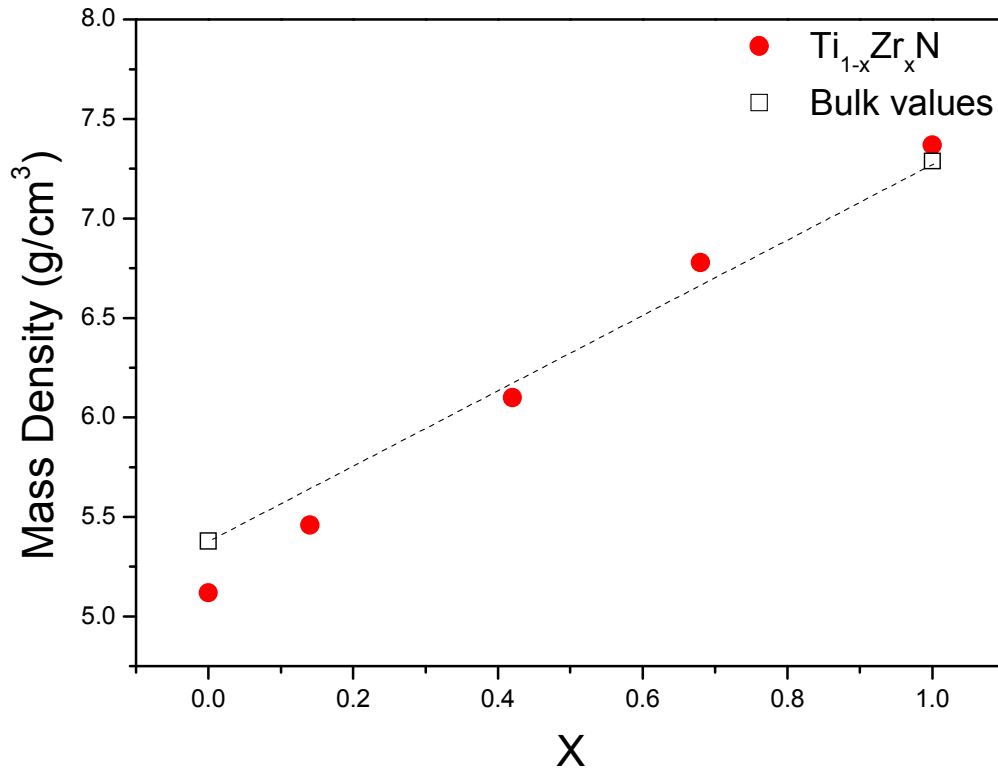
Figure 4.23:) Evolution of density of Ti$_{1-x}$Zr$_x$N films as a function of x content.

On the other end, the ZrN microstructure is overdense, having a "globular" like grains and the value of density is higher than expected. This is also manifested at the values of the lattice constant which are greater than bulk values manifesting a compressive in-plane stress. Additionally the root-mean-square surface roughness of the films is found to decrease with increasing the Zr content (fig. 4.24), which is directly related to the higher adatom mobility pronounced by the heavier Zr atoms.
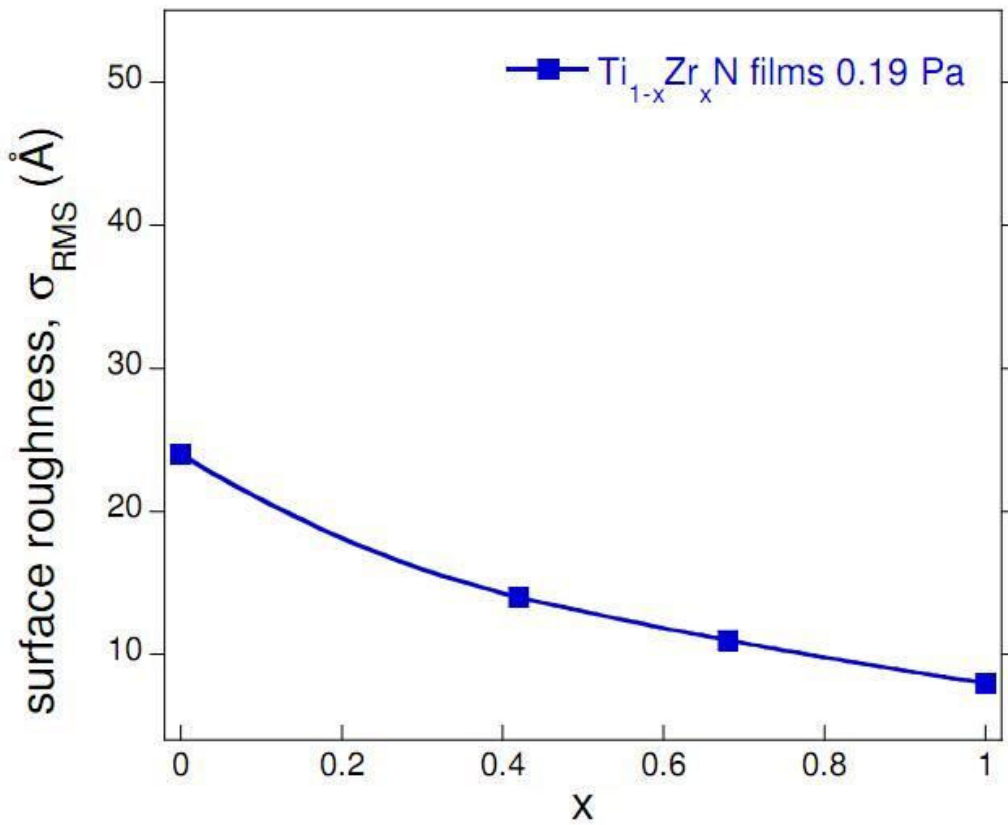
Figure 4.24: Evolution of surface roughness σ_{RMS} of $Ti_{1-x}Zr_xN$ films as a function of x.

4.3.3 Ternary nitrides; Case study TiTaN

In TiZrN the formation of ternary solid solution nitrides was reasonable and expected due to the miscibility in metal phase as well as the same valence configuration. Additionally they share the same crystal structure in the elemental form. But the challenge was to stabilize a ternary nitride from immiscible metals. This is the case of Ti-Ta-N. Ti and Ta have different valence configuration and they are not miscible to each other. Furthermore the crystal structure of TiN and TaN in the bulk is different (δ-TiN rocksalt and ϵ-TaN hexagonal, even though the δ-TaN has also been grown). Also some previous works[31] mentioned that there is limited solubility between TiN and Ta up to 8%. In the following section we investigate the stability of ternary δ-TiTaN using various growth techniques and detailed ab-initio calculations.

Three sets of ternary $Ti_xTa_{1-x}N$ films have been grown on commercial, Czochralski-grown Si(100) substrates. The first set (~300 nm thick) has been deposited by reactive DCMS using two 3'' unbalanced magnetron cathodes (Ti 99.995% purity and Ta 99.998% purity). The deposition occurred in a high-vacuum (HV) chamber (P_b~$2x10^{-6}$ Pa) equipped with three confocal planar magnetron sources. The metallic targets were located at a distance of 18 cm

from the substrate mounted on a rotating sample holder coupled with a heating element. The Ti and Ta target powers were varied in the ranges 150-300 W and 75-152 W, respectively. The Ar/N$_2$ flows were 16/1.3 sccm resulting to a partial pressure of N$_2$ 3-7x10^{-3} Pa as measured by an *in-situ* and *real time* mass spectrometer.

The second set of films (~300 nm thick) has been grown at Room Temperature (RT) by DIBS using a HV (P$_b$~10^{-6} Pa) NORDIKO 3000 system employing a composite target by placing two plates of Ta on top of the circular Ti plate. The typical values employed for depositing the nitride films were U$_p$=1200 V, I$_p$=80 mA and Ar flow rate of 10 sccm for the primary beam, and U$_a$=50 V, I$_a$=40 mA and 2/2 sccm for the Ar/N$_2$ flow rate of the assistance beam, resulting in a total pressure of 0.04 Pa during deposition and growth rate of ~0.045 nm/s.

The PLD experiments of the third set (~200-250 nm thick) were performed in a HV chamber (base pressure P$_b$~5x10^{-6} Pa) at RT using a rotating target of mixed Ti-Ta (purity 99.95% and 99.999% for Ta and Ti, respectively); the fraction of Ti/Ta on the target was varying in order to produce films of varying composition (x). A Nd:YAG laser (2nd harmonic, λ=532 nm, pulse duration 3 ns, pulse energy 200 mJ, repetition rate 10 Hz) was used for the ablation in a flowing N$_2$ (purity 99.999%) ambient (N$_2$ flow 50 sccm, N$_2$ partial pressure 3x10^{-1} Pa) and with a DC bias (V$_b$=-50 V) applied to the rotating substrate during growth. The target to substrate distance was 3.5 cm.

The lattice constants, the crystallographic orientation and texture coefficients have been determined from x-ray diffraction (XRD) patterns recorded on a Bruker D8 diffractometer using Cu K$_\alpha$ radiation and operating in θ–2θ Bragg-Brentano configuration. The pole figures, the stresses of the films and the densities have been determined by X-Ray Reflectivity (XRR) and the crystalline group method[2,6,32], respectively, using a SEIFERT four circle X-ray diffractometer. The composition of the films x was studied Energy-Dispersive X-Rays (EDX) in a JEOL 5600LV scanning electron microscope, while the [Metal]/[N] ratio of the marginal cases of TiN and TaN has been found to be very close to unity using Auger Electron Spectroscopy; thus we assume that this ratio applies for the intermediate Ti$_x$Ta$_{1-x}$N cases, as well. The surface morphology of the films was characterized by Atomic Force Microscopy (AFM) using a Multimode Digital Instruments device operating in tapping mode, while film cross-section views were imaged by scanning electron microscopy (SEM) using a JEOL JSM 7000F equipped with a field emission gun.

The total ground energy, the cell size, and the electron density of states of Ti$_x$Ta$_{1-x}$N have been calculated using the linear augmented plane wave method within the density

functional theory (DFT). The exchange-correlation functional was treated within the generalized gradient approximation (GGA) or the local spin density approximation (LSDA).

The energetics of the incoming particles were estimated using Monte-Carlo simulations based on theory of the interaction of ions with solids, using the SRIM[33] computer code. Calculations were performed for the two metallic targets (Ti and Ta) using 10^7 Ar ions with typical incident energy of 500 eV. The threshold energy for atomic displacement was taken as 30 and 80 eV for the Ti and Ta targets, respectively[34]. The average energy of sputtered atoms, E_{sp}, backscattered neutrals, E_b, as well as the weighted average deposited energy defined as $E_{dep} = (1-\alpha)E_{sp} + \alpha E_b$, where α denotes the ratio of backscattered Ar flux to the sputtered atoms flux in the solid angle ($\Omega = \pm\ 7°$) towards the substrate have been determined.

Figure 4.25 shows the evolution of XRD scans of Ti–Ta–N films with increasing Ta content. It can be seen that the co-sputtering of Ti and Ta under reactive atmosphere results in the formation of B1-structure $Ti_xTa_{1-x}N$ solid solutions. Only the characteristic peaks (111) and (002) from the rocksalt structure are observed and no peaks from pure Ti or Ta nor pure binary TiN and TaN compounds were found. With increasing Ta content, a gradual shift of Bragg peaks towards lower 2θ angles is observed. This can be related to an increase in compressive stress or to a dilatation of the lattice parameter due to the formation of substitutional solid solutions (the TaN lattice is expanded by ~2.3% compared to that of TiN).

In figure 4.26 we can see that the $Ti_xTa_{1-x}N$ system forms a solid solution in the whole range of compositions and the lattice constant resembles the vegard's rule. Also we can notice the mentioned expansion of the lattice constant of the films compared to the bulk values. Independently of the expansion (or the growth technique) the stress can be relieved using post-growth techniques like thermal annealing. We see at the figure 4.26a that the thermal annealing for 3h under vacuum at 850° C, relieves all stresses and the new lattice size is very close to the expected by the vegard's rule.
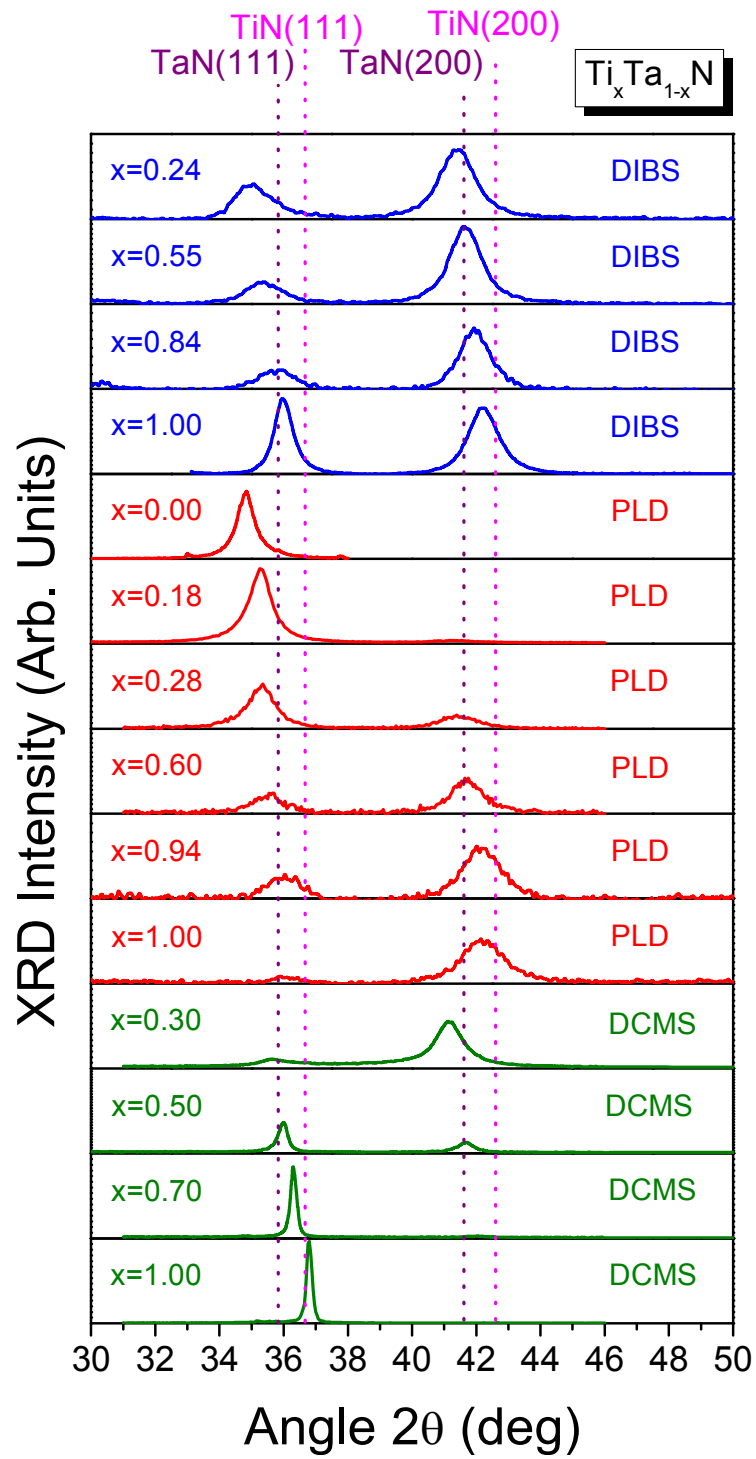
Figure 4.25: (color online) XRD patterns from Ti$_x$Ta$_{(1-x)}$N samples grown by PLD, DIBS and DCMS for various x.
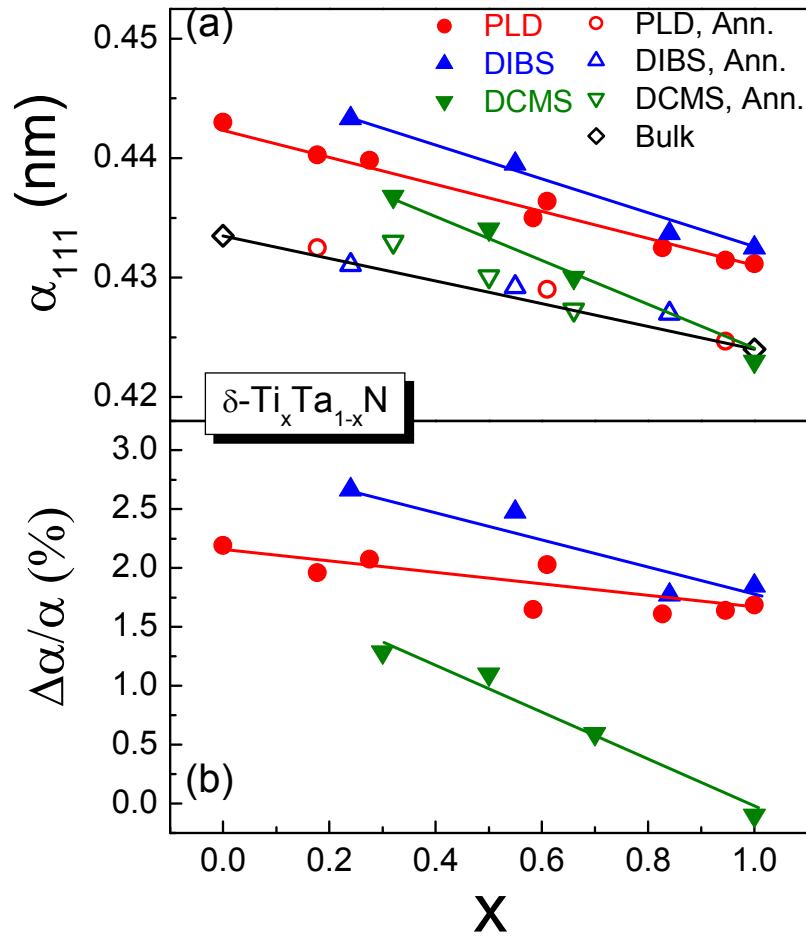
Figure 4.26: a) Lattice constant, and (b) deviation from Vegard's rule vs. x for all the XRD data of this study

In figure 4.26b we have plot the percentage variation from the vegard's rule due to macrostrain, using the bulk values of the nitrides. We can see that the variation can be as high as 3% for the high Ta content sample grown by DIBS. This graph is a direct indicator of the stress induced by the deposition technique. It is obvious that the DIBS technique is producing the most strained samples among the other two. In addition, it seems that the Ta content is affecting the stress state of the films. The stress accumulated mechanism as well as the effect of the Ta addition will be discussed later on, in terms of energetics.

Another feature of the lattice constant of ternary nitrides is the bowing of the lattice constant as a function of composition. In figure 4.27 one can see the stress free lattice constant of various $Ti_{1-x}Ta_xN$ films and the relative bowing (%) of the lattice parameter from Vegard's rule. The value of the lattice constant is the stress free as found from the $\sin^2\psi$ analysis. This implies that the stress induced expansion is not the cause for this behavior. The explanation relies on the bonding of these elements. The different bond length between Ti-N and Ta-N as well as the relative cell size between Ti-N and Ta-N and Ti-Ta is probably the cause for that. The Vegard's rule is based on the linear effect of the solid solution but the real case is not linear. This bowing effect is not a major problem, as a structural parameter,

121

because the deviation is small. But this behavior is observed also in band gap, and this deviation is more critical for the film properties. Hence both effects should be understand and taken into account and the tool on that study is the electronic structure and the bonding of these materials.
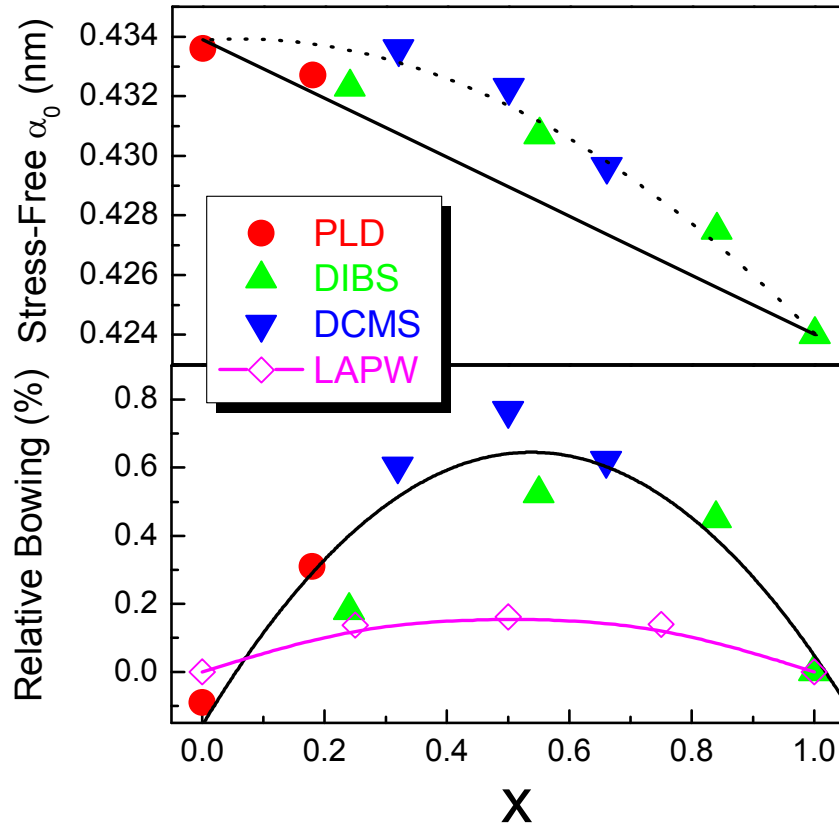
Figure 4.27: The stress free lattice constant of various $Ti_{1-x}Ta_xN$ films and the relative bowing (%) of the lattice parameter from Vegard's rule.

The wide solubility range between TiN and TaN, in contrast to metallic Ti and Ta, can be understood considering the chemical bonding between the metal and N atoms. Ab-initio calculations show that the metallic TaN besides the purely ionic bonding between the Ta ($5d^36s^2$) and N ($2s^22p^3$), presents also covalent-like bonding due to the strongly hybridized energy states around −7 eV of the Ta 5d and N 2p. This mixed bonding competition is clearly manifested in the δ-$Ti_xTa_{1-x}N$ figure 4.28. The TaN features of the N strong s-character, along with the Ta_{dt2g} pronounced lobes that point toward the nearest metal atoms denote σ-bonding and characterize the $Ti_{25}Ta_{75}N(010)$ plane, Figs. 4.28a and 4.28b. The corresponding TiN plane in the case of $Ti_{75}Ta_{25}N$ (010) exhibits more metallic than ionic character ($Ti:3d^24s^2$), Fig. 4.27d. In the $Ti_{25}Ta_{75}N(100)$ plane, N loses its perfect electron saturation regaining charge via π-bonding formation with the Ti_{dt2g} orbitals in the (110) plane, Fig. 4.28a.
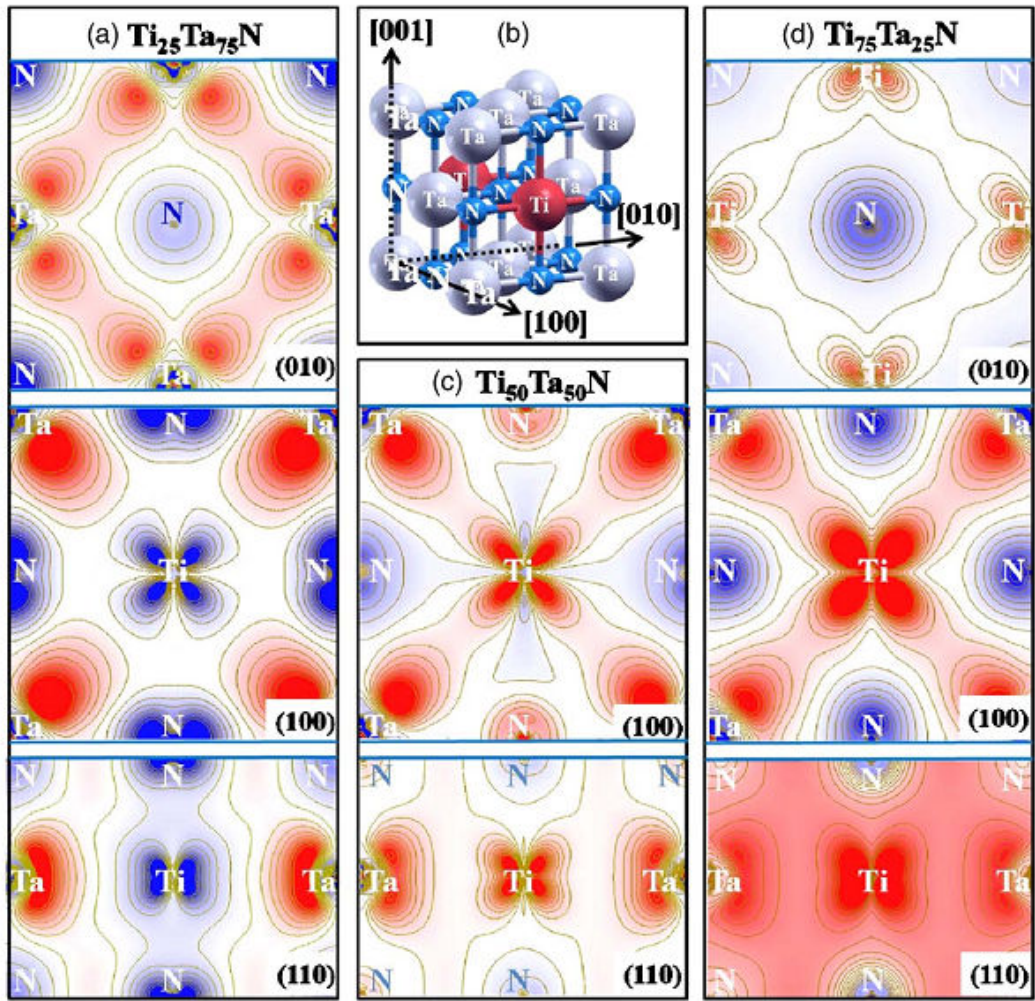
Figure 4.28: Total valence charge density for the (010), (100), and (110) planes. (a) and (b) $Ti_{25}Ta_{75}N$, (c) $Ti_{50}Ta_{50}N$ and (d) $Ti_{25}Ta_{75}N$. Red (blue) indicates positive (negative) values.

As the Ti inclusions increase Figs. 4.27c and 4.27d, the Ti_{dt2g}-Ta_{dt2g} hybridization is more pronounced reaching in the case of $Ti_{75}Ta_{25}N(100)$, the picture of the pure TaN plane of $Ti_{25}Ta_{75}N(010)$, Fig. 4.27α. Finally, the small hybridization of Ta_{dt2g} orbitals with N atoms in the [001] direction of $Ti_{25}Ta_{75}N(110)$ plane, Fig. 4.27a, is enhanced in the $Ti_{50}Ta_{50}N(110)$ and $Ti_{75}Ta_{25}N(110)$ planes, resulting in positive charge of the corresponding N atoms. Thus, the bonding nature of δ-$Ti_xTa_{1-x}N$ is characterized by a mixed covalent-ionic character that coexists with the metallic features. The charge transfer between the cations (Ti,Ta) and the anion (N) increases when the mean metal electronegativity increases, resulting in stronger ionic character for TaN compared to TiN along with stronger covalent bond features.

The next important feature of the ternary compounds is the preferred orientation of the grains. Previous studies [35-37] have examined the texture evolution in binary compounds (mainly focused on TiN) to reveal the dominant mechanisms. The question is how the addition of one more element affects the orientation of the ternary compound.

In our case we have obtained films with single and mixed textures depending on the deposition conditions. The preferred orientation is varying significantly even for films with the same composition. We will try to deconvolute the influence of each parameter (surface energy and diffusion, total energy, ion bombardment, *etc*) involved in grain orientation.

Normally at equilibrium, the system need to go to lowest energy, so the nucleation and coalescence of these materials favours, generally, the {111} oriented grains, because this orientation has the lowest free energy (for the cubic lattices in nitrides). Thus the occurrence of a (002) preferred orientation could be due to the grain growth under non equilibrium conditions. These conditions occur when we have ion bombarbment to the film's surface. In such conditions the {200} planes exhibit lower surface energy, thus they are more favourable to "survive" during coalescence. This is shown in figure 4.29, where is plotted the texture coefficient TC_{111} of $Ti_xTa_{1-x}N$ films, versus x, for the three different deposition techniques.

It is clear that the texture coefficient is dependent on composition for PLD and DCMS but not for DIBS. In DCMS samples (Ti rich) the majority of grains are 111 oriented while in Ta rich the opposite is happening. This is due to the surface bombardment which is creating-destroying nucleation centres (non equilibrium condition). The addition of Ta increases the momentum transfer to the surface since the Ta is much heavier than Ti. In DIBS the bombardment is already very intense and because of that the orientation is almost random and independent of the composition range.

The preferred orientation of the PLD-grown samples is more sensitive to the composition of the films. Thus, Ti-rich samples are textured along the {100} direction (e.g. Fig. 4.29), while Ta-rich samples are textured along the {111} direction. This can be well explained if we consider the ionization potential of Ti and Ta, which is 6.83 and 7.88 eV, respectively. Thus, the multi-photon ionization process during the ablation of the target occurs by 3-photon absorption for Ti and 4-photon absorption for Ta, making the ionization of Ti more probable than for Ta and thus the Ti species are more energetic than Ta resulting to {100} texture in agreement with the proposed texture mechanism for such nitrides.
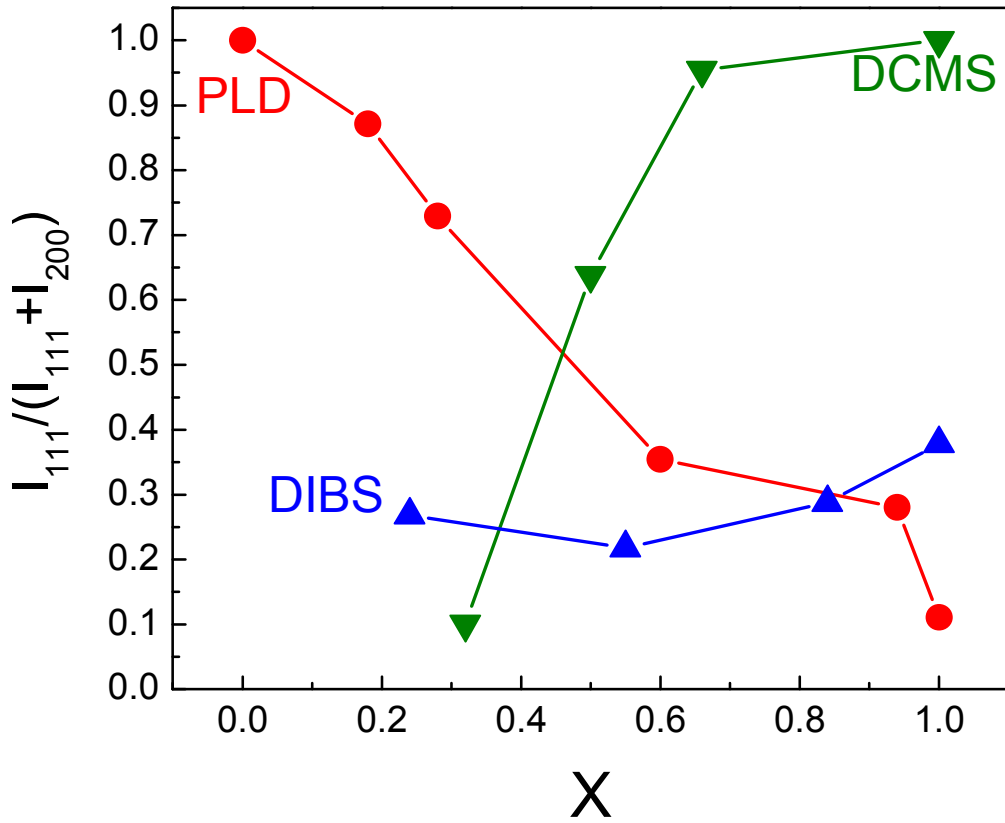
Figure 4.29: Texture Coefficient (TC$_{111}$) vs. Composition.

All the above come in agreement with the backscattered Ar atoms (much higher backscattered intensity for a Ta target than for Ti), which means that the Ta target produces a lot of backscattered Ar atoms. More backscattered Ar atoms means more energy transferred to the film and thus a non equilibrium growth of the grains resulting (100) oriented grains.

We have performed Monte Carlo simulations using the SRIM[38] code, for various target compositions for both sputtering techniques (PLD does not produce backscattered atoms). We calculated the percentage of atoms (backscattered or sputtered) arriving the substrate surface. To have a more precise result, we filtered the results by selecting these particles only going to the substrate (according to our deposition geometry). The results are shown in table 4a, and one can notice that the number of backscattered Ar atoms increases with the Ta content of the target. The median energy of sputtered particles leaving target has increased from 11eV to 15eV while the median kinetic energy of backscattered atoms changed from 140eV to 340eV. If we take account the percentage of the arriving particles we can see that the backscattered atoms deliver a massive amount of energy to the surface of the film, especially for the DIBS technique.

Table 6: SRIM calculations for a)Ion beam sputtering using Ar atoms at 1.2KeV at various target compositions and b) for magnetron sputtering using Ar atoms at 500eV impinging energy for three elemental targets.

a)

Ti$_x$-Ta$_{1-x}$ Target composition	Sputtered (%)	Back Scattered (%)	Mean Energy of Sputtered (eV)	Mean Energy of Back Scattered (eV)	Median Energy of Sputtered (eV)	Median Energy of Back Scattered (eV)
0.00	90.4	9.6	31.6	329.1	15.6	339.5
0.30	90.7	9.3	31.7	281.6	14.0	262.2
0.50	93.5	6.5	28.7	241.6	12.4	199.0
0.70	95.0	5.0	26.2	200.6	11.2	144.7

b)

Element	Sputtered atoms (%)	Backscattered atoms (%)	Average Energy of Sputtered Atoms (eV)	Average Energy of Backscattered atoms (eV)	Deposited Energy (eV)
Ti	0.97	0.03	17	12	17.0
Ta	0.83	0.17	33	110	46.2

Similar results for the DCMS technique are shown in table 4b), where we have co-deposition from two single elemental targets, and the Ta target produces more (than Ti target) BS Ar atoms. In that case we have similar results with lower values of energy, but different ratio of sputtered and backscattered particles, arriving at the surface.

Further evidence on the correlation of the preferred orientation with the bombardment of the surface is the size of the crystallites. In figure 4.30 we present the estimated grain size from the three different PVD techniques. The grain size has been calculated using the single diffraction line analysis proposed by T. de Keijser[30]. That method is based on evaluating independently the Gaussian (related to microstrain) and the Lorentzian (related to grain size) constituents to the total integral width of the diffraction line. One can see that the grain size (for both orientations (111) + (200)) is independent from the composition for the DIBS technique, since the ion bombardment plays the major role and prohibit grains from growth further than few (<10) nm.

On the contrary, the grain size for the PLD grown samples is varying significantly (again for both textures) versus composition, although all the PLD-grown films exhibit similar globular microstructure as revealed by TEM observations. The variation of the grain size might be attributed to the ionization degree of the plume. Thus, in the case of TaN the grain size is higher and that it is related due to the increase of the ion irradiation.

On the other hand the case of DCMS is very distinct, because the variation on the grain size is huge (one order of magnitude) and is a function (for both textures also) of the Ta

content. This difference means that it seems to be an energetic threshold for the development of a texture and another one for the growth of the grains. The DIBS and PLD techniques are above that threshold limit for the grain growth so they don't have any grain growth, while on DCMS the deposition of Ti-rich samples leads to lower energetics and thus larger grains. The control of the final microstructure of the film is very crucial since it affect the majority of the film's properties. The $Ti_xTa_{1-x}N$ films in this study had two different microstructure forms, a columnar and a globular one.
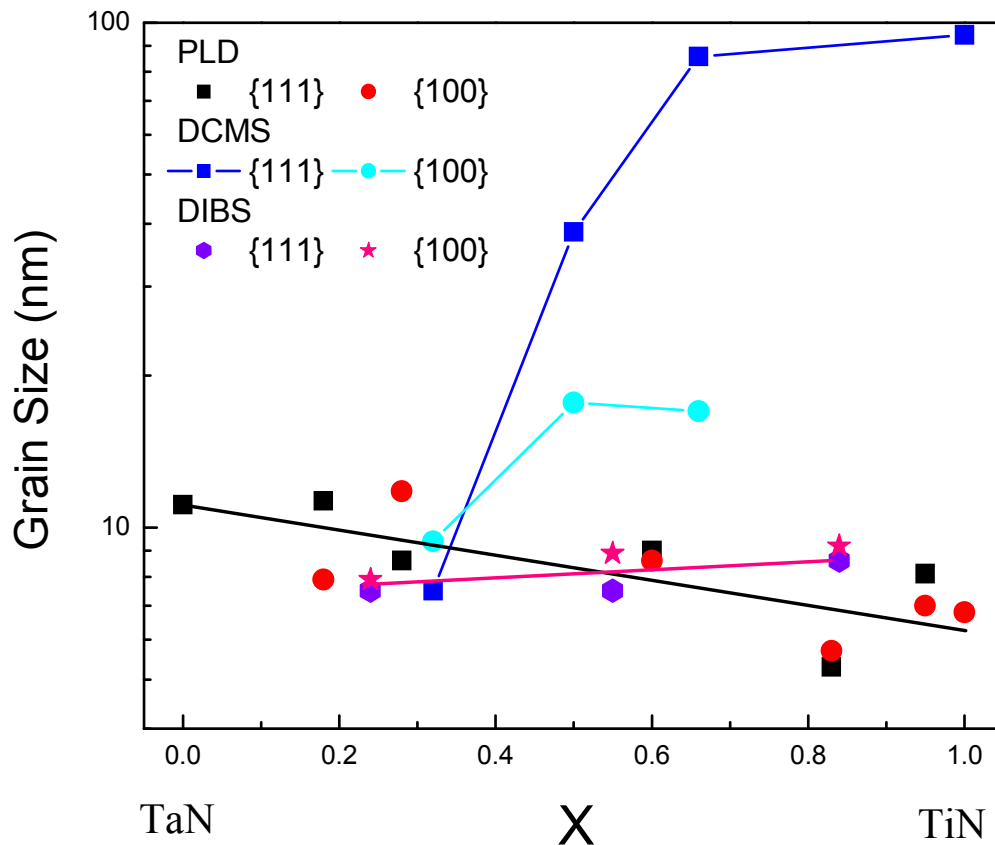
Figure 4.30: Grain size calculated from single line analysis of the XRD peaks.

Depending on the deposition parameters, the microstructure changed from one to another for the same composition of film. This led to a conclusion that chemistry by itself does not play a role on that and it is only a mass-momentum transfer phenomenon. In figure 4.31 we can see the cross section SEM images from laser ablated Ti rich and Ta rich samples. The difference in microstructure is more than obvious. In the Ti-rich sample one can notice the columnar growth of grains and on the Ta-rich case the globular type of growth. To verify stronger the microstructural observations we have performed AFM scans to check the surface topography.
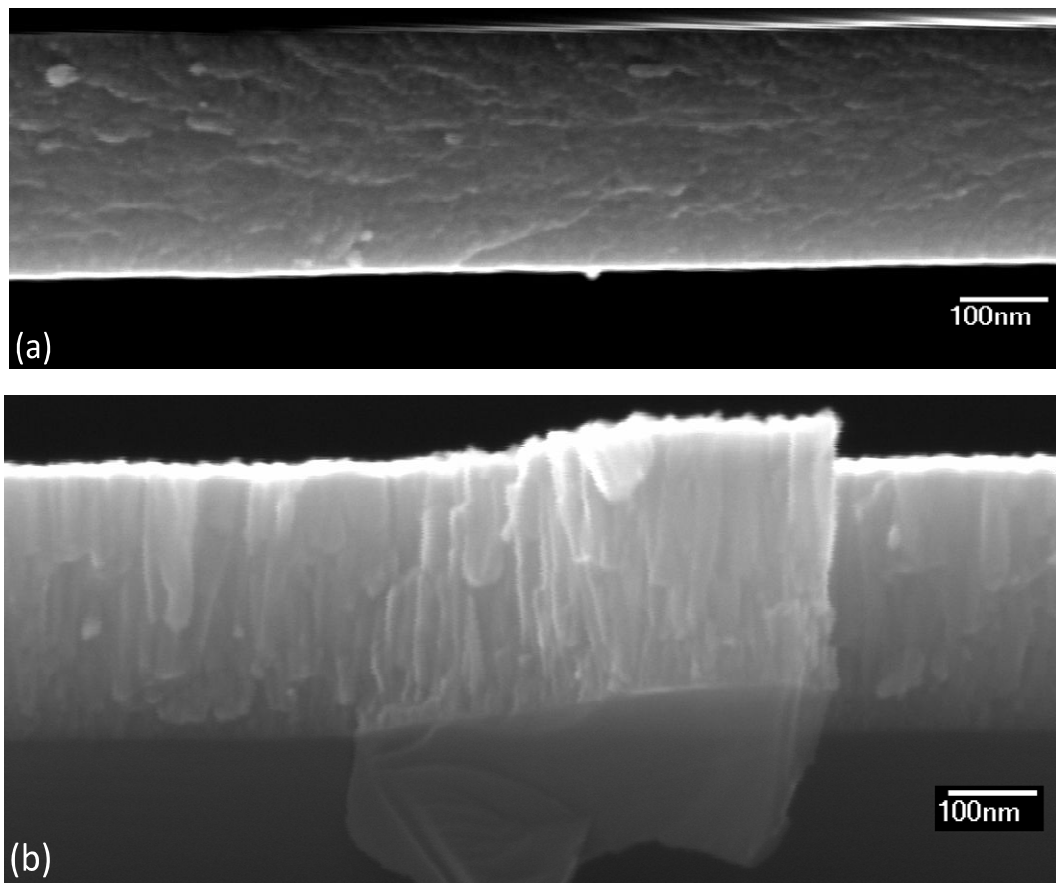
Figure 4.31: Cross section SEM images from a Ta rich (a) and Ti rich (b) Ti$_x$Ta$_{1-x}$N samples.

The AFM images revealed another feature of the different morphology samples, which is the roughness. The samples deposited with lower energetic conditions illustrate more roughness since the diffusion is limited inside grains and also because the growth in [111] direction is creating sharp triangular facets. The three fold symmetry of the planes-facets can be seen clearly in the AFM images. The other case is the Ta rich sample where the roughness is very low due to the low grain size and the continuous bombardment which results in local annealing due to collisions and finally a very smooth surface. The intermediate samples have a mixed topography changing from the columnar to globular.
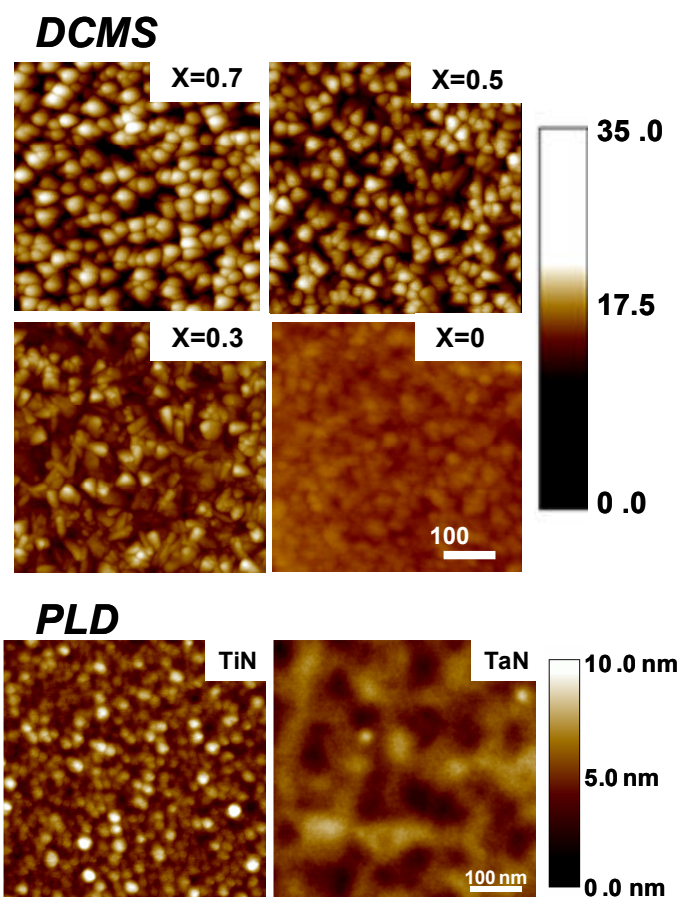
Figure 4.32: AFM images of DCMS and PLD grown $Ti_xTa_{1-x}N$ samples.

4.3.4 Other ternary TMN

To strengthen the previous results about the structure and stability we have grown additionally $Ti_xMe_{1-x}N$ as well as $Ta_xMe_{1-x}N$ (Me: Hf, Nb, Mo and W) over the whole range of x (0<x<1). We studied the stability of the rocksalt structure in all these films and we investigated the validity of Vegard's rule.

$Ti_xMe_{1-x}N$ as well as $Ta_xMe_{1-x}N$ films 200-300nm thick were grown by on Si{001} by reactive Pulsed Laser Deposition (PLD) in the same conditions as the previous depositions to ensure that validity of the results. The composition of the films was determined by in-situ Auger Electron Spectroscopy (AES) and by Energy Dispersive X-rays (EDX). The crystal structure was investigated by θ-2θ X-Ray Diffraction (XRD) in Bragg-Brentano geometry using the CuKα monochromatized line.

The XRD patterns exhibited exclusively the characteristic (111) and (200) peaks of the rocksalt structure for all cases without any fine structure, indicating perfect solid solutions over the full range of x (0<x<1) for all cases, demonstrating the general property of TiN and TaN being fully miscible in every MeN of rocksalt structure, independently of the phase

diagram of the constituent metals. The bonding of the metal's d valence electrons with the nitrogen's p electrons makes possible the formation of any rocksalt ternary nitride of the group IVb-VIb metals regardless the valence electron configuration.

The cell sizes (α_{111}) were calculated from the (111) interplanar spacings and are displayed in figure 4.33. The a_{111} vs. the composition x for a very wide variety of $Ti_xMe_{1-x}N$ and $Ta_xMe_{1-x}N$ (Me=Ti, Zr, Hf, Nb, Ta, Mo, W) follow distinct lines resembling (but not coinciding) Vegard's rule. In all cases, presented in figure 4.33, the lattice constant is expanded compared to the expected values from Vegard's rule; this is exclusively due to in-plane compressive stresses, which are relieved after vacuum annealing, as already explained previously.
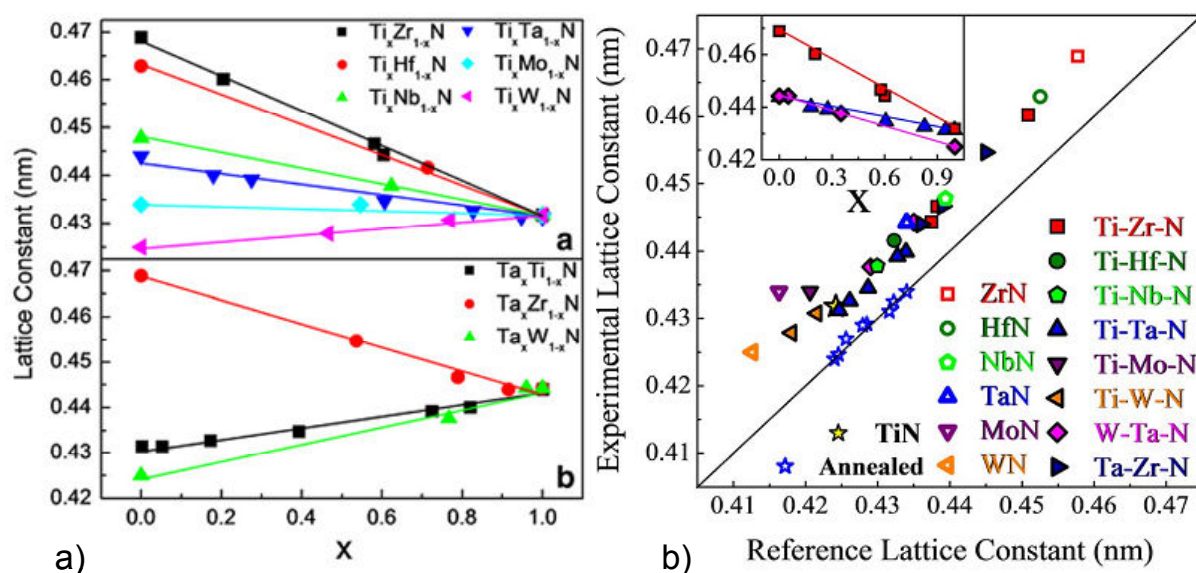
Figure 4.33: a) Lattice size of $Ti_xMe_{1-x}N$ and $Ta_xMe_{1-x}N$ (Me=Ti, Zr, Hf, Nb, Ta, Mo, W) as a function of composition x and b) Comparison of the experimental lattice constants with those expected from Vegard's rule. Inset: Correlations of the lattice constant with the film composition for the systems $Ti_xZr_{1-x}N$, $Ti_xTa_{1-x}N$ and $W_xTa_{1-x}N$.

4.4 Conclusions

Within the present chapter, we presented a comparative study of a very wide range of ternary transition metal nitrides of the form: $Ti_xMe_{1-x}N$ and $Ta_xMe_{1-x}N$ (Me=Ti, Zr, Hf, Nb, Ta, Mo, W), for (0<x<1), grown by three deposition techniques; Pulsed Laser Deposition (PLD), Dual Ion Beam Sputtering and Dual Cathode Magnetron Sputtering (DCMS). Based on results on binary nitrides also presented here (TaN and ZrN), we studied experimentally and theoretically the stability of the rocksalt structure in all these ternary films and we map their lattice constants. We gave special emphasis to $Ti_xZr_{1-x}N$ and $Ti_xTa_{1-x}N$ as representative ternary nitride cases where the two metals do or do not share the same valence electron

configuration, respectively. We considered the electron hybridizations and the bond nature of the ternary nitrides based on the *abinitio* calculation results. We investigated the validity of Vegard's rule and the effect of growth-dependent stresses to the lattice constant. We clarified the major mechanisms affecting the texture and the microstructure of the films as well as defined the contribution to stress evolution of the microstructure.

References

1   H. Bing-Hwai, Journal of Physics D: Applied Physics **34,** 2469 (2001).
2   G. Abadias, Surface and Coatings Technology **202,** 2223-2235 (2008).
3   G. Abadias and Y. Y. Tse, Journal of Applied Physics **95,** 2414-2428 (2004).
4   I. C. Noyan and J. B. Cohen, *Residual Stress, Measurement by Diffraction and Interpretation* (Springer, New York, 1987).
5   U. Welzel, J. Ligot, P. Lamparter, A. C. Vermeulen, and E. J. Mittemeijer, Journal of Applied Crystallography **38,** 1-29 (2005).
6   U. Welzel and E. J. Mittemeijer, Zeitschrift fur Kristallographie **222,** 160-173 (2007).
7   G. Cornella, S. H. Lee, W. D. Nix, and J. C. Bravman, Applied Physics Letters **71,** 2949-2951 (1997).
8   C. S. Shin, D. Gall, Y. W. Kim, P. Desjardins, I. Petrov, J. E. Greene, M. OdΓ©n, and L. Hultman, Journal of Applied Physics **90,** 2879-2885 (2001).
9   C. S. Shin, D. Gall, Y. W. Kim, N. Hellgren, I. Petrov, and J. E. Greene, Journal of Applied Physics **92,** 5084 (2002).
10 C. S. Shin, Y. W. Kim, N. Hellgren, D. Gall, I. Petrov, and J. E. Greene, Journal of Vacuum Science and Technology A: Vacuum, Surfaces and Films **20,** 2007-2017 (2002).
11 H. Wang, A. Tiwari, A. Kvit, X. Zhang, and J. Narayan, Applied Physics Letters **80,** 2323 (2002).
12 L. G. Parratt, Physical Review **95,** 359-369 (1954).
13 P. Patsalas and S. Logothetidis, Journal of Applied Physics **90,** 4725-4734 (2001).
14 S. Mahieu, P. Ghekiere, G. De Winter, R. De Gryse, D. Depla, G. Van Tendeloo, and O. I. Lebedev, Surface and Coatings Technology **200,** 2764-2768 (2006).
15 G. Abadias, L. E. Koutsokeras, P. Guerin, and P. Patsalas, Thin Solid Films **518,** 1532-1537 (2009).
16 S. Mahieu, P. Ghekiere, D. Depla, and R. De Gryse, Thin Solid Films **515,** 1229-1249 (2006).
17 I. Petrov, P. B. Barna, L. Hultman, and J. E. Greene, Journal of Vacuum Science & Technology A: Vacuum, Surfaces, and Films **21,** S117-S128 (2003).
18 G. Abadias and G. Ph, Applied Physics Letters **93,** 111908 (2008).
19 W. S. Richard and J. S. David, Journal of Applied Physics **79,** 1448-1457 (1996).
20 J. A. Thornton, in *Proceedings of SPIE - The International Society for Optical Engineering*; *Vol. 821* (1988), p. 95-103.
21 A. Anders, Thin Solid Films **518,** 4087-4090.
22 F. M. D'Heurle, Metallurgical and Materials Transactions B **1,** 725-732 (1970).
23 W. D. Nix and B. M. Clemens, Journal of Materials Research **14,** 3467-3473 (1999).
24 S. Nagao, K. Nordlund, and R. Nowak, Physical Review B **73,** 144113 (2006).
25 J. Adachi, K. Kurosaki, M. Uno, and S. Yamanaka, Journal of Alloys and Compounds **396,** 260-263 (2005).
26 R. Hull, *Properties of crystalline silicon* (INSPEC, London, 1999).
27 G. Abadias, Y. Y. Tse, P. GuΓ©rin, and V. Pelosin, Journal of Applied Physics **99** (2006).
28 E. Chason, B. W. Sheldon, L. B. Freund, J. A. Floro, and S. J. Hearne, Physical Review Letters **88,** 156103 (2002).
29 M. Mayer, SIMNRA User's Guide, Report IPP 9/113 (1997).
30 T. H. de Keijser, J. I. Langford, E. J. Mittemeijer, and A. B. P. Vogels, Journal of Applied Crystallography **15,** 308-314 (1982).
31 O. Bourbia, S. Achour, N. Tabet, M. Parlinska, and A. Harabi, Thin Solid Films **515,** 6758-6764 (2007).

[32] B. M. Clemens and J. A. Bain, MRS Bulletin **17,** 46 (July 1992).

[33] J. F. Ziegler, J. P. Biersack, and U. Littmark, The Stopping and Range of Ions in Solids (1985).

[34] P. Lucasson, Proceedings of International Conference at Gatlinburg**,** 42 (1975).

[35] P. Patsalas, C. Gravalidis, and S. Logothetidis, Journal of Applied Physics **96,** 6234-6235 (2004).

[36] J. E. Sundgren, Thin Solid Films **128,** 21-44 (1985).

[37] U. C. Oh and J. H. Je, Journal of Applied Physics **74,** 1692-1696 (1993).

[38] J. F. Ziegler, J. P. Biersack, and U. Littmark, *The Stopping and Range of Ions in Solids* (Pergamon, New York, 1985).

CHAPTER 5

ELECTRONIC STRUCTURE AND OPTICAL PROPERTIES

5.1 Introduction

This chapter is about the optical properties of the transition metal nitrides. The optical properties are the interactions of the material with the electromagnetic spectrum. The range we are interested in is the range of the visible light and the UV (1.5 to 5.5 eV). The electrons which are responsible for these interactions are the valence electrons of the material and thus the electrons occupying the d-shell of the transition metals. The electronic structure of the d electrons in these materials is responsible for the optical properties of the material as well as for the bonding.

We need to investigate the electronic structure to define the electronic transitions and vise-versa. The investigation of the electronic structure is mainly performed by *ab initio* calculations in the framework of DFT and the study of optical properties is done though spectroscopic ellipsometry and optical reflectance spectroscopy.

The *ab initio* calculations through the Density of States (DOS), provide an insight of the population of states, revealing the electrons participating in bonding; and valence charge density plots, expose the directionality of orbitals in space. The transitions of electrons are present in the measured dielectric spectra of the material granting a full description about optical properties.

Summarizing, this chapter starts with a short introduction about the crystal field theory which describes the behavior of the d orbitals in compounds such as the nitrides. Further on, results are presented about the optical properties of a binary system (TaN) and the afterwards results on a ternary system $Ti_xTa_{1-x}N$. The final section of the chapter maps a vast area of binary and ternary nitrides in terms on electronic structure and optical properties.

5.1.1 Crystal field theory

Crystal Field Theory (CFT) is a model that describes the electronic structure of transition metal compounds. CFT can successfully describe the magnetic and optical properties of the compounds. The compound in this case is the transition metal surrounded by 8 atoms of nitrogen. The nitrogen atoms bound electrons from the metal to form bonds and appear to have negative charge. This electric field imposed by the negative ions (ligands) surrounding the metal is changing the d orbitals' energy splitting them into two groups e_g and t_{2g}. The d-orbitals which point directly to the ligands are affected most and these orbitals are elevated in energy (e_g). These orbitals are the d_{z^2} and $d_{x^2-y^2}$ as shown in figure 5.1.
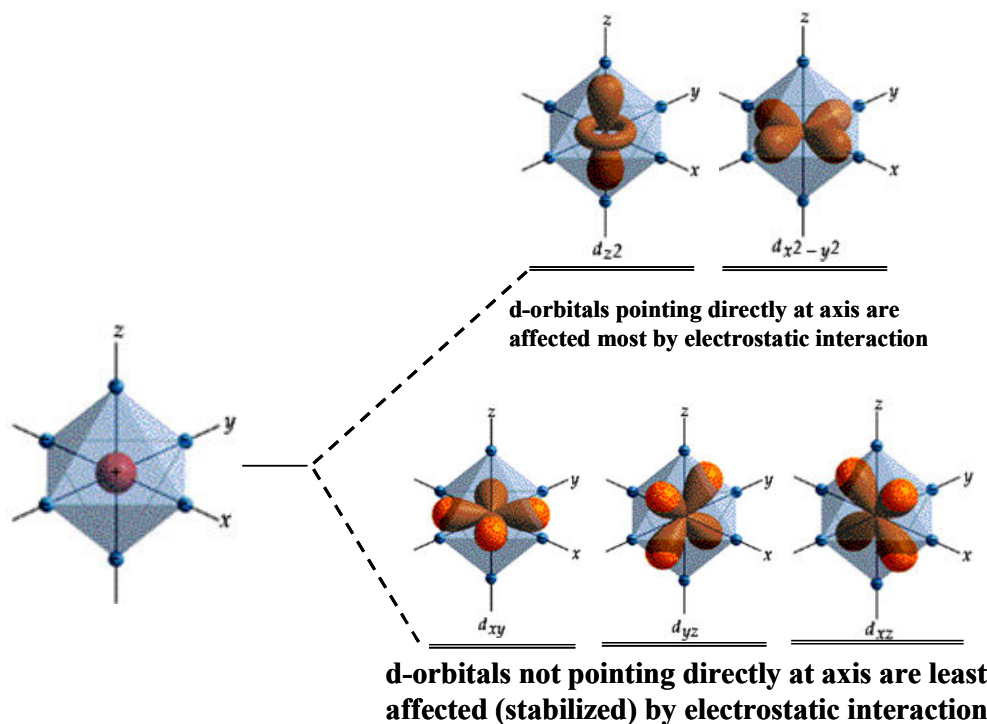
Figure 5.1: The splitting of d orbitals in the presence of 6 ligands (in octahedral points) around a transition metal. The higher orbitals in energy are the e_g and the three remaing are the t_{2g}.

The orbitals which are not point directly to the ligands are the d_{xy}, d_{yz} and d_{zx} and these orbitals are affected less from the surrounding ligands thus being lower in energy.

The energy required by an electron to transit from t_{2g} states to e_g depends on the system and in the case of nitride compounds is around 2 eVs and lies within the visible range. This transition is manifested in the experimental optical measurements further on this chapter.

5.1.2 Electron Density Of States (EDOS)

Another tool complementary to the CFT is the Electron Density Of States (EDOS) which is calculated for a given system and provides information about the population of states as a function of energy in a given system. This information can provide an insight of the electronic structure of a material explaining transitions being observed in the experimental measurements as well as describe the type of bonding between the atoms of a compound (nitride). In general, an EDOS is calculated by finding the available states per unit volume per unit energy of a system. The first step is to calculate all the available states in k space, where k is the wavevector and after that, throught calculations between energy-moment relations, the EDOS is derived in terms of energy.

In compounds such as nitrides, the EDOS structure can indicate possible hybridizations between the energy states of selective orbitals at a specific energy and therefore

give information about the type of bonding. In case of ternary nitrides where there is another metal present the partial electronic density of *d*-electrons is more complicated and the correlation between the stoichiometry is obvious.

The tool which provides information about the directionality and the charge distribution of the electronic structure is the valence charge density plots. In such type of plots, the variations of charge density in a given plane can show or not directionality, revealing the character of the bond.

5.2 Optical properties of δ-TaN

In this section we study in detail the optical properties of highly textured polycrystalline δ-TaN films grown by reactive pulsed laser deposition (PLD) on Si (100). Our experimental results are supported by detailed ab initio calculations within the density functional theory (DFT). Additionally we also report the experimental dielectric function spectra of pure, well characterized, fully dense crystalline and stoichiometric δ-TaN films in a wide spectral range (1.3–5.9 eV) as well as the calculated dielectric function spectra of single-crystal δ-TaN in the 0.5–25 eV spectral range.

The EDOS of δ-TaN have been calculated using the linear augmented plane wave method (LAPW[1,2]) within the DFT using the WIEN2K[3] software. The LAPW method expands the Kohn–Sham in atomiclike orbitals inside the atomic [muffin tin (MT)] spheres and plane waves in the interstitial region. The MT radii were taken 2.0 and 1.8 a.u for the Ta and the N atoms, respectively. Two calculations have been performed with the exchange-correlation functional being treated either using the generalized gradient approximation[2,4] (GGA) in the form given by Perdew, Burke, and Ernzerhof (PBE96) or the local spin density approximation (LSDA)[5].

The joined density of states (JDOS) has been also calculated from the EDOS. JDOS was used[6] to determine the spectral dependence of the imaginary part of the dielectric function ε_2. Then, the spectral dependence of the real part of the dielectric function ε_1 has been calculated by Kramers–Kronig integration.

138
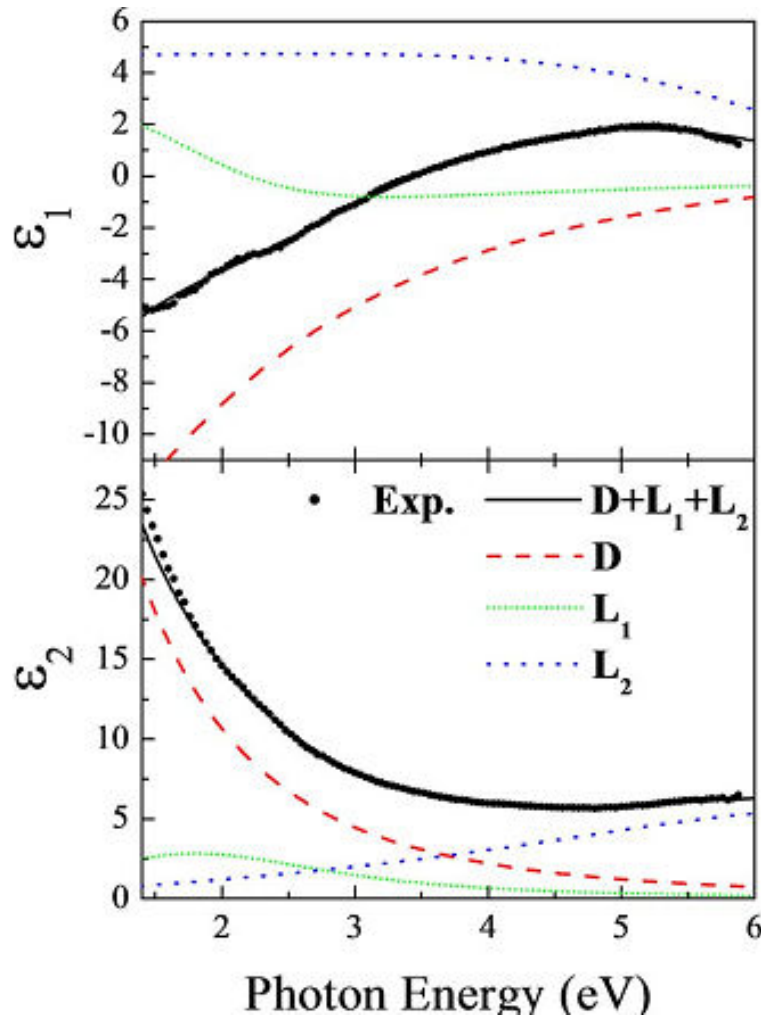
Figure 5.2: The experimental (solid circles) and the fitted (solid line) real (ε₁) and the imaginary (ε₂) parts of the dielectric function of a δ-TaN film. The individual contributions of the Drude (D) term and the two Lorentz oscillators (L₁, L₂) are also presented.

The dielectric function spectra of textured, dense δ-TaN acquired by rotating polarizer ellipsometry are shown in figure 5.2 (solid circles). The optical behavior of δ-TaN is that of a typical conductor exhibiting a strong Drude behavior resembling TiN. Since the studied δ-TaN films are thicker than 300 nm, SE provides directly the complex dielectric function $\varepsilon(\omega)$ of the bulk film without any contribution from the Si substrate. The experimental spectral dependence of the complex dielectric function $\varepsilon(\omega)$ was fitted by a Drude term and two Lorentz oscillators[7-9] that correspond to the intraband absorption and the interband transitions, respectively,

$$\varepsilon(\omega) = \varepsilon_{\infty} - \frac{\omega_{pu}^2}{\omega^2 - i \cdot \Gamma_D \cdot \omega} + \sum_{j=1}^{2} \frac{f_j \cdot \omega_{oj}^2}{\omega_{oj}^2 - \omega^2 + i \cdot \gamma_j \cdot \omega} , \qquad (5.1)$$

139

Where ε_{∞} is a background constant larger than unity and is due to the contribution of the higher-energy transitions that are not taken into account by the two Lorentz terms. Each of the Lorentz oscillators is located at an energy position $\hbar\omega_{oj}$, with strength f_j, and damping (broadening) factor γ_j. More details about the optical model are presented in appendix II.

In Fig. 5.2 the results of the fitting with the above model are shown for a δ-TaN representative film, along with the individual contributions of (i) the Drude term (dashed lines) describing the optical response of the Ta 5d conduction electrons and (ii) the two Lorentz oscillators located at 1.9 eV (short dotted lines) and 7.3 eV (dotted lines). It has to be noted that fits of equivalent qualities can be obtained with the positions of the two oscillators varying from the reported values by ±0.3 and ±0.5 eV, respectively.

The Drude plasma energy E_{pu} has been determined to be 9.15 eV, which is higher than other reported values for TaN, indicating a higher conduction electron density; this is most likely because PLD produces films with lower defect densities than sputter deposition processes.

The actual spectral location of the two Lorentz oscillators suffers from the relatively high estimated errors. Nevertheless, there are two distinct reasons justifying both cases. The later oscillator is located beyond the experimental spectral range and only its low-energy tail contributes to the experimental spectrum and consequently to the corresponding fitting. The former oscillator is very weak and it overlaps with the strong Drude term. This oscillator is actually a secondary term of non-Drude intraband absorption due to non-parabolic structure of the Ta 5d band (Drude's model applies exclusively for parabolic bands). We address this issue with the following reasoning.

The assignment of the absorption bands of δ-TaN determined by SE analysis using the D2L model, is based on detailed band structure calculations. Figure 5.3a) depicts the total, the atomic, and the l-projected (s , p, d electrons) calculated EDOS for Ta and N. We distinguish three energy regions: a) from −20 to −14 eV, b) from −12 to −4 eV, and c) from −4 to 4 eV.

The first region is mainly due to N s-electron contributions while the participation of Ta p electrons is of less importance. The second region is characterized by the strong hybridization of the Ta d electrons with the N p electrons. The third region reveals the origin of the metallic character of the material; in particular the majority of the conduction electrons originate predominantly from the Ta d-t_{2g} states[10] that intercept the Fermi level (located at zero energy and indicated by the vertical dotted line). The E_{pu} is also calculated from the total EDOS at the Fermi level to be E_{pu} =9.7 eV.
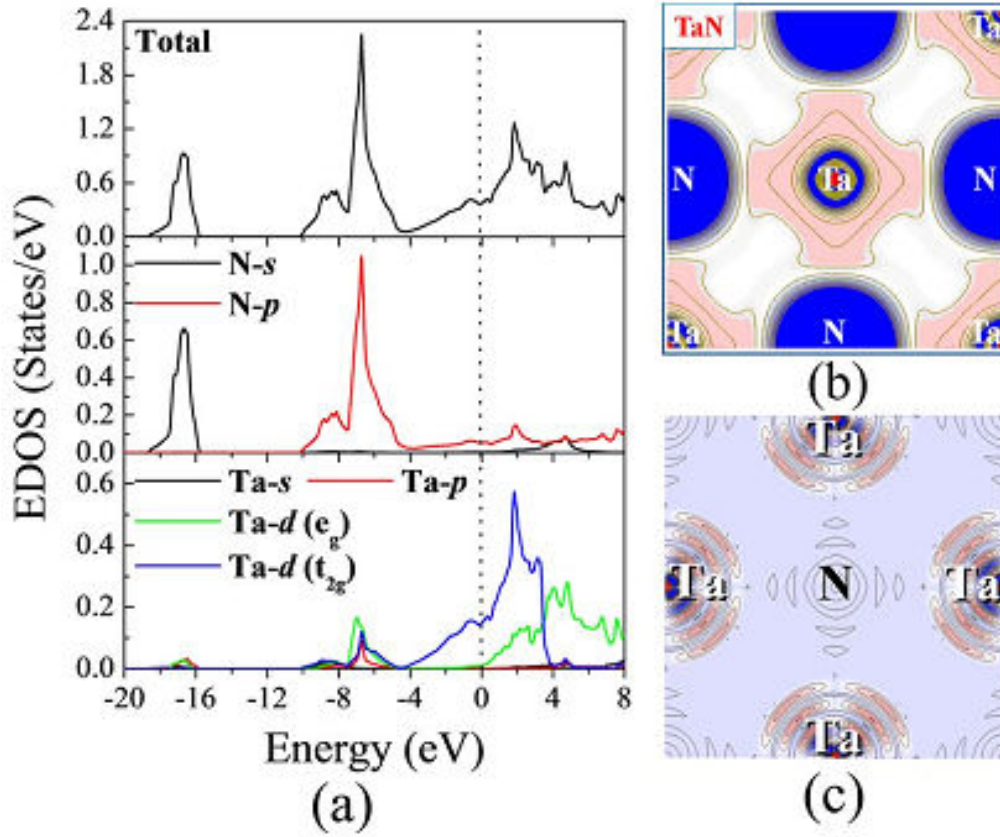
Figure 5.3: a) EDOS for δ-TaN; the electrical conductivity originates predominantly from the Ta-(dt$_{2g}$) band that intercepts the Fermi level (vertical dotted line). b) Total valence charge density of δ-TaN. Blue to red color transition indicates increase of charge values. c) The wave functions of electrons at the Γ-k point and in the second energy region, where the N p-Ta d bonds take place.

The occupied electronic states close to the Fermi level, as well as the unoccupied states (above the Fermi level), govern the optical properties of δ-TaN through the JDOS. The unoccupied states are predominantly due to Ta 5d electrons; the t$_{2g}$ band intercepts the Fermi level, thus being the source of intraband absorption, while the eg band is mainly located above the Fermi level. The observed interband transition (second Lorentz oscillator in Fig. 5.2) can originate from the band lying 6.75 eV below the Fermi level, which is predominantly due to N 2p electrons. A N p→Ta d transition is in accordance with the selection rules for photonic excitation $\left(\Delta l = 0, \pm 1\right)$ and the spectral separation between the N 2p band and the Fermi level (6.75 eV) and it is in good agreement with the experiment (7.3±0.5 eV), especially if we take into account the error in the spectral position of the second Lorentz oscillator and the assumptions of the DFT calculations.

In figure 5.3b we show the total valence charge density map for the (001) plane, from which we can deduce that the idealized picture according to which one assumes purely ionic

bonding between the cations Ta^{5+} and anions N^{3-} without hybridization, is not predicted by our calculations. Indeed, as we can see in figure 5.3b there is a clear charge distribution along the [100] and [010], indicating that the metallic TaN exhibits also covalentlike bonding. This is due to the strongly hybridized energy states in the second region around −5 eV (at the Γ-k point) of the Ta 5d and N 2p electrons, as shown in figures 5.3a and 5.3c, which is in agreement with previous calculations[1]. The partial ionic character in the bonding of δ-TaN gives rise to the crystal field splitting[10] of the Ta 5d band to the t_{2g} and eg bands. The consequence of this is a nonparabolic conduction band [see total EDOS compared to the almost parabolic t_{2g} band around the Fermi level in Fig. 5.3a]. Summarizing, the Drude term in the D2L model describes the intraband Ta 5d-t_{2g} absorption, while the first Lorentz oscillator (at 1.9 eV) describes the deviation of the intraband (intra-d) absorption from the ideal Drude description due to the transitions from the t_{2g} occupied states to e_g unoccupied states due to crystal field splitting.
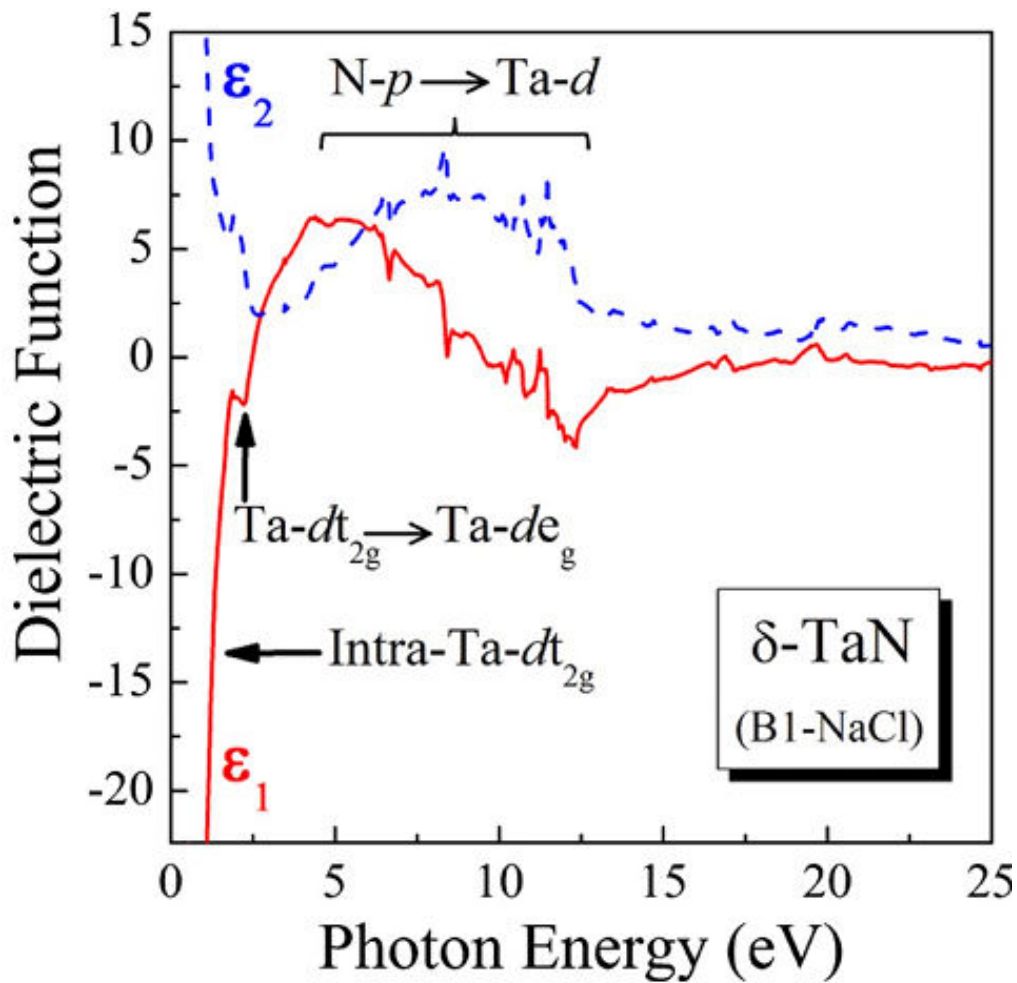

Figure 5.4: Dielectric function spectra (real ε_1 and imaginary ε_2) calculated from the JDOS and Kramers-Kronig integration for δ-TaN. The black arrows indicate the assignment of the peaks.

These considerations and the assignment of the absorption bands are depicted in figure 5.4, which shows the calculated dielectric function spectra of δ-TaN (B1-NaCl). The ε_2 spectrum has been calculated from the JDOS determined by DFT while the ε_1 was calculated from ε_2 using Kramers–Kronig integration[9].

The computational results are in qualitative agreement with the experiment in the 0–6 eV range (figure 5.5), reproducing the main features of the experimental spectra. In addition, the computational ε_1, ε_2 spectra have been calculated for fully dense, single-crystal δ-TaN at 0 K; therefore, the absorption peaks are sharper and better defined than in the experimental spectra. The sharp Drude term has less overlap with the $t_{2g} \to e_g$ transition revealing clearly the presence of the later transition around 2 eV (a spectral position which is in agreement with the prediction of crystal field theory for d^3 transition metals).

The predominant difference between the computational and experimental dielectric function spectra is about the Drude damping factor Γ_D, i.e., the calculated spectra exhibit sharper intraband absorption. This is very reasonable if we take into account that the experimental results concern textured polycrystalline films measured at RT, while the computations have been performed for a perfect single crystal at 0 K. The Γ_D^{poly} factor (which is the inverse of the conduction electron relaxation time) for polycrystalline materials is much larger than Γ_D^{bulk} for single crystals and it is determined by the Fermi velocity u_f and the mean grain size G

$$\Gamma_D^{poly} = \Gamma_D^{bulk} + \frac{u_F}{G}, \quad \Gamma_D^{poly} \gg \Gamma_D^{bulk} \tag{5.2}$$

Based on the D2L model and above equation we calculated a series of dielectric function spectra at the spectral region of strong intraband absorption. The experimental spectra in Fig. 5.5 were best fitted by Γ_D^{poly} =2.1 eV. Then, keeping the rest of the parameters of D2L model fixed, we calculated the dielectric functions of hypothetical δ-TaN samples of varying Γ_D^{poly}, which correspond to varying grain size according to equation 4. Indeed, the inset in figure 5.4 shows the variations in ε_2 with changing Γ_D^{poly} from 2.1 eV (the experimental case) to 0.13eV. Following this analysis the Γ_D^{bulk} is estimated to be 0.19eV (the corresponding line is not shown in the inset of Fig. 5.4 because it coincides with a major extent with the DFT line). According to these considerations the calculated dielectric function spectra calculated by DFT are fully validated and represent accurately the spectral optical behavior of single crystal δ-

TaN. In addition, these results show that the scattering of conduction electrons at the grain boundaries is the dominant damping mechanism of the Drude term explaining the observed high resistivity value 360 $\mu\Omega cm$, which was determined from the Drude parameters. DFT calculations of the dielectric function spectra have been also performed for TiN for comparison. The determined Γ_D^{bulk} for TaN is considerably larger than that of TiN, explaining the higher resistivity of high crystal quality TaN [185 $\mu\Omega cm$ (Ref. [11])] compared to TiN [42 $\mu\Omega cm$ (Ref. [6,7])] in the framework of the free-electron model.
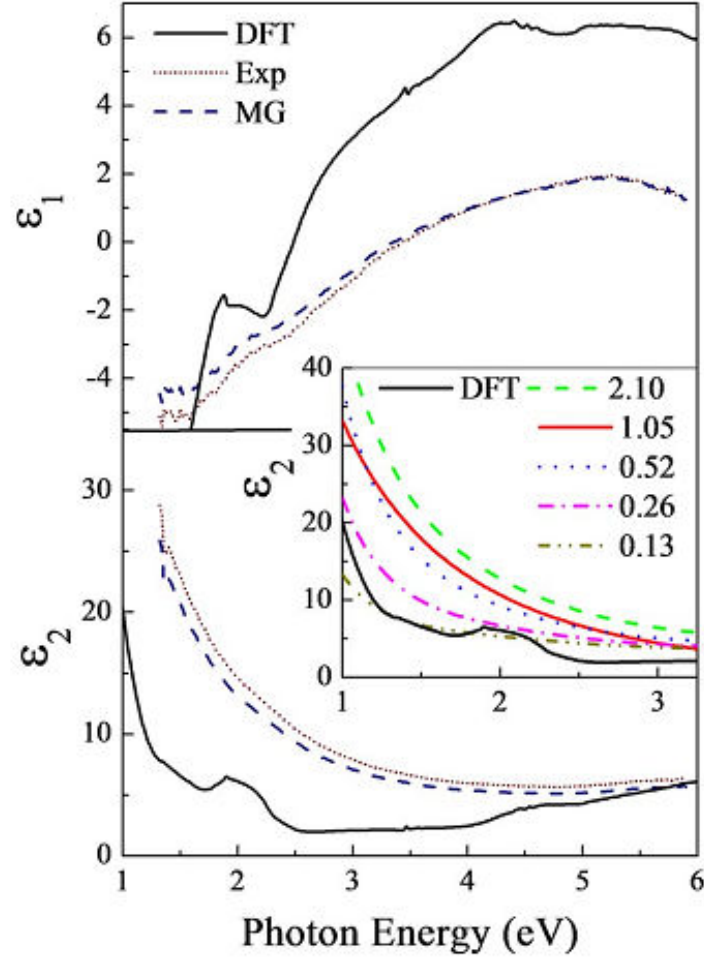
Figure 5.5: Dielectric function spectra of δ-TaN: experimental raw data (dotted lines) after the MG-EMT correction (dashed lines) and computational spectra (solid lines). The inset shows details of ε₂ from the region of strong interband absorption for simulations using the D2L model for various values of Γ_D (in eV) in comparison to the DFT data.

5.3 Optical properies of Ti-Ta-N

The electronic structure of the films can be studied through their optical properties. Optical characterization is fast, reliable, nondestructive, and of high statistical quality. The determination of the complex dielectric function enables the investigation of the material's electronic structure since ε_2 is directly related to JDOS[6]. The ε_2 spectra of TiN, TaN, and of

144

various $Ti_xTa_{1-x}N$ have been calculated from the JDOS determined by LAPW, while the ε_1 spectra were calculated from ε_2 using Kramers–Kronig integration. The calculated dielectric function spectra are presented in figure 5.6. The optical properties of $Ti_xTa_{1-x}N$ films are that of typical conductors exhibiting a strong Drude behavior resembling to TiN[7,12] and TaN[8]. The assignment of the absorption bands of $Ti_xTa_{1-x}N$ is based on the detailed electronic structure calculations given in figure 5.7.
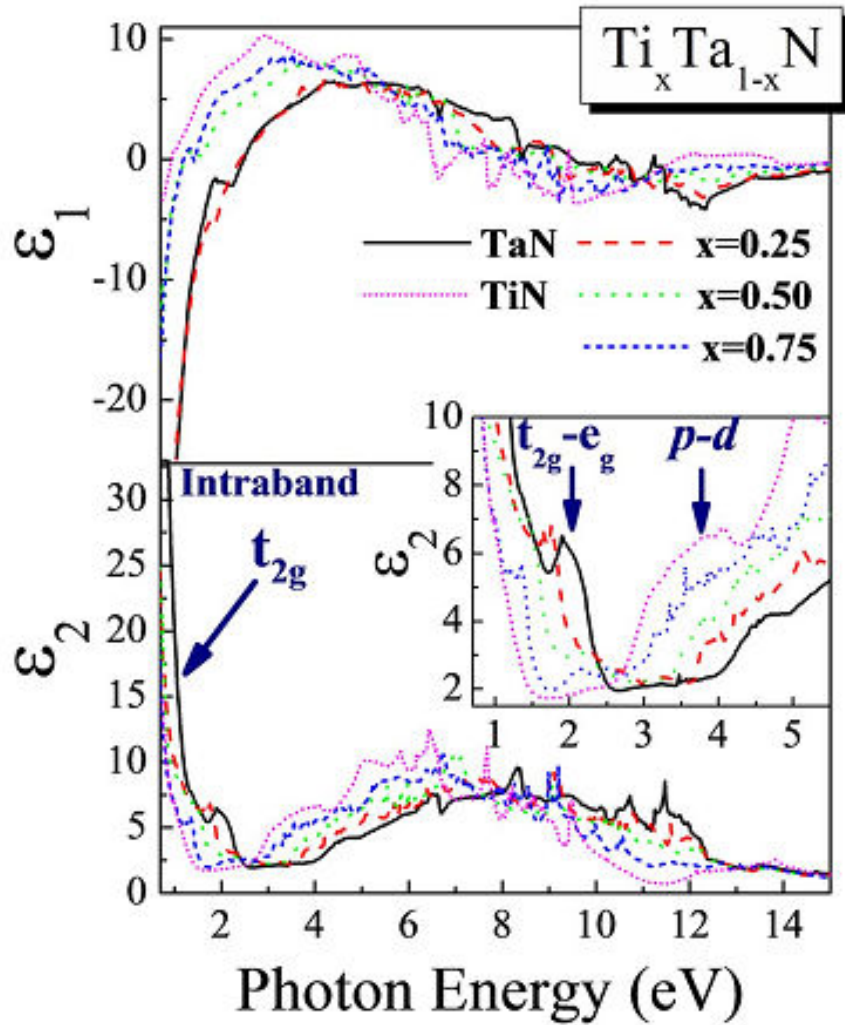
Figure 5.6: The dielectric function spectra of TiN, TaN, and various $Ti_xTa_{1-x}N$ determined by LAPW. The inset shows details of ε_2 around the principal absorptions, which have been observed in the experimental spectra.

The absorption band manifested at 1.9 eV for TaN (see inset of figure 5.6) has been previously attributed to the deviation of the intraband (intra-d) absorption from the ideal Drude description due to the transitions from the t_{2g} occupied states to e_g unoccupied states due to crystal field splitting. This spectral position is in agreement with the prediction of

crystal field theory for d^3 transition metals and confirms the partial ionic character of the TaN bonding.
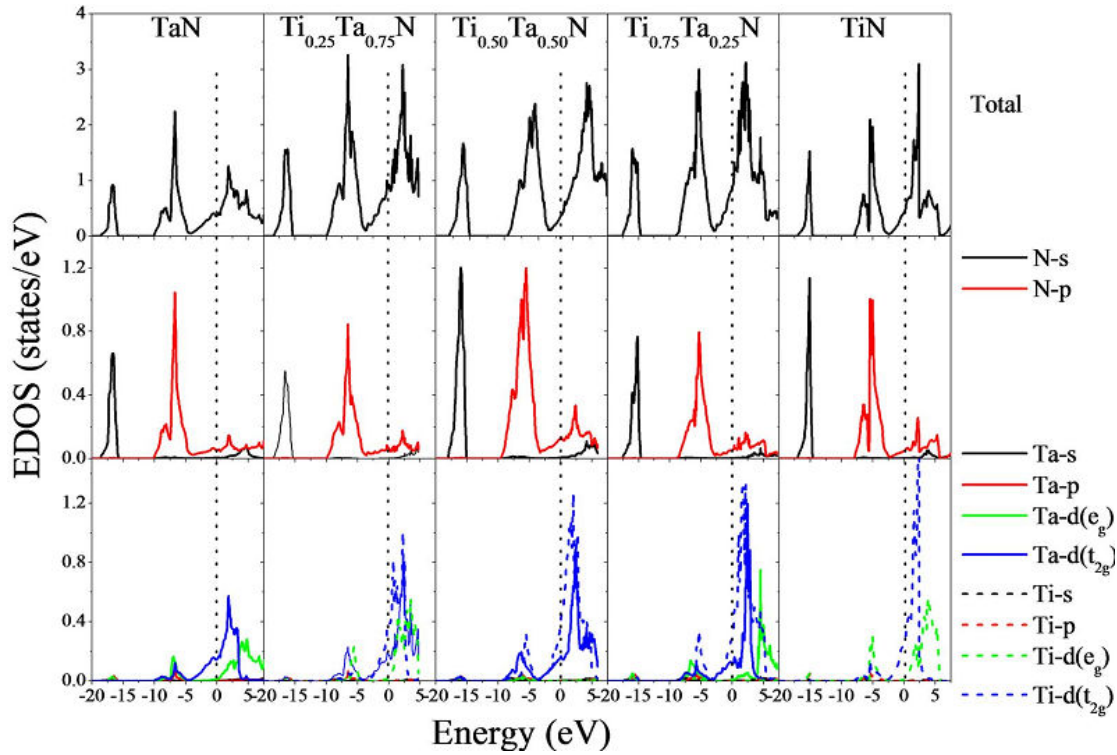
Figure 5.7: Electronic density of states for the $Ti_xTa_{1-x}N$. Zero energy stands for the Fermi level and it is denoted by vertical, dotted, black lines.

The present results further support this assignment: thus, this absorption band is absent (see inset of Fig. 5.6) in the case of $Ti_{0.50}Ta_{0.50}N$, where the e_g unoccupied states have been lacking (Fig. 5.7). In the cases of $Ti_xTa_{1-x}N$ with x=0.25 and 0.75 this absorption band is located at 1.7 and 1.3 eV, respectively. This is due to the spectral separation between the Fermi level and the maximum density of e_g unoccupied states, which decreases when increasing the Ti content (increasing x). Finally, although in the case of TiN the e_g unoccupied states exist (Fig. 5.7), this absorption band is not manifested (Fig. 5.5) because it is located at very low photon energy and, thus, it completely overlaps with the main Drude absorption below 1.2 eV.

The interband absorption spans from about 3 eV up to 13eV as presented in the ε_2 spectra in Fig. 5.6. The observed wide interband absorption originates from the states lying 5.05–6.75 eV below the Fermi level, which are predominantly due to N p electrons. A N p→Metal $d(t_{2g})$ transition is in accordance with the selection rules for photonic excitation $(\Delta l = 0, \pm 1)$ and the spectral separation between the N p states and the Fermi level (6.75 eV for TaN and 5.05 eV for TiN) that intercept the t_{2g} conduction band of the metals. The exact

146

spectral position of the N p→Metal d(t_{2g}) transitions depend on x for $Ti_xTa_{1-x}N$ due to the spectral shift in the N p states with respect to the Fermi level (Fig. 5.7).
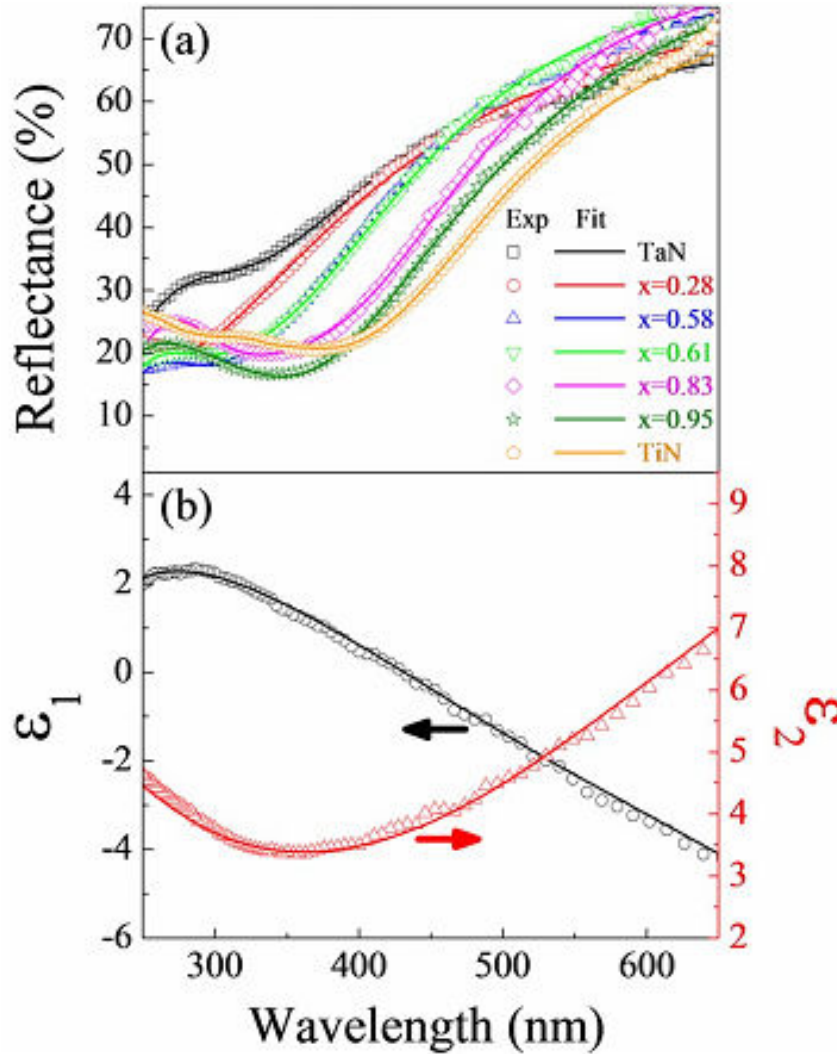
Figure 5.8: a) Experimental (symbols) and fitted with the D2L model, optical reflectance spectra for the various $Ti_xTa_{1-x}N$ films, and b) experimental (symbols) and fitted (lines) SE spectra from an as-grown $Ti_xTa_{1-x}N$ (x=0.55) film.

Thus, ε_2 shows local maxima that exhibit a gradual blueshift from 3.8 eV for TiN to about 4.6 eV for TaN (inset of Fig. 5.6), which is in agreement with experiment. The global maximum of ε_2 which is defined as the spectral separation between the EDOS maxima of the N p and the Metal-d states, is also exhibiting a gradual blueshift from the value of 6.5 eV for TiN to about 8.2 eV for TaN, in fair agreement with experiments [6.3 ±0.5 eV for TiN (Ref.[7]) and 7.3±0.5 eV for TaN (Ref.[8])].

Moreover, the optical properties of $Ti_xTa_{1-x}N$ have been also studied experimentally using ORS and SE. The experimental spectra have been fitted using a Drude term and either one (DL) or two (D2L) Lorentz oscillators in order to describe the local absorption band at

3.8–4.6 eV and the global band at 6.5–8.2 eV, as discussed previously. The use of only one Lorentz oscillator can be justified by the spectral position of the global band, which is well beyond the upper limit of the ORS spectra; in that case, the contribution of the second oscillator is summed to ε_∞. The experimental (symbols) and fitted optical reflectance spectra for various $Ti_xTa_{1-x}N$ films spectra using the D2L model (lines) are presented in Fig. 5.8.
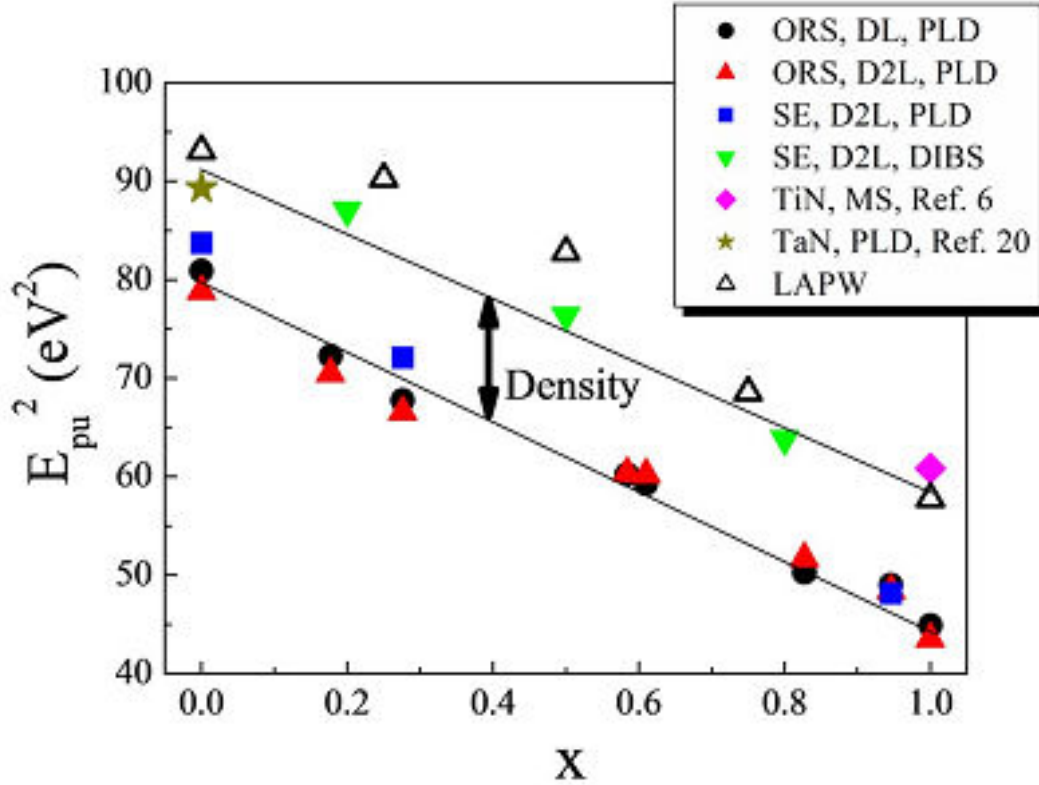
Figure 5.9: The variation in the plasma energy in Ti$_x$Ta$_{1-x}$N calculated by LAPW (open triangles) and determined from ORS and SE data for samples grown by various techniques and determined using fits with the DL or D2L models. The straight lines are guides to the eyes.

In addition, experimental (symbols) and fitted (lines) SE spectra from a representative, as-grown $Ti_xTa_{1-x}N$ (x=0.55) film are also displayed in the same spectral range for comparison. Fits with both models provide the same results, as shown in Fig. 5.9; there is also good agreement between the results from ORS (circles and triangles) and SE (squares). The experimental E^2_{pu} increases with the Ta content in agreement with the LAPW results.

According to LAPW results, the intraband absorption (metallic character) of all $Ti_xTa_{1-x}N$ originates predominantly from the metals' (Ti and Ta) d-t$_{2g}$ states[8,10] that intercept the Fermi level located at zero energy and indicated by the vertical dotted lines in Fig. 5.7, in agreement with similar findings in the case of binary nitrides[13]. The calculated E^2_{pu} values, which are proportional to conduction electron density, have been calculated from the total

EDOS and are presented in Fig. 5.9 (open triangles); we note here that for the cases of x=0.25, 0.50, and 0.75 these values may vary along different crystal orientations and the presented values in Fig. 5.9 are, in fact, the averages of all orientations for each case. The E^2_{pu} values decrease with x, in very good agreement with the experimental data. This is quite reasonable taking into account the valence electron configuration of Ti ($d^2 s^2$) and Ta ($d^3 s^2$); indeed, part of the valence charge are hybridized to form the covalent bonding and the excess of the metal's electrons (which is higher in the TaN case because of the one extra valence electron of Ta compared to Ti) constitute the Fermi gas. However, the experimental E^2_{pu} are shifted to lower values compared to the LAPW results. This is attributed to the mass density of the studied PLD-grown films that are less than the corresponding bulk values, as deduced from x-ray reflectivity analysis. Since E^2_{pu} is directly proportional to the conduction electron density, it would be affected by the mass density of the studied material, as well. Indeed, we report in Fig. 5.9 the E^2_{pu} of a pure, fully dense TiN film grown by magnetron sputtering, the corrected value for fully dense TaN (Ref. [8]) and the values of fully dense $Ti_xTa_{1-x}N$ films grown by dual ion beam sputtering (DIBS), which are in much better agreement with the LAPW results.

The Γ_D is also a very important quantity, which is affected by the scattering of conduction electrons and, therefore, accounts the electron-electron, electron-phonon, and electron-defect (point defects and grain boundaries) interactions[14]. The values for Γ_D have been determined by fitting the experimental and LAPW dielectric function spectra with the D2L model and are displayed in Fig. 5.9. The Γ_D values from LAPW are about an order of magnitude smaller than the experimental values. This is very reasonable taking into account that the experimental results refer to polycrystalline films measured at RT, while the LAPW computations have been performed for perfect single-crystals at 0 K. As mentioned in the section of the binary TaN, the Γ_D^{poly} factor for polycrystalline materials is much larger than Γ_D^{bulk} for single-crystals, due to scattering of electrons by the structural defects, and it is determined by the Fermi velocity u_F and the mean grain size G by the equation (5.2). The determined Γ_D^{bulk} for TaN is considerably larger than that of TiN, explaining the higher resistivity of high crystal quality TaN [185 $\mu\Omega cm$ (Ref. [11,15])] compared to TiN [42 $\mu\Omega cm$ (Ref. [7]) in the framework of the free-electron model, while $Ti_xTa_{1-x}N$ exhibit a consistent, monotonous but not linear relation with x. This nonlinearity is well understood considering the complexity of the Γ_D parameter.

The experimental Γ_D^{poly} data (Fig. 5.10) also exhibit a similar variation, though the absolute values are much higher due to structural defects and the nanocrystalline character of

the studied films (the mean grain size has been determined by analysis of the XRD data to be of the order of 10–20 nm). A major exception seems to be the $Ti_xTa_{1-x}N$ sample with x=0.18, which clearly deviates from the trend of the rest of the samples. However, we attribute this deviation to the fitting procedure used; more specifically, using the model (equation 1) with two Lorentz oscillators at 3.8–4.6 eV and 6–8 eV to describe the N p→Metal d(t_{2g}) transition, we do not take into account the t_{2g}→e_g transition, which is significant in the experimental spectral region only for the Ta-rich films.
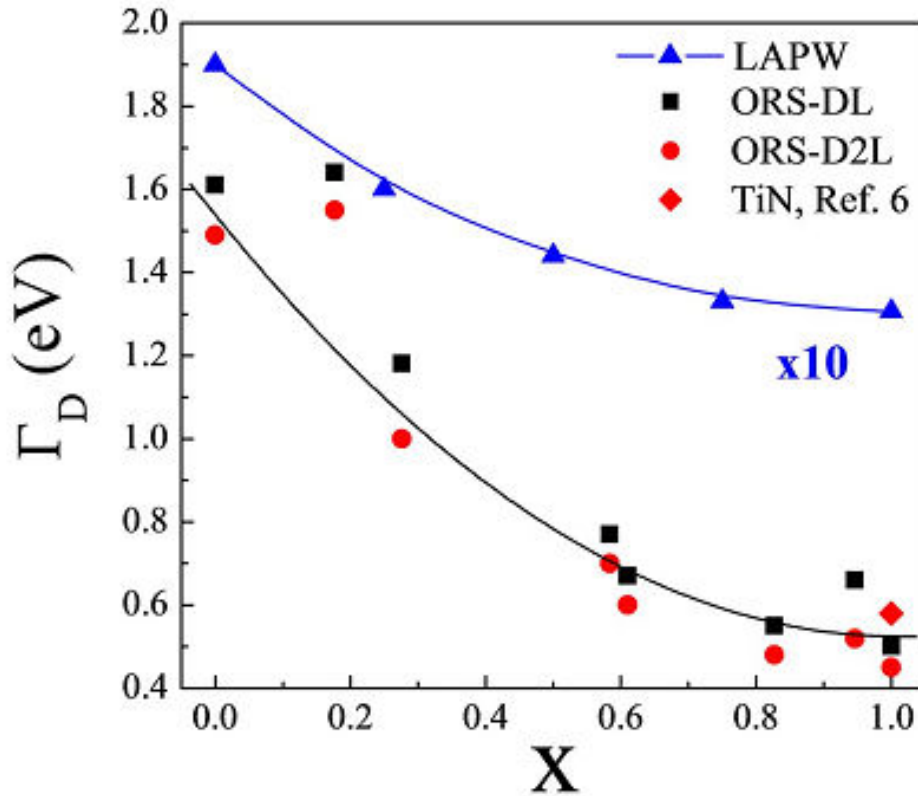
Figure 5.10: The variation in the Drude broadening in $Ti_xTa_{1-x}N$ determined from LAPW (triangles, magnified x10) and ORS data for samples grown by PLD using a Drude term and one (squares) or two (circles) Lorentz oscillators for the fits.

Thus, the Drude term used for the fits accounts for the contribution of this transition, as well, resulting to broader Γ_D for this Ta-rich sample. The samples that are close to equiatomic Ti–Ta do not exhibit this transition due to the absence of the e_g unoccupied states, while the Ti-rich samples are predicted to exhibit this transition but at lower photon energy, below 1.2 eV, i.e., beyond the experimental range. Finally, for the pure TaN the one Lorentz oscillator converges spontaneously to a value of 2 eV, Fig. 5.11, which is consistent with previous experiments and the presented LAPW results assigning this peak to the t_{2g}→e_g transition. This is not occurring for the sample with x=0.18 most likely because the t_{2g}→e_g transition is not so

150

well defined. The spectral positions of the Lorentz oscillators determined by the fits on the experimental spectra are summarized in Fig. 5.11. The principal oscillator describes the local maximum of the N p→Metal d(t_{2g}) transition indicated by the arrow in the inset of Fig. 5.6. The spectral position of this oscillator exhibits a blueshift with increasing Ta-content in agreement with the LAPW calculations (Fig. 5.6). In addition, the results for pure, PLD-grown TiN are in very good agreement with the corresponding results for sputtered TiN. Finally, the value of 4.3eV for pure TaN does not contradict the recently reported value of 7.3 eV, since this is the result of a fit in the spectral region 1.46–4.96 eV where only the local maximum of the N p→Metal d(t_{2g}) transition is taken into account Fig. 5.6, while in Ref. 8 the ellipsometry data up to 6.0 eV took into account the low energy tail of the global maximum of the N p→Metal d(t_{2g}) transition located at 7.3 ±0.5 eV. We should note here that the spectral positions of the interband transitions (Lorentz oscillators) might be affected by the stress[16-18] and the grain size[19].
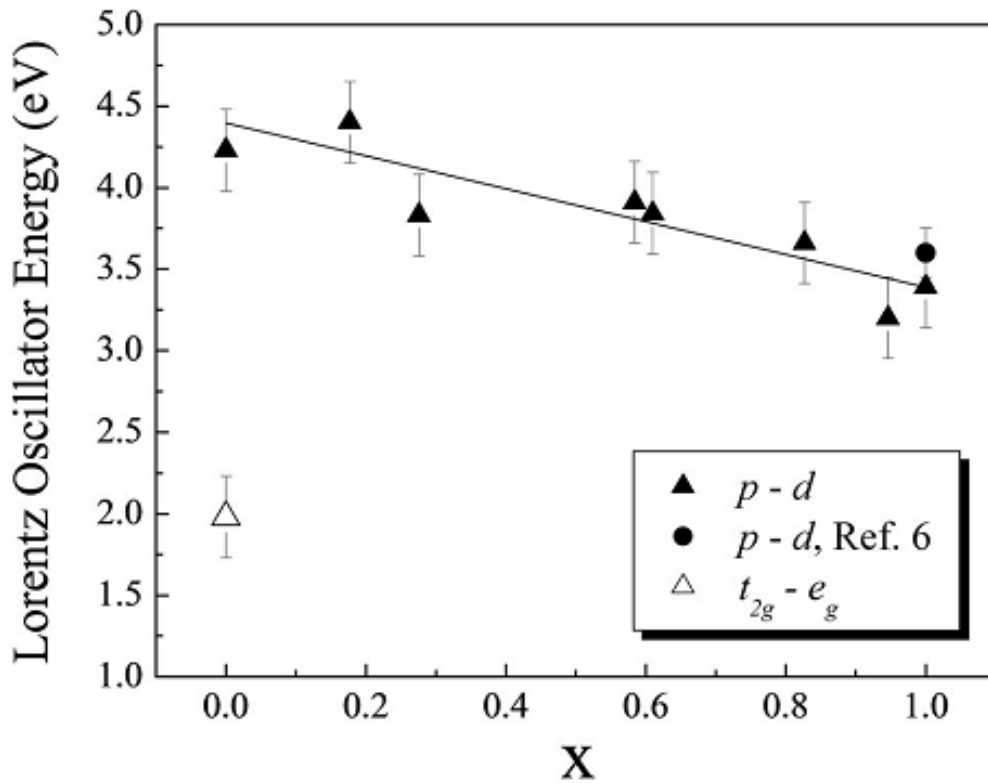
Figure 5.11: The spectral positions of the experimental Lorentz oscillators, which are assigned to the main electronic transitions manifested in the experimental spectral range.

However, by comparing as grown and annealed films we identified that the effect of stress in the interband transitions in our films is of the order of 100 meV, which is much less than the error bars in Fig. 5.11, while the grain size of the films is long enough (10–20 nm) to eliminate quantum confinement effects and restore the spectral positions of the bulk material.

For practical applications in microelectronics the most important factor are the values of $Ti_xTa_{1-x}N$ resistivity. The E_{pu} and Γ_D parameters may be used for the study of the transport properties of conduction electrons of the $Ti_xTa_{1-x}N$ layers, as well, through the calculation of the electrical resistivity $\left(\rho\right)$ according to the free-electron model[20], following the formula in SI units:

$$\rho = \left(\frac{1}{\varepsilon_0}\right)\frac{\hbar^2 \cdot \Gamma_D}{E_{pu}^2} \qquad (5.1)$$

In Fig. 5.12 is demonstrated the variation in the resistivity in $Ti_xTa_{1-x}N$ determined from the optical data through Eq.3 for various samples (excluding the sample with x=0.18 due to its inaccurate Γ_D value). We observe that for the PLD-grown samples there is a monotonous increase in resistivity with increasing Ta-content, which is consistent with the values for bulk, highly crystalline TiN (Ref. [7]) and TaN[8].

The resistivity values of DIBS-grown samples are also shown for comparison. The specific values presented in Fig. 5.12 are process-dependent, since they are significantly affected by the structural defects. Much lower values can be achieved by eliminating the structural defects. Indeed, lower resistivity values have been determined after vacuum annealing of representative samples   (Fig. 5.12, open diamonds) due to partial annealing out of defects and 10%–15% increase in the mean grain size. Further reduction may be achieved by growing $Ti_xTa_{1-x}N$ at higher temperature and achieving greater mean grain size. In any case, the resistivity of $Ti_xTa_{1-x}N$ will get intermediate values between those of TiN and TaN of the same structural quality. The more interesting effect is the resistivity of the DCMS grown samples which varies a lot as a function of composition. This is happening due to microstructure change from columnar (with big vertical grains) to globular (very small grains). PLD and DIBS samples do not change microstructure and the variation in resistivity is an intrinsic effect based on the addition of Ta.
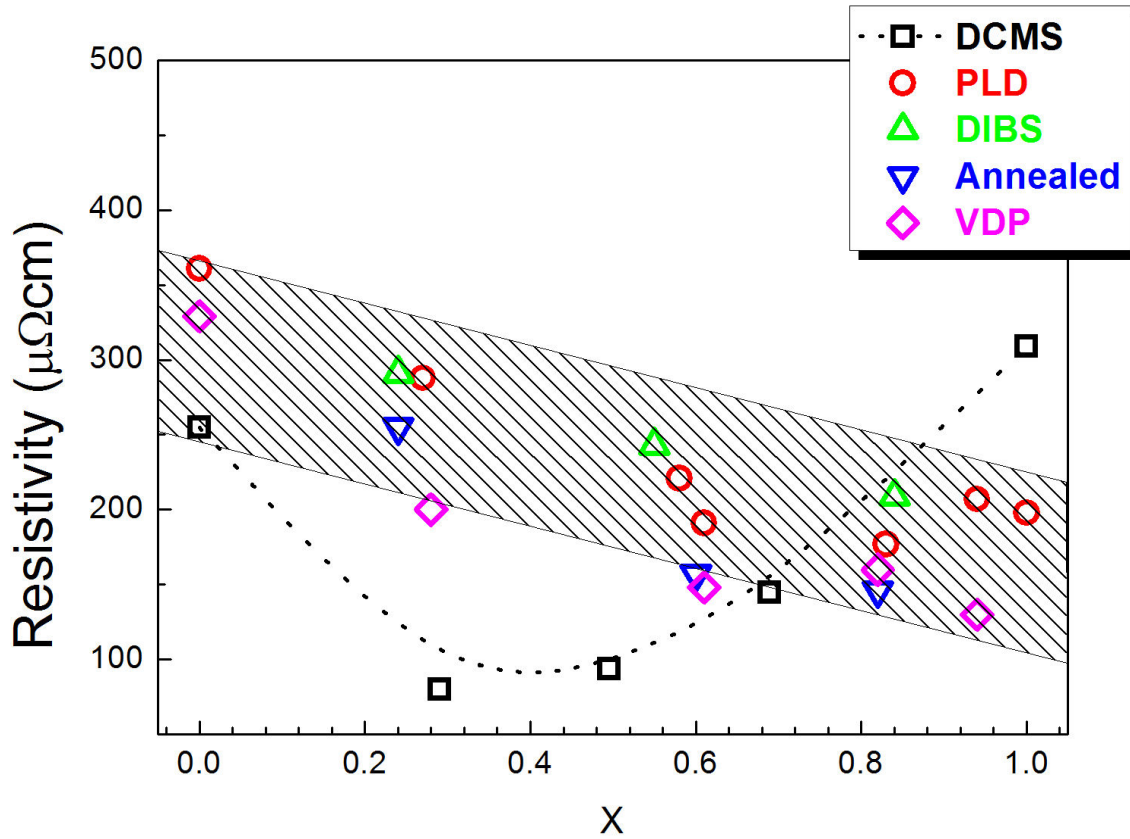
Figure 5.12: The variation in the resistivity of Ti$_x$Ta$_{1-x}$N for various samples.

Summarizing, all Ti$_x$Ta$_{1-x}$N films are good conductors with varying density of conduction. The plasma energy of fully dense Ti$_x$Ta$_{1-x}$N has been found to increase from 7.8 to 9.45 eV with increasing Ta-content. The electron conductivity in Ti$_x$Ta$_{1-x}$N is mainly due to the Metal(Ti /Ta)d(t$_{2g}$) states. Additional optical absorption bands are manifested due to the N p→Ti /Ta d interband transition and the t$_{2g}$→e$_g$ transition due to crystal field splitting of the metals' d band, especially for the Ta-rich samples. The spectral position of the interband transitions exhibits a blueshift with increasing Ta-content due to the varying spectral location of the N p states with respect to the Fermi level for various x. The resistivity values of TixTa$1−x$N are comparable to those of polycrystalline TiN and TaN films and lying from 200 to 360 $\mu\Omega cm$, thus making these films promising candidates for substitution of TiN and TaN in electronic applications, where a better lattice match is required. A significant reduction in the resistivity down to 145 $\mu\Omega cm$ has been achieved by the annealing out of defects. Based on the LAPW results we anticipate that further reduction in the resistivity can occur in Ti$_x$Ta$_{1-x}$N of better crystalline quality.

5.4 Plasma energy and work function

In this section we present a detailed study of the work function and the plasma energy for the widest range of binary and ternary $Ti_xMe_{1-x}N$ and $Ta_xMe_{1-x}N$ (Me: Ti, Zr, Ta, Nb, Hf, Mo, W) films reported ever[21-26]. All the films were deposited by pulsed laser deposition and the structural and compositional results were described in chapter 4. The optical properties were studied using optical reflectance spectroscopy (ORS) (Fig. 5.13, inset), which revealed the typical behavior of conductors. Thus, the optical data were analyzed to the contributions of intraband and interband transitions described by a Drude term and two Lorentz oscillators, respectively. This modeling determines accurately the plasma energy E_p, which is directly correlated with the conduction electron density N

$$E_p = \hbar\omega_p, \quad \omega_p = \sqrt{\frac{Ne^2}{\varepsilon_0 m^*}}, \qquad (5.2)$$

(where e is the electron charge, ε_0 is the permittivity of free space, and m^* is the electron effective mass, in SI units). Ep is an intrinsic property of the material because it determines the electron conductivity at zero temperature and with zero defects. Of course for realistic device applications the electron scattering, which is affected by the structural defects and the temperature, is also very important and should be taken into account. The following correction: $\left(E_p^{corr} / E_p\right)^2 = \rho_{ref} / \rho_{exp}$, where ρ_{ref} and ρ_{exp} are the reference and experimental mass density measured by x-ray reflectivity for each case, respectively, has been applied in order to deduce the E_p values of the fully dense films presented in Fig. 5.13.
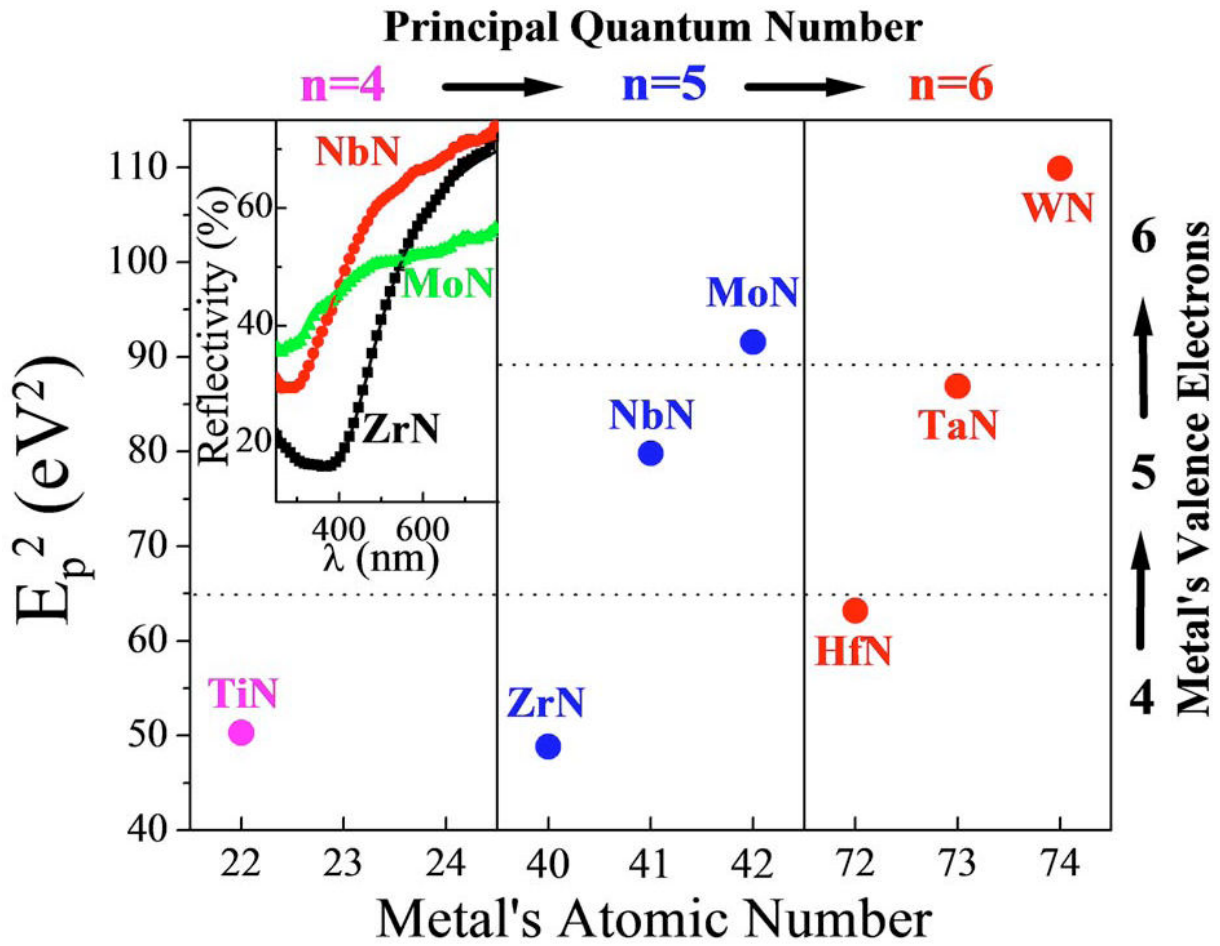
Figure 5.13: The variation of E_{pu}^2 for binary TMN, which are grouped according to the number of valence electrons of the constituent metal. Inset: ORS experimental and fitted spectra of row-5 TMN.

E_{pu}^2 values are rationally grouped according to the metal's quantum numbers (principal quantum number and number of valence electrons), as shown in Fig. 5.13. Nitrides of metals of the same group (e.g., TiN, ZrN, and HfN, whose metals share the same d^2s^2 valence electron configuration) exhibit similar E_{pu}^2 values, while E_{pu}^2 increases with increasing number of valence electrons. This is quite reasonable if we take into account that part of the metal's valence charges are hybridized to form the covalent bonding with N and the excess of the metal's electrons (which are increasing with increasing number of metal's valence electrons) constitute the Fermi gas.

The E_{pu}^2 values of each ternary nitride system follow an almost linear correlation with the α, as shown in Fig. 5.14, and the composition x of the films. The more generalized view of E_{pu}^2 versus α for all the binary and ternary nitrides is much more complex. Thus, the phase space of E_{pu}^2 with the nitride's α has an almost triangular shape with TiN, ZrN, and WN being at the vertices; TaN is also indicated in Fig. 5.14 for comparison. The form of this phase space reveals that $Ti_xZr_{1-x}N$ is the most versatile system for low-mismatch growth on various

semiconductors since it exhibits almost constant E^2_{pu} (i.e., conduction electron density) and varying α in the vast range of 0.432–0.469 nm.
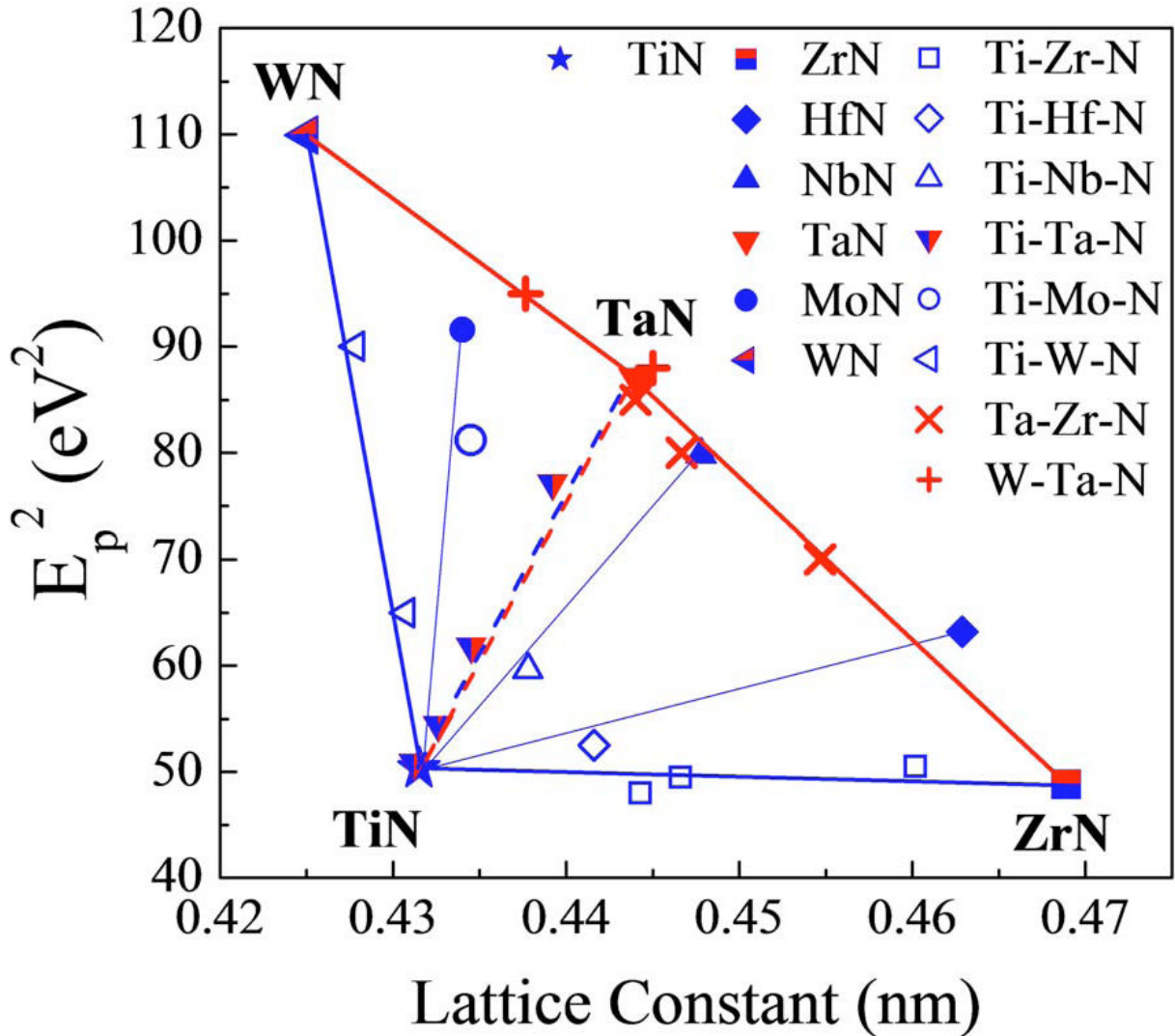
Figure 5.14: The phase space of E^2_{pu} (which is proportional to conduction electron density) vs the nitride's lattice constant.

On the other hand, the $Ti_xW_{1-x}N$ system provides the ability to grow conducting epilayers of similar α (below 0.430 nm) but with E^2_{pu} considerably varying; as a result, conducting layers of varying resistivity can be grown, e.g., for MEMS applications. The whole phase space can be covered by alloying the various nitrides.

Another important factor for Ohmic behavior of a contact is the WF of the conductor. In the case of n-type semiconductors, the metal's WF should be equal to the electron affinity of the semiconductor[27]. Relative WF values of selected $Ti_xZr_{1-x}N$ samples have been determined by *ex situ* Kelvin probe measurements. In order to estimate the absolute values, these relative values were scaled to the value WF_{TiN}=3.74 eV of a reference, stoichiometric

156

TiN sample (assuming that possible adsorbates from the ambient would be the same for all samples), and are presented in Fig. 5.15 along with the values of various binary nitrides reported in Refs.[28] and [29] (for comparison), and the electron affinities and lattice constants of III-nitride semiconductors.
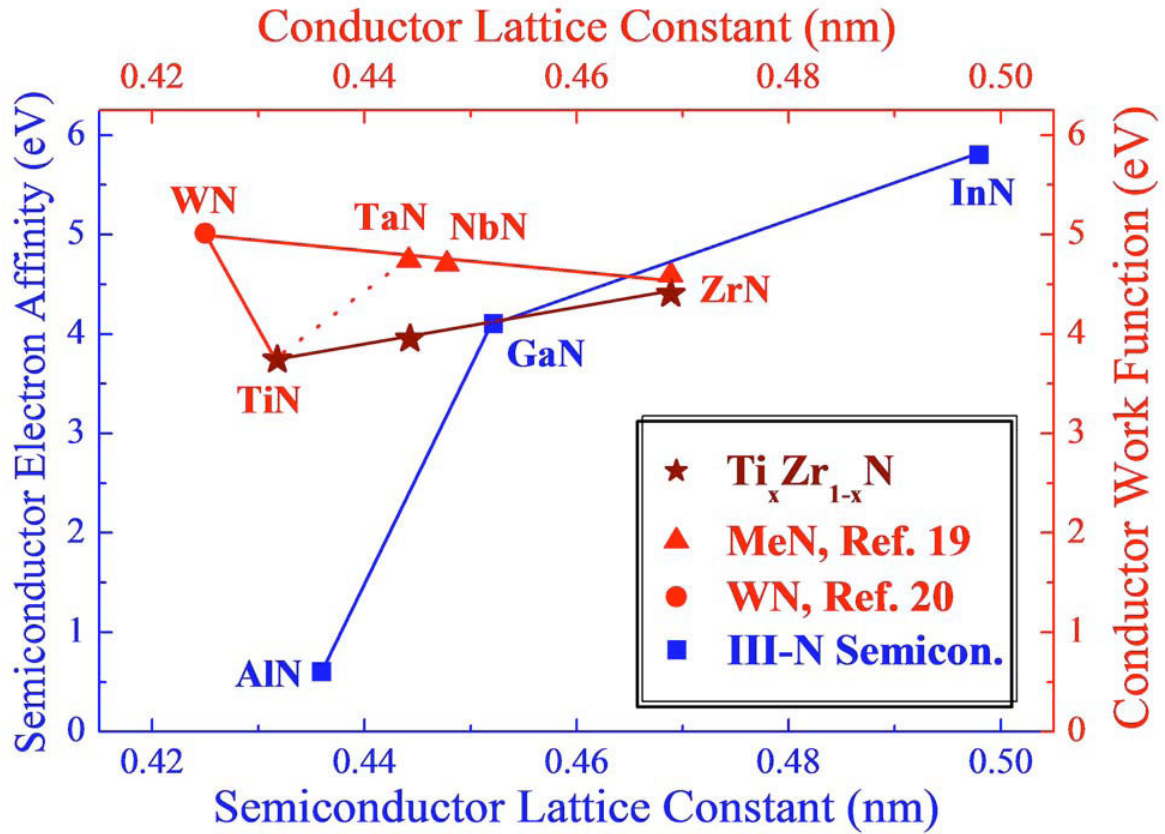
Figure 5.15: The variation of WF with the nitride's lattice constant in comparison with the electron affinities and the lattice constants of III-nitrides.

We note here that for simplicity the lattice constants of III-nitrides presented in Fig. 5.15 are for the zincblende polytypes; in the case of the wurtzite polytypes, the picture is similar for heteroepitaxy of the (111) rocksalt conductor nitride along the (0001) III-nitride semiconductor[30]. It is evident that $Ti_xZr_{1-x}N$ is structurally and electrically appropriate as growth template or Ohmic contact for n-type $In_yGa_{1-y}N$. Following similar considerations and taking into account the bandgap values of the III-nitrides, $W_xTa_{1-x}N$ might be also promising as contact on p-type $Al_yGa_{1-y}N$.

References

[1] M. Sahnoun, C. Daul, M. Driz, J. C. Parlebas, and C. Demangeat, Computational Materials Science **33,** 175-183 (2005).

[2] C. Stampfl, W. Mannstadt, R. Asahi, and A. J. Freeman, Physical Review B - Condensed Matter and Materials Physics **63,** 1551061-15510611 (2001).

[3] P. Blaha, K. Schwarz, G. K. H. Madsen, D. Kvasnicka, and J. Luitz, WIEN2k, An Augmented Plane Wave + Local Orbitals Program for Calculating Crystal Properties (2001).

[4] J. P. Perdew and Y. Wang, Physical Review B **45,** 13244-13249 (1992).

[5] J. P. Perdew, K. Burke, and M. Ernzerhof, Physical Review Letters **77,** 3865-3868 (1996).

[6] W. A. Harrison, *lectronic Structure and the Properties of Solids* (Freeman, San Fransisco, 1980).

[7] P. Patsalas and S. Logothetidis, Journal of Applied Physics **90,** 4725-4734 (2001).

[8] G. M. Matenoglou, L. E. Koutsokeras, C. E. Lekka, G. Abadias, S. Camelio, G. A. Evangelakis, C. Kosmidis, and P. Patsalas, Journal of Applied Physics **104** (2008).

[9] F. Wooten, *Optical properties of solids* (New York, 1972).

[10] R. L. Carter, *Molecular Symmetry and Group Theory* (Wiley, New York, 1998).

[11] C. S. Shin, Y. W. Kim, N. Hellgren, D. Gall, I. Petrov, and J. E. Greene, Journal of Vacuum Science and Technology A: Vacuum, Surfaces and Films **20,** 2007-2017 (2002).

[12] S. Gautier, P. Komninou, P. Patsalas, T. Kehagias, S. Logothetidis, C. A. Dimitriadis, and G. Nouet, Semiconductor Science and Technology **18,** 594-601 (2003).

[13] D. A. Papaconstantopoulos, W. E. Pickett, B. M. Klein, and L. L. Boyer, Physical Review B **31,** 752 (1985).

[14] U. Kreibig, J. Phys **F4,** 999 (1974).

[15] S. M. Aouadi and M. Debessai, Journal of Vacuum Science and Technology A: Vacuum, Surfaces and Films **22,** 1975-1979 (2004).

[16] J. E. Rowe, F. H. Pollak, and M. Cardona, Physical Review Letters **22,** 933 (1969).

[17] J. E. Wells and P. Handler, Physical Review B **3,** 1315 (1971).

[18] P. Tyagi and A. G. Vedeshwar, Physical Review B **66,** 075422 (2002).

[19] J. M. Wagner and F. Bechstedt, Physical Review B **66,** 115202 (2002).

[20] H. V. Nguyen, I. An, and R. W. Collins, Physical Review Letters **68,** 994 (1992).

[21] T. Seppanen, L. Hultman, J. Birch, M. Beckers, and U. Kreissig, Journal of Applied Physics **101,** 043519-6 (2007).

[22] M. H. Oliver, J. L. Schroeder, D. A. Ewoldt, I. H. Wildeson, V. Rawat, R. Colby, P. R. Cantwell, E. A. Stach, and T. D. Sands, Applied Physics Letters **93,** 023109-3 (2008).

[23] T. Joelsson, L. Hultman, H. W. Hugosson, and J. M. Molina-Aldareguia, Applied Physics Letters **86,** 131922-3 (2005).

[24] W. W. Jang, J. O. Lee, J.-B. Yoon, M.-S. Kim, J.-M. Lee, S.-M. Kim, K.-H. Cho, D.-W. Kim, D. Park, and W.-S. Lee, Applied Physics Letters **92,** 103110-3 (2008).

[25] N. N. Iosad, N. M. van der Pers, S. Grachev, V. V. Roddatis, B. D. Jackson, S. N. Polyakov, P. N. Dmitriev, and T. M. Klapwijk, Journal of Applied Physics **92,** 4999-5005 (2002).

[26] S. M. Aouadi, Journal of Applied Physics **99,** 053507-6 (2006).

[27] S. M. Sze, *Physics of Semiconductor Devices* (Wiley, new York, 1981).

[28] G. Yasuhito, T. Hiroshi, and I. Junzo, in *Measurement of work function of transition metal nitride and carbide thin films*, 2003 (AVS), p. 1607-1611.

[29] P.-C. Jiang, Y.-S. Lai, and J. S. Chen, Applied Physics Letters **89,** 122107-3 (2006).

30   P. Ruterana, G. Nouet, K. Th, K. Ph, K. Th, M. A. d. F. Poisson, F. Huet, and H. Morkoc, physica status solidi (a) **176,** 767-771 (1999).

CHAPTER 6

CONCLUSIONS & PERSPECTIVES

6.1 Conclusions

Summarizing, the present thesis has covered a very wide area on the study of transition metal nitrides (TMN) thin films. Three different deposition techniques in terms of energy flux were used to grow samples, in order to study how these films grow and what are the processes governing the crystal structure and the microstructure. All the transition metals have been used (Ti, Zr, Nb, Mo, Hf, Ta, W), except V and Cr, to study structural properties, microstructural features and functional properties as well as optical and electronic properties. This wide range of study has been performed in order to reveal the universal mechanisms for this type of material and not just to study them case by case. To strengthen the results we have to notice that the presented results are totally lab-independent, since the growth, the characterization and the analysis has been done in two different institutions.

Another aspect covered by this thesis, is the vast amount of experimental data gathered in one place and categorized accordingly. As grown and stress-free lattice parameters for all binary and ternary TMNs; texture orientation and grain size as a function of composition and deposition technique. All the grown films exhibit several microstructures from fiber-texture to granular and the variation of hardness and stress can be found as a function of composition.

The optical data have been extracted mainly from two optical techniques, optical reflectance spectroscopy and spectroscopic ellipsometry. From these measurements we have obtained the interband and intraband transition energies of the TMN. Plasma energy values also have been estimated from optical measurements. These values can provide information about the conduction electron density of the nitrides and they have been confirmed from conductivity measurements as well. Moreover, from optical measurements we have extracted structural information about the films which were at excellence agreement with the structural measurements.

Another set of values for nitrides is the work function. The work function is an important parameter for the design of integrated circuits, since it has to match with the corresponding value of the electron affinity of the semiconductors in order not to insert resistivity at the interfaces. The work function value is the starting point, where a nitride system is selected and tailored accordingly to match the lattice constant of the semiconductor.

The extensive study and the plethora of experimental data provided an insight of the mechanisms that govern the physics of these materials. The crystal structure of TMNs has been studied experimentally and theoretically and found that all ternary and binary nitrides can be stabilized in the rocksalt structure just by deposited under appropriate deposition conditions. The preferred orientation of the grains is a function of deposition conditions and

162

growth flux as well as the residual stress of the final films. The lattice size of the ternary nitrides can by described by the Vegard's law (in absence of growth stress) but the electronic study revealed that deviation from this linear correlation exists. Indeed, this has also manifested in our experimental measurements. The electronic study explained the formation of the ternary nitrides consisting from totally immiscible metals and the optical transitions showed exactly the same result.

6.2 Perspectives

An interesting future plan to extend this research could be the formation of solid solutions of multiple transition metal nitrides in order to investigate the validity of the recorded results. Quarternary nitrides based on these materials are favorable to obey to the same mechanisms and processes as described in this thesis. But due to the complexity of the system, other effects could also arise such as magnetic properties or superconductivity. Since the basic study has already been performed about the fundamental aspects of the films structure, microstructure *etc*, this investigation might be straightforward to be done.

The majority of the films studied in this study were polycrystalline and the crystalline quality was described totally in terms of grain structure. But the needs in the semiconductor industry require films of superior crystalline quality such as epitaxial. Epitaxial films could only be grown under circumstances such as the low lattice mismatch among the epilayers (for the case of TMNs on MgO(100) substrates or along the basal planes of sapphire substrates). It could be useful to extend the research on properties of epitaxial TMN films since these kinds of films are required in many cases in the semiconductor industry.

Staying in the same category of the single phase materials, multilayers of TMN have already been investigated but only in binary systems. The better understanding of the formation of the ternary compounds as well as the huge range of possible combinations can lead to multilayer films with interesting properties.

Another great opportunity arisen from this study is that ternary TMN can exhibit superior properties compared to their binary counterparts. The trend on nowadays research is about the nanocomposites materials. Nanocomposites based on TMN have shown remarkable properties and the effort is applied on how to tailor the separate constituents of nanocomposites to achieve the required properties. The ternary transition metal nitrides may offer a different starting point for the creation of composite materials with unique characteristics. This is a possibility that worth taking the effort to try.

Finally, the results presented in this thesis have demonstrated that a wide variety of films with tailored lattice sizes and conductivities/resistivites have ben grown. These films might be useful for all-ceramic durable optoelectronic devices, e.g. light emitting diodes (LED), if used either as growth templates for II-nitrde semiconductor growth and/or as metal contacts for III-nitride semiconductors. Therefore, a very reasonable future plan is to grow epitaxially such ternary TMNs on III-nitride semiconductors and produce all-ceramic LEDs and investigate their efficiency and durability.

APPENDIX

Part I

Dielectric Function

The dielectric function is a complex function that describes the response of a medium to an external electromagnetic field. The complex dielectric function is a function of wavelength and it consists from the real dispersion part and the complex part which is correlated with the absorption. Also the dielectric function can be expressed in terms of the complex refractive index n and the attenuator factor k.

$$\tilde{\varepsilon} = \varepsilon_1 + i\varepsilon_2 = (n + ik)^2$$

Where
$$\begin{cases} \varepsilon_1 = n^2 - k^2 \\ \varepsilon_2 = 2nk \end{cases}$$
and
$$\begin{cases} n = \sqrt{\dfrac{\sqrt{\varepsilon_1^2 + \varepsilon_2^2} + \varepsilon_1}{2}} \\ k = \sqrt{\dfrac{\sqrt{\varepsilon_1^2 + \varepsilon_2^2} - \varepsilon_1}{2}} \end{cases}$$

The optical model

The model which describes the behavior of the transition metal nitrides is the addition of a Drude term, a Lorenz term with two oscillators and the ε_∞.

$$\varepsilon(\omega) = \varepsilon_\infty - \frac{\omega_{pu}^2}{\omega^2 - i \cdot \Gamma_D \cdot \omega} + \sum_{j=1}^{2} \frac{f_j \cdot \omega_{oj}^2}{\omega_{oj}^2 - \omega^2 + i \cdot \gamma_j \cdot \omega}$$

Each of the below terms has parameters which are connected with the material properties; all these parameters will be explained below for each term.

The Drude term is describing the free conductive electrons of the solid. It is consisted of two parameters the unscreened plasma energy ω_{pu} and the dumping factor Γ_D. The parameter ω_{pu} is related with the density of the free electrons defined by the relation

$$\omega_{pu} = \sqrt{\frac{N \cdot e^2}{\varepsilon_o \cdot m^*}}$$

168

where N is the conduction electron density, e is the electron charge, ε_0 is the permittivity of free space and m^* is the electron effective mass.

The second important parameter of the Drude term is the dumping factor Γ_D. This parameter is describing the scattering of the free electrons and it includes terms of electron-electron, electron-phonon and electron-defects (point defects and grain boundaries). The value of the dumping factor is related to the relaxation time of electrons according to the free electron theory by the equation:

$$t_D = \frac{\hbar}{\Gamma_D\left(eV\right)}$$

The Lorentz term is consisted of two oscillators which describe the intra-band and inter-band transitions. Each of the Lorentz oscillators is located at an energy position ω_{0j}, with strength f_j and damping (broadening) factor γ_j.

The last strength is the epsilon affinity which is a background constant, larger than unity, due to higher-energy contributions (beyond the experimental spectral range) referring to transitions that are not taken into account by the Lorentz terms (eg X-rays).

Optical Reflectance Spectroscopy

The aim of this analysis is to define the parameters of the Drude2Lorentz model by measurements of the optical reflectivity. The reflectivity of a material is a function of the complex refractive index $n\left(\omega\right)$ and the incident angle ϑ. For a constant and vertical incident angle $\vartheta = 0^o$ the reflectivity is only a function of $n\left(\omega\right)$ and $k\left(\omega\right)$ which is the attenuation factor and describes the absorption of the solid. The reflectance can be expressed by:

$$R\left(\omega\right) = \frac{\left[n\left(\omega\right)-1\right]^2 + k^2\left(\omega\right)}{\left[n\left(\omega\right)+1\right]^2 + k^2\left(\omega\right)}$$

Combining the initial equations of the dielectric function and the refractive index, the reflectivity can be expressed in terms of the dielectric function, facilitating the implementation of the Drude2Lorentz and the minimization procedure.

Spectroscopic Ellipsometry

Ellipsometry measures the complex reflectance ratio, ρ (a complex quantity), which is the ratio of r_p over r_s:

$$\rho = \frac{r_p}{r_s} = \tan\left(\Psi\right)e^{i\Delta}$$

Thus, tan(Ψ) is the amplitude ratio upon reflection, and Δ is the phase shift (difference). The analysis of the spectroscopic ellipsometry is little different from the optical reflectance, which measures the reflectivity $R=rr^*$. The ellipsometry, as described in chapter 3, provides data about the relative change of the polarization angles Ψ and Δ. The change in the polarization angles is linked with the Fresnel equations for the reflectance and the transmittance.

Part II

Coordinate systems – reference frames

Crystallographic coordinate system

It is defined by the basic vectors (a_1,a_2,a_3) of the conventional unit cell. The elastic compliances and the stiffness are known in this reference frame. This coordinate system is defined by the three vectors of the primitive cell (cubic, for simplicity):

Sample Reference Frame

This frame is define by the vectors S. The S_3 is in the direction of the sample normal and the other two (S_2,S_3) are lying in the plane of the sample. The stresses are usually referenced to this coordinate system (biaxial, triaxial, and hydrostatic).

This coordinate system is referenced to individual crystallites and it's orientation with respect to the substrate is determined by the orientation of the crystallite axes. For fiber-texture films every crystallite must be treated to its own S frame. For example for all crystals with the (111) face parallel to the film surface we will use:

$$S_1 = \left[\overline{1}10 \right]$$
$$S_2 = \left[\overline{1}\,\overline{1}2 \right]$$
$$S_3 = \left[111 \right]$$

Laboratory Reference System

This frame is formed by rotating the S system by an angle φ about S_3 and then rotating about L_2 by an angle ψ. The lattice parameter measurements are performed in this system. We choose the orientation of the laboratory system so that the scattering vector **q** lies along the direction L_3. We measure a d-spacing $d_{\psi\varphi}$ which is related to the strain in the laboratory system $\left(\varepsilon_{33}^L \right)_{\psi\varphi}$ by:

$$\left(\varepsilon_{33}^L \right)_{\psi\varphi} = \frac{d_{\psi\varphi} - d_0}{d_0}$$

Elastic Quantities

There are two equivalent conventions (tensor and enginnering) for representing the stress, strain and the elastic compliances of a sample. In the tensor representation, the stresses σ_{ij} and the strains ε_{ij} are 3x3 tensors and the compliances s_{ijkl} and stiffness c_{ijkl} are 3x3x3x3 tensors. Rotation of these quantities from one coordination system to another is performed by standard tensor rotations. For example, the laboratory reference frame strain tensor ε^L can be found from the sample reference frame strain tensor ε^S by rotation with the transformation matrix M^{SL}, which is an 3x3 array with components M_{ik}^{SL} which are the directions cosines between the ith direction in the laboratory reference frame and the kth direction in the sample reference frame.

$$\varepsilon^L = M^{LS} \varepsilon^S M^{SL} \tag{1}$$

Where M^{LS} is the transpose of M^{SL}. Equation 5 represents a matrix multiplication where the result ε^L is a tensor with components

$$\varepsilon_{ij}^{\ L} = M_{ki}^{\ LS} M_{lj}^{\ SL} \varepsilon_{kl}^{\ S}$$

Where summing over different indices is implied.

For rotation from the sample reference frame to the laboratory reference frame as shown in figure 3.5, the transformation matrix is

$$M^{SL} = \begin{pmatrix} \cos\phi & -\sin\phi & \cos\phi\sin\psi \\ \sin\phi\cos\psi & \cos\phi & \sin\phi\sigma\iota\nu\psi \\ -\sin\psi & 0 & \cos\psi \end{pmatrix}$$

Compliances and stiffnesses are know in for the crystallographic reference frame, and they can be rotated to any desired reference frame in a similar manner. In addition, the compliance and the stiffness tensor are just the inverse to each other.

$$\sigma_{ij} = c_{ijkl}\varepsilon_{kl} \quad (6)$$
$$\varepsilon_{ij} = s_{ijkl}\sigma_{kl} \quad (7)$$

Where c_{ijkl} and s_{ijkl} are the elements of the stiffness and compliance tensors, respectively.

The engineering representation of the elastic quantities utilizes simplifications resulting from the symmetry of the system. The 3x3 strain tensor can be represented a 1x6 vector and similarly for the stress. There are some transformation rules to engineering representation but rotations of quantities from one reference frame to another cannot be performed without transforming back to the tensor representation.

A typical manipulation which applies to a crystalline in any textured film is outlined below. Starting with the film frame stresses and the unstrained lattice parameter, we calculate the observer lattice parameter for a given reflection in the following steps:

1. The film frame 3x3 stress tensor is rotated into the crystallographic reference frame

2. The crystallographic reference frame stress tensor is then transformed to a 1x6 vector (using the transformation rules).

3. Hook's law is applied using the crystallographic frame s_{ij} to find the crystallographic frame enginnering strain 1x6.

4. This vector is transformed to the tensor representation crystallographic frame strain 3x3 tensor.

5. This tensor is rotated to find the laboratory frame strain component $\varepsilon_{33}{}^{L}$ for a particular reflection with q pointing along L_3.

6. This then used in Equation 4 together with the unstrained lattice parameter to find the observed lattice parameter.

7. Steps 5 and 6 are repeated for all the observed lattice parameters.

By using the transformations above, expressions of the lattice parameter vs $\sin^2\psi$ for the corresponding [001] and [111] fiber axis are

$$a_\psi^{001} = a_0 \left[1 + \left(2s_{12} + \left(s_{11} - s_{12} \right) \sin^2\psi \right) \sigma_{biax} \right]$$

$$a_\psi^{111} = a_0 \left[1 + \left(2s_{12} + \frac{2}{3}J + \frac{s_{44}}{2}\sin^2\psi \right) \sigma_{biax} \right]$$

Where $J = s_{11} - s_{12} - \dfrac{s_{44}}{2}$ is the anisotropy factor of the material. The knowledge of the elastic compliances of the material is required to fit the above equations and determine the value of σ_{biax}. For a sample of mixed texture a combination of the above equations is used with the same stress-free lattice parameter and different stress state for each grain family.

Part III

Single line method for the analysis of X-ray diffraction line broadening

Introduction

This method is based on the article of Th. H. Keijser (J. Appl. Cryst. 15, 308-314, 1982). It is a very useful method to determine the size and microstrain of grain by analyzing a single diffraction peak. This method is ideal for thin films since other methods based on multiple diffraction lines could not be used due to the low diffraction volume and the preferred orientation of the majority of deposited films.

The measures of crystal imperfections by means of diffraction broadening were the full width at half maximum (FWHM, 2*w*) and the integral breadth (*β*). In order to use these quantities for measuring it is need to ascribe an analytical function to describe the line profiles. The best analytical function which applies to diffraction lines is the convolution of Cauchy (lorentzian) and Gaussian functions, namely the Voigt function. The breadths of the Cauchy and Gaussian components can be found from the ratio of the FWHM of the broadened profile to its integral breadth (2*w*/*β*).

The method

The measured line profile *h* is the convolution of the standard profile g with the structurally broadened profile *f*. If *h*, *f* and *g* are voigt functions then:

$$h_c = g_c * f_c \quad \text{and} \quad h_g = g_g * f_g, \tag{1}$$

where the C and G subscripts denote the lorentzian and the Gaussian component of the respected line profiles. From (1) it follows that the integral breadths of f_l and f_g are given by

$$\beta_c^f = \beta_c^h - \beta_c^g \quad \text{and} \quad \left(\beta_G^f\right)^2 = \left(\beta_G^h\right)^2 - \left(\beta_G^g\right)^2. \tag{2}$$

The constituent Cauchy and Gaussian components can be obtained from the ratio 2*w*/*b* for the *h* and *g* profiles using the following empirical formulae:

$$\beta_c / \beta = a_0 + a_1 \varphi + a_2 \varphi^2 \tag{3}$$

and

$$\beta_g / \beta = b_0 + b_1 \left(\varphi - \frac{2}{\pi} \right)^{1/2} + b_1 \varphi + b_2 \varphi^2 \tag{4}$$

where

$\varphi = 2w/\beta$,

$a_0 = 2.0207, \ a_1 = -0.4803, \ a_2 = -1.7756,$
$b_0 = 0.6420, \ b_{12} = 1.4187, \ b_1 = -2.2043,$
$b_2 = 1.8706$

Another issue that has to be mentioned is that since a single voigt function cannot be ascribed to a K_α doublet, either the a_2 component must be removed from the measured profiles.

In order to separate size and strain effects it is necessary to assume that the size and the strain profiles have a particular form. So it is assumed the Cauchy component of the f profile is solely due to the crystallite size and that the Gaussian contribution arises from strain. For a single line analysis the apparent crystallite or domain size D is given by:

$$D = \lambda / \beta_c^f \cos \theta \tag{5}$$

And the strain e by

$$e = \beta_c^f / 4 \tan \theta \tag{6}$$

where β is measured on a 2θ scale and, if K_α radiation is used, λ and θ are the wavelength and angular position of the a_1 component.